Periodic methanol masers and colliding wind binaries

SP van den Heever

13077724

Thesis submitted for the degree *Philosophiae Doctor* in Space Physics at the Potchefstroom Campus of the North-West University

Promoter: Prof DJ van der Walt

October 2017

"If we knew what it was we were doing, it would not be called research, would it?"

Albert Einstein

Acknowledgements

- Firstly, I want to thank my Mom and Dad for their support throughout my journey to this point, where they always encouraged me to keep on going and not to give up on my dreams. I also want to thank them for their support during the difficult times I went through in my personal life during my PhD.

- My friends and family who also encouraged me during this journey. My girlfriend Estie for standing by me and believing in me.

- Prof. Johan van der Walt my supervisor, for his great supervision during this challenging journey called a PhD. When I had difficulty understanding, he was there to help me understand. I want to thank him for his encouragement, long hours of discussions, his understanding, and for all the normal conversations.

- Prof. Melvin Hoare and Dr. Julian Pittard my collaborators from Leeds University in England. Julian Pittard for the provision of the codes which I used to do this project, and both for the invaluable discussions we had during my visits to Leeds, even if it was in a Pub, thank you Melvin. I also want to thank an old student of Julian's, Ross Parkin for the code he provided me. I also want to thank Sharmila Goedhart for valuable discussions, Jabulani Maswanganye for the provision of the data from HartRAO, Esteban Araya for the data from Arecibo, and Marian Szymczak for the data from Torun.

- The Physics department's financial administrator Petro Sieberhagen for all her help for the years.

- Lastly, I want to thank the South African Square Kilometer Array (SKA) project for their financial support during my PhD, and the Physics department at the North West University for their added support the last year.

Abstract

The process by which massive stars form is not yet fully understood. Since massive stars are rare, and generally found at great distances from the Sun, it is difficult to study them and their influence on their environment during the earliest stages of their formation. Although huge strides have been made to better the resolution at which we can observe the environments of these massive stars, it is still very difficult to resolve small scale structures (AU scale) at these large distances where massive stars are located. Since the discovery of *Microwave Amplification by Stimulated Emission of Radiation* (MASERs) we have been provided with a valuable tool by which *High-Mass Star Formation* (HMSF) can be studied. Here we are especially interested in the class II methanol masers at 6.7 GHz, first observed by Menten (1991), and the 12.2 GHz methanol masers (Batrla et al., 1987). In the last few decades it has been firmly established that class II 6.7 GHz and 12.2 GHz methanol masers are exclusively associated with HMSF (Minier et al., 2002, Ellingsen, 2006, Breen et al., 2013). To date $\simeq$ 1000 class II methanol masers have been detected in *High-Mass Star Forming Regions* (HMSFRs) (Caswell et al., 2010, 2011, Green et al., 2010, 2012). A number of these methanol masers have been observed, that show regular/periodic flaring behaviour. Several of these periodic/regular flaring methanol masers, including the first one discovered G9.62+0.20E (Goedhart et al., 2003) show similar light curves. Since the discovery of the periodic/regular flaring several proposals have been made to explain this behaviour. In this work we proposed that the periodicity of the methanol masers are caused by a *Colliding Wind Binary* (CWB) system. The framework is that the methanol masers are projected on the partially ionized gas of the ionization front of the background HII region, i.e. the masers amplify the radio free-free "seed" photons from the background HII region. The UV and X-ray photons produced in the very hot (10^6-10^8 K) shocked gas of the colliding stellar winds are modulated by the stars' orbital motion in an eccentric binary system. This results in a "pulse" of ionizing photons around periastron, which increases the electron density in the partially ionized gas at the ionization front. The increase in electron density causes an increase in the radio free-free emission from that part of the ionization front which the maser amplifies. This was investigated using a hydrodynamical model to simulate the colliding winds, from which SEDs for an entire orbit were calculated using a plasma emission model. The SEDs were used together with the radiation field of a black body (representing the star that maintains the HII

region) to simulate whether the additional ionizing photons will be able to cause an increase in the electron density at the ionization front, i.e. change the position of the ionization front. It is shown that within the framework of the primary star, which maintains the HII region, the additional ionizing photons cause changes in the position of the ionization front. This suggests that the energy generated in the shocked gas is enough to change the position of the ionization front, and can thus change the radio free-free emission from that part in the partially ionized gas of the ionization front. With the proposition that the masers amplify the background radio free-free emission, n_e^2 is solved time-dependently in the approximation that the HII region is optically thin for radio free-free emission from the ionization front towards the maser. The CWB model is compared to the observed maser light-curves, and the CWB model describes the periodic maser flare profiles very well. Thus, it strongly suggests that the observed changes in the maser light curves are most likely due to changes in the free-free emission from the background HII region.

Keywords: High-mass stars – Binary systems: Colliding-Wind-Binaries: UV and X-rays. High-Mass stars – HII regions. radio free-free emission: radio lines – Masers

Opsomming

Die proses waardeur massiewe sterre vorm word tot dusver nog nie heeltemal verstaan nie. Omdat massiewe sterre skaars is, en in die algemeen ver vanaf die Son geleë is, is dit moeilik om hulle self asook hulle invloed op die nabye omgewing gedurende die vroegste fases van vorming te bestudeer. Alhoewel daar enorme vooruitgang gemaak is met die resolusie waarmee die omgewings van hierdie massiewe sterre waargeneem kan word, is dit steeds bykans onmoontlik om op die afstande waar hierdie sterre geleë is klein-skaalse (AU) strukture op te los. Sedert die ontdekking van masers is ons met waardevolle gereedskap verskaf waardeur *Hoë-Massa Ster Vorming* bestudeer kan word. Hier is ons veral geinteresseerd in die klas II metanol masers by 6.7 GHz, vir die eerste keer waargeneem deur Menten (1991), en die 12.2 GHz metanol masers (Batrla et al., 1987). In die laaste aantal dekades is dit stewig vasgestel dat klas II metanol masers by 6.7 en 12.2 GHz uitsluitlik geassosieer word met *Hoë-Massa Ster Vorming* (Caswell et al., 2010, 2011, Green et al., 2010, 2012). Tot dusver is daar $\simeq$ 1000 metanol masers waargeneem in *Hoe-Massa Ster Vorming Gebiede* (Caswell et al., 2010, 2011, Green et al., 2010, 2012). 'n Aantal metanol masers is waargeneem en gevind dat daar gereelde/ periodieke opvlammende gedrag is. Verskeie van hierdie gereelde/periodieke opvlammende bronne, wat die eers ontdekte bron nl. G9.62+0.20E (Goedhart et al., 2003) insluit, wys opvlammende lig-krommes soortgelyk aan G9.62+0.20E. Sedert die ontdekking van die gereelde/periodieke opvlammende gedrag, is verskeie voorstelle gemaak om die gedrag te verduidelik. Hier word dit voorgestel dat die periodisiteit van die metanol masers veroorsaak word deur 'n *Botsende-Wind-Binêre* sisteem. Binne hierdie raamwerk is die metanol masers geprojekteer op die gedeeltelik ge$\ddot{\imath}$oniseerde gas van die ionisasie front van die agtergrond HII gebied, m.a.w. die masers versterk die radio vry-vry fotone vanaf die agtergrond HII gebied. Die UV en X-straal fotone geproduseer in die baie warm (10^6 -10^8 K) geskokte gas van die botsende stellêre winde, word gemoduleer deur die beweging van die sterre in 'n eksentrieke binere sisteem. Die beweging van die sterre in the eksentrieke baan het 'n "puls" van ioniserende fotone rondom periastron tot gevolg, wat die elektron digtheid in die gedeeltelik ge$\ddot{\imath}$oniseerde gas van die ionisasie front laat toeneem. Die toenemende elektron digtheid veroorsaak 'n toename in die radio vry-vry emissie vanaf die ionisasie front wat deur die maser versterk word. Hierdie voorstel is ondersoek deur eerstens 'n hidro-dinamiese model te gebruik om die botsende winde te simuleer, van waar *Spektral Energie Verdelings* (SEDs) vir 'n

hele orbitaal van die binêre sisteem bereken is deur die plasma emissie model te gebruik. Daarna was die SEDs saam met die straling van 'n swart straler (wat die ster se stralingsveld verteenwoordig) gebruik om vastestel of die addisionele ioniserende fotone wel genoegsaam sal wees om 'n toename in die elektron digtheid by die ionisasie front te veroorsaak, m.a.w. 'n verandering in die posisie van die ionisasie front te kan veroorsaak. Dit word gewys dat dit wel die geval is, en dat dit veronderstel dat die energie gegenereer uit die geskokte gas genoegsaam is om 'n verandering in die posisie van die ionisasie front te veroorsaak. Met die stelling dat die masers die agtergrond vry-vry emissie versterk, word n_e^2 tydsafhanklik opgelos vir die benadering dat die HII gebied opties dun is vir radio vry-vry emissie vanaf die ionisasie front na die maser. Die *Botsende-Wind Binêre* model is met die waargeneemde data vergelyk, en die model beskryf die periodieke maser opvlammings profiele baie goed. Dus is daar sterk aanduiding dat die waargeneemde veranderinge in die maser lig-krommes heel moontlik vanweë verandering in die vry-vry emissie vanaf die agtergrond HII gebied is.

Sleutelwoorde: Hoë-massa sterre – Binêre sisteme: Botsende-Wind-Binêres: UV en X-strale, Hoë-Massa sterre – HII gebiede. radio vry-vry emissie: radio lyne – Masers.

Contents

Abbreviations

CD	**C**ontact **D**iscontinuity
MS	**M**ain **S**equence
LoS	**L**ine of **S**ight
PMS	**P**re-**M**ain-**S**equence
CWB	**C**olliding **W**ind **B**inary
YSO	**Y**oung **S**tellar **O**bject
MIR	**M**id **I**nfra**R**ed
GRS	**G**alactic **R**ing **S**urvey
MSX	**M**idcourse **S**pace E**x**periment
MYSO	**M**assive **Y**oung **S**tellar **O**bject
SED	**S**pectral **E**nergy **D**istribution
ISM	**I**nter**S**tellar **M**edium
IMF	**I**nitial **M**ass **F**unction
CMF	**C**ore **M**ass **F**unction
HMSFRs	**H**igh **M**ass **S**tar **F**orming **R**egions
HMSF	**H**igh **M**ass **S**tar **F**orming
IRDCs	**I**nfra**R**ed **D**ark **C**louds
HMCs	**H**ot **M**olecular **C**ores
HMPOs	**H**igh **M**ass **P**rotostellar **O**bjects
HMSCs	**H**igh **M**ass **S**tarless **C**ores
HCHIIs	**H**yper **C**ompact **H**II **R**egions
UCHIIs	**U**ltra **C**ompact **H**II **R**egions
MASERs	**M**icrowave **A**mplification by **S**timulated **E**mission of **R**adiation
GMCs	**G**iant **M**olecular **C**louds
MCs	**M**olecular **C**louds
ZAMS	**Z**ero-**A**ge-**M**ain-**S**equence
UV	**U**ltraviolet
EUV	**E**xtreme **U**ltraviolet
KH	**K**elvin-**H**elmholtz

VLBA	**V**ery **L**ong **B**aseline **A**rray
VLBI	**V**ery **L**ong **B**aseline **I**nterferometry
IR	**I**nfra**r**ed
MIR	**M**id **I**nfra**r**ed
ARWEN	**A**strophysics **R**esearch **W**ith **E**nhanced **N**umerics
CIE	**C**ollisional **I**onization **E**quilibrium

To my family and friends for all their support

Chapter 1

Introduction

1.1 A broader perspective on the study of star formation

Stars are formed from the gas and dust called the *interstellar medium* (ISM), this being described as a cyclic process reshaping the ISM (Kennicutt, 2005). The way in which stars feed energy back into the ISM depends on their mass. For solar type stars the energy is fed back gradually by the loss of their surface layers as they live and die. More massive stars loose a significant fraction of their mass by stellar winds during their lifespan and end their lives in a violent supernova explosion. The supernova explosion replenishes and enriches the ISM, from which a new generation of stars can form (Kennicutt, 2005).

This makes massive stars important objects in the ISM. Stars are defined as massive after reaching a mass of $\simeq 8M_{\odot}$, at which point they have started hydrogen burning and join the *Zero-Age-Main-Sequence* (ZAMS). This means that more massive stars have started burning hydrogen before the end of their accretion stage, which has profound implications for their further formation. It also complicates the study of their formation as it is difficult to distinguish between their luminosity due to accretion and the protostellar luminosity itself (Ward-Thompson & Whitworth, 2011). Except for the violent explosions massive stars end their lives with, during their lives massive stars also dramatically alter their environment by the energetic output of *Extreme Ultraviolet* (EUV) and *Ultraviolet* (UV) photons. These photons heat and ionize the surroundings of the massive star(s), forming HII regions. Massive stars therefore play a key role in the evolution of galaxies and the universe (Zinnecker & Yorke, 2007). Additionally, massive stars also provide heavy elements, which are responsible for the cooling of the ISM, affecting star- and planet formation (see e.g. Zinnecker & Yorke, 2007, and references therein).

The lack in knowledge of *High-Mass Star Formation* (HMSF) is due to the fact that massive stars form deep inside molecular clouds and are therefore heavily obscured by the high degree of visual

extinction. Also, massive stars are rare and are typically found at great distances from the Sun (e.g. Zinnecker & Yorke, 2007, de Wit et al., 2004), making high resolution studies very difficult. The high degree of extinction makes it very difficult to observe them during crucial formation and evolutionary phases because they evolve rapidly. Massive stars are also seldom isolated from other massive stars, which makes their influence on their surrounding environment more complex (e.g. Zinnecker & Yorke, 2007). Their rarity also makes it difficult to construct a clear statistical evolutionary picture from observations (e.g. Shepherd & Churchwell, 1996, Zinnecker & Yorke, 2007). These difficulties hamper progress in the overall theoretical understanding of massive star formation and their evolutionary sequence. The precursor and infancy phases of HMSF can be observed by electromagnetic radiation at Infrared (IR), millimetre/submillimetre, and radio wavelengths. The most renowned signpost during the earliest stages of HMSF is the *Hot Molecular Core* (HMC) stage (see e.g. Beuther et al., 2007, and references therein), prior to the well-known *Ultra Compact* UCHII region stage (Garay & Lizano, 1999, Kurtz et al., 2000). Since massive stars form inside *Molecular Clouds* (MCs), a brief overview of the structures found in the environments of stars/massive stars is given.

1.2 The hierarchy of structures in the ISM

The predominant components of the ISM are gas and dust. Most of the gas in the ISM is hydrogen in different forms: neutral hydrogen (HI), ionized hydrogen (HII) and molecular hydrogen (H_2). MCs are the sites of star formation where the gas is colder and denser than anywhere else in the Universe (Lopez et al., 2010). It is believed that all present day star formation takes place inside MCs (Blitz, 1991). It is also stated by Blitz & Williams (1999) that the association of MCs with star formation is so strong that it can generally be assumed that one will always be able to find molecular gas in the vicinity of young stars. The temperature inside MCs ranges from 10-60 K (e.g. Bontemps et al., 2010, Bergin & Tafalla, 2007), with particle densities higher than 10^3 cm^{-3} (Kurtz et al., 2000). The MCs have a variety of embedded structures, classified as follows:

- **Giant Molecular Clouds (GMCs)**: these clouds are enormous and are composed of dust and gas with a clumpy structure. They have typical temperatures of 15-20 K, average number densities in the order of 10^2 cm^{-3}, and masses of $\sim 10^5 - 10^7$ M$_\odot$; Typically they are $\sim$ 50 pc across (e.g. Carroll & Ostlie, 2007, for a discussion). There are also regions of density significantly greater than the average density within these clouds.

- **Molecular Clouds (MCs)**: they are massive, 10^3-10^4 M$_\odot$, cold (10-50) K H_2 clouds in which the gas is primarily in molecular form. Their densities are of the order 10^2-10^3 cm^{-3}

and sizes in the range of 2-15 pc. They are also generally gravitationally bound (Williams et al., 2000).

- **Clumps**: these structures are smaller, individual parts inside MCs with diameters of a couple of parsecs, average number densities of $\sim 10^3$-10^4 cm^{-3} and masses ranging from $\sim 10 M_\odot$ up to 10^3-10^4 $M_\odot$ (e.g. Kurtz et al., 2000). Their temperatures are in the range of $\sim$ 10-20 K (Bergin & Tafalla, 2007).

- **Dense cores / Cores**: these structures are even smaller, with characteristic diameters of $\leq$ 0.1 pc, and with masses of the order of 0.5 $M_\odot$ up to $\sim 10^2$-10^3 $M_\odot$, have number densities of $\sim 10^4$-10^5 cm^{-3} (Kurtz et al., 2000, Williams et al., 2000), and temperatures of $\simeq$ 20 K (Bontemps et al., 2010).

- **Hot molecular Cores(HMCs)**: these structures are even smaller than dense cores, with sizes ranging from 0.05-0.1 pc, temperatures of 100-300 K and masses that can reach up to 3000 $M_\odot$. They also have very large densities of $\sim 10^6$ - 10^9 cm^{-3} (e.g. Osorio et al., 1999, van der Tak, 2004, Nomura & Millar, 2004).

On the largest scales, molecular gas in the ISM is typically concentrated within galactic spiral arm segments, with sizes up to the kiloparsec scale and masses up to 10^7 $M_\odot$ (e.g. Solomon & Sanders, 1985, Elmegreen, 1985, 1993, Blitz & Williams, 1999). According to Williams et al. (2000) the internal structure of these GMCs is described as follows:

- *Clumps* are coherent regions in longitude-latitude-velocity space that are generally identified from spectral line maps of molecular emission.

- *Star-forming clumps* are the massive clumps from which stellar clusters form.

- *Cores* are the regions from which single stars (or multiple star systems like binaries) are formed.

The internal structure (hierarchy) of the MCs is shown in the schematic representation of Figure 1.1, as taken from Kim & Koo (2001). The *star-forming clumps* are believed to be the birthplace of embedded stellar clusters. These clumps evolve into dense cores due to the supersonic and turbulent velocity fields inside GMCs (Lada & Lada, 2003), which cause collisions that can become gravitationally unstable under the right conditions, and form dense cores and decouple. The largest and most massive of these fragments are potential sites of cluster formation. Most stars predominantly form in star clusters (e.g. Lada & Lada, 2003, de Wit et al., 2004). These dense cores associated with embedded clusters are the most massive (100-1000 $M_\odot$), and have dense ($n(H_2) \sim 10^4 - 10^5$ cm^{-3}) cores within the clumps. Due to the turbulence inside the MCs the various structures that form are filamentary and clumpy (Falgarone et al., 1991).

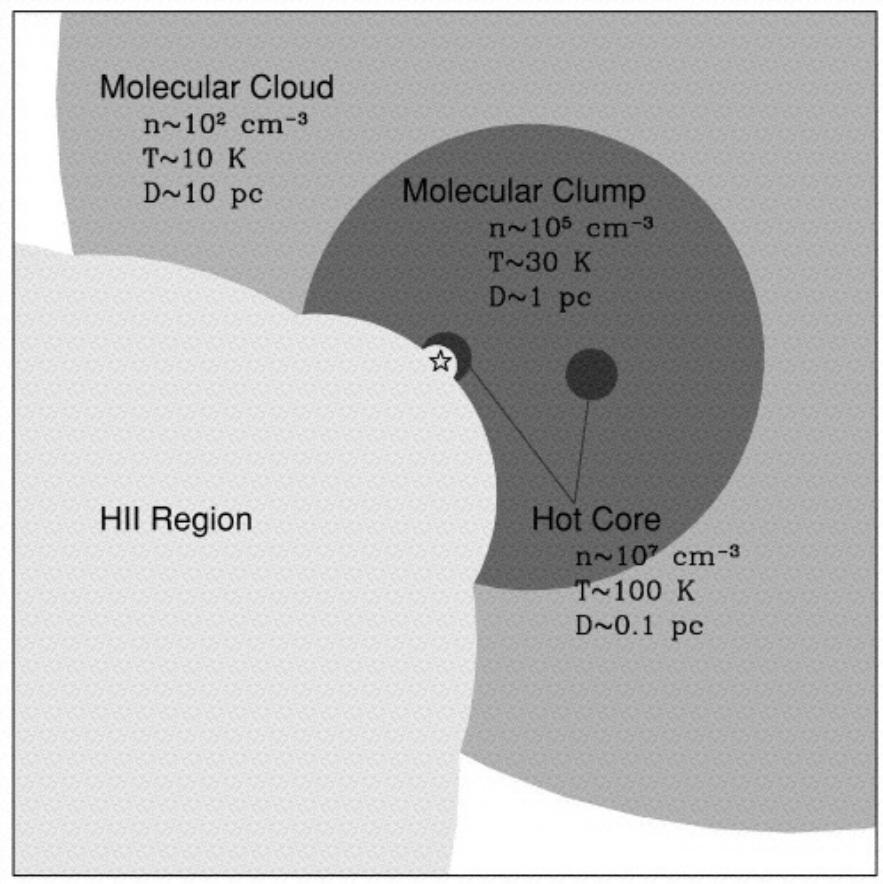

FIGURE 1.1: A schematic representation showing the hierarchy of structures within MCs, taken from Kim & Koo (2001).

star. *Hot molecular cores* (HMCs) inside MCs are believed to be the birthplace of massive single stars, or binary systems (Ho & Haschick, 1981). As mentioned before, these HMCs exhibit extraordinary densities of $n(H_2) \sim 10^6 - 10^9$ cm^{-3} (Osorio et al., 1999, van der Tak, 2004, Nomura & Millar, 2004), and temperatures of up to 300 K (e.g. Cesaroni, 2005). Due to their high densities HMCs obscures the massive star(s) within at near-infrared (near-IR) and optical wavelengths (Hoare et al., 2007).

More recently Beuther et al. (2007) proposed an evolutionary stage for HMSF, where the *cores* and *clumps* are part of the stage called, (1) *High-Mass Starless Cores* (HMSCs) followed by (2) High-Mass Cores harbouring accreting low/intermediate mass protostar(s) to become high-mass star(s), (3) High-Mass Protostellar objects (HMPOs), and (4) Final stars. On a larger scale Beuther et al. (2007) propose Massive Starless Clumps, Protoclusters and Stellar Clusters, where Massive Starless Clumps can only harbour high- and low-mass starless cores. On the other hand, Protoclusters can harbour all kinds of small scale members, low- and intermediate-mass protostars, HMPOs, high-mass cores, HMSCs, and even HCHIIs or UCHIIs (Beuther et al., 2007). How stars form from such structures is the subject of the following sections.

1.3 Star formation fundamentals

As stated earlier, star formation is a fundamental process in the evolution of galaxies and the ISM. Here a brief overview will be presented of the fundamental initial processes involved in star formation. This includes the initial collapse of the MC, and subsequent dynamical time scales involved in the further evolution of the collapsing core.

1.3.1 The Virial Theorem

For star formation to occur from molecular cloud cores, what are the conditions necessary for collapse? The conditions were first investigated by Sir James Jeans, where, under the assumption of hydrostatic equilibrium collapse conditions,

$$2E_{th} + U = 0. \tag{1.1}$$

This is known as the *Virial* theorem, and it states that for a stable gravitationally bound system, the total internal thermal energy (E_{th}) must be twice that of the gravitational potential energy (U). This was estimated by neglecting the effect of rotation, turbulence and large scale magnetic fields (e.g. Carroll & Ostlie, 2007). To calculate the gravitational potential energy U, consider a spherical symmetric cloud with constant density. The gravitational potential energy between two objects with individual masses M and m, a distance r apart, can be written as

$$U = -G\frac{Mm}{r}, \tag{1.2}$$

with G the gravitational constant. Integrating over the entire core from the center to radius R, assuming uniform constant density, the total gravitational potential energy for a prestellar collapsing core (Carroll & Ostlie, 2007) is

$$U \sim -\frac{3}{5}\frac{GM^2}{R}. \tag{1.3}$$

At the stage of collapse, where the internal thermal pressure of the core equals the gravitational potential energy of the cloud (neglecting magnetic fields and an external pressure), the radially dependent pressure can be written as (Tayler, 1994)

$$\frac{dP}{dr} = -\frac{GM_c}{r^2}\rho, \tag{1.4}$$

which is known as the *equation of hydrostatic support*. By the use of

$$-3\int_{V_{center}}^{V_{surf}} PdV = -\int_{M_{center}}^{M_{surf}} \frac{GM_c}{r} dM_c. \tag{1.5}$$

The term on the right hand side is approximately the gravitational potential energy U of a core, where U is the energy required to appropriate the core matter from infinity. Thus, $U = -\int_0^{M_{surf}} \frac{GM_c}{r} dM_c$, and for the left hand side, with $dV = dM/\rho$ and the surface pressure approximated by zero, it follows that (Tayler, 1994)

$$3\int \frac{P_{center}}{\rho} dM + U = 0. \tag{1.6}$$

By using the ideal gas law $P = NkT/V$, where N is the number of particles, P can be rewritten in terms of the mass density, $\rho(N = \rho/\mu m_H)$, for mean molecular weight μ of a particle, and m_H the mass of a hydrogen atom. Expressing the kinetic energy per particle, $(3/2)kT$, as the internal energy per unit mass, $E_m = \frac{3}{2}\frac{kT}{\nu m_H}$, then leads to

$$E_m = \frac{3}{2}\frac{P}{\rho}. \tag{1.7}$$

Substituting this energy into Equation 1.6, and integrating over the entire core, with E the total internal energy of the core, we arrive at the *Virial* theorem

$$\begin{aligned} 2\int_0^M E_m dM + U = 0 \\ \Rightarrow 2E_{th} + U = 0 \end{aligned} \tag{1.8}$$

As mentioned above, this result is obtained by neglecting the influence of rotation, magnetic fields and turbulence in the MC. Assuming that the core consists of a monatomic ideal gas, is a good approximation for cold clouds ($T \simeq 20$K) (Bontemps et al., 2010) of a molecular nature. This is because the energy of the rotational and vibrational degrees of freedom are frozen out for a diatomic ideal gas in equipartition at such low temperatures (Schroeder, 1999), i.e. the kinetic energy of a diatomic gas at a temperature under ~ 100 K is simply $E_{th} = (3/2)kT$.

1.3.2 Collapse criteria

From the *Virial* theorem, the condition necessary for collapse of a molecular core to be initiated is $2E_{th} < |U|$, i.e. when the gravitational potential energy U is larger than twice the internal

thermal energy E_{th} of the core. For a monatomic ideal gas in energy equipartition, $E_{th} = (3/2)kT$, and the number of particles in the core $N = M_c/\mu m_H$, we can rewrite Equation 1.3 and Equation 1.8 for this conditions as

$$\frac{3M_c kT}{\mu m_H} < \frac{3GM_c^2}{5R_c}, \tag{1.9}$$

by substituting the radius R_c. Using the volume of the cloud and the $\rho = M/V$ relation, with constant initial density ρ_o as assumed, we obtain

$$R_c = \left(\frac{3M_c}{4\pi\rho_o}\right)^{1/3}, \tag{1.10}$$

and a minimum mass can be estimated in order for collapse to commence. The condition for the minimum mass necessary is known as the **Jeans criterion**, i.e. $M_c > M_J$, where M_J is the **Jeans mass**, given by

$$M_J \approx \left(\frac{5kT}{G\mu m_H}\right)^{3/2}\left(\frac{3}{4\pi\rho_o}\right)^{1/2}. \tag{1.11}$$

Thus, for a MC with mass $M_c > M_J$, the cloud will commence collapse. Note, however, for the case of a molecular cloud the assumed density stays the same, but the mean molecular weight doubles, so that the *Jeans mass* decrease by a factor of $(1/2)^{3/2}$. However, in the presence of an external pressure the critical mass changes and it is called the *Bonner-Ebert mass* (Carroll & Ostlie, 2007), given by

$$M_{BE} = \frac{c_{BE} v_T^4}{P_0^{1/2} G^{3/2}} \tag{1.12}$$

where $v_T = kT/\mu m_H$ is the isothermal sound speed, and $c_{BE} \simeq 1.18$.

When the MC starts to collapse, it is believed that the collapse takes place isothermally, i.e. the energy released during the collapse is able to escape the cloud without being absorbed elsewhere (optically thin radiative cooling). Inhomogeneities in the cloud will cause the cloud to fragment and form individual condensations within the collapsing cloud, which themselves have to satisfy the *Jeans criterion*. At some point these condensations will become optically thick to the release of energy, at which point the collapse will follow adiabatically. For adiabatic collapse, applying the adiabatic temperature dependence, $T \propto \rho^{\gamma-1}$, and substituting it into Equation 1.11, the *Jeans mass* dependence on density becomes, $M_J \propto \rho^{1/2}$, in which case the *Jeans mass* will increase as the density increases. This description has neglected the influence of magnetic fields on the collapse criteria (see e.g. Williams et al., 2000, Shu & Li, 1997, McKee & Ostriker, 2007,

for reviews). Apart from the collapse criteria for molecular clouds, their evolutionary time scale is also of importance and will be discussed next.

1.3.3 Dynamical time scales

When the mass of a MC is in excess of the *Jeans mass*, the cloud will start its collapse. This process is governed by two time scales during its early evolution (*pre-main sequence*, PMS). The two time scales are the *free-fall* time scale (t_{ff}) and the *Kelvin-Helmholtz* (KH) time scale (t_{KH}).

Under the simplifying assumption that only thermal and gravitational energy play a role in the collapse of a cloud, the *free-fall* time scale is the time it will take a spherically symmetric cloud to collapse to the center where the only force acting is gravity. It is essentially the early evolutionary phase, when the collapsing cloud is still optically thin and all the released gravitational potential energy can be radiated away (e.g. Shu et al., 1987, Carroll & Ostlie, 2007), and the shell of the cloud is seen as simply free-falling. This time is given by

$$t_{ff} = \left(\frac{3\pi}{32}\frac{1}{G\rho_0}\right)^{1/2}. \tag{1.13}$$

This result was obtained by applying the spherical symmetric hydrodynamic equation to the static shell of the cloud prior to collapse, given by

$$\rho\frac{d^2r}{dt^2} = -G\frac{M_r\rho}{r^2}, \tag{1.14}$$

where it is assumed that $||dP/dr|| \ll GM_r\rho/r^2$.

On the other hand, the KH time scale is the time it will take the cloud to radiate all its gravitational energy and convert it to thermal energy. From the *Virial* theorem, the kinetic energy is half the gravitational energy, $E_{th} = -(1/2)U = (3/10)(GM^2/R)$, and the KH time scale is the ratio of the thermal energy to the luminosity of the cloud. Thus, the KH time scale is

$$t_{KH} \simeq \frac{3GM_\star^2}{10R_\star L_\star}, \tag{1.15}$$

where $M_\star$,$R_\star$, and $L_\star$ are the mass, radius and luminosity of the protostar, respectively. Comparing typical values of mass, radius and luminosity of low-mass stars (cf. the Sun, $M_\odot = 1.2 \times 10^{30} kg$, $R_\odot = 7 \times 10^8 m$, and $L_\odot = 3.9 \times 10^{26} Js^{-1}$) with an example high-mass star (O-star, $M_\star = 20M_\odot$, $R_\star = 8.5R_\odot$, and $L_\star \simeq 9 \times 10^4 L_\odot$), Howarth & Smith (2001) show that $t_{KH} = 9.6 \times 10^6$ yr for the Sun, and only $t_{KH} = 4.8 \times 10^3$ yr for the high-mass star. From

equation 1.13, for an assumed molecular density of $n \simeq 10^6$ cm^{-3} (Fontani et al., 2002), this implies that $t_{KH} < t_{ff}$ for massive stars.

This has significant implications for massive protostellar objects, as all the energy will be radiated away by gravitational collapse before the collapse has concluded. This would lead to rapid contraction, and the ignition of hydrogen fusion will commence, producing a significant amount of UV radiation while still accreting material onto the core. The UV radiation field will disrupt the cloud before the protostar is revealed. This is one of the reasons why applying the theory relevant to low-mass stars to high-mass stars is still under debate (e.g. Stahler & Palla, 2005).

1.3.4 The Initial Mass Function (IMF)

A very wide range of stellar masses have been observed, ranging from sub-solar masses to masses in excess of 100 $M_\odot$ (see e.g. Duquennoy & Mayor, 1991, Crowther et al., 2010). The distribution of stellar masses at birth is described by the *Initial Mass Function* (IMF), originally defined by Salpeter (1955), and given by

$$\xi(\log m) = \frac{d(N/V)}{d\log m} = \frac{dn}{d\log m}, \tag{1.16}$$

where $n = N/V$ is the stellar number density in a volume V measured in pc^{-3}. This expression gives the fraction of the stellar population with masses in a logarithmic mass range between m_1 and m_2, i.e. $\int_{\log m_1}^{\log m_2} \xi(\log m)\, d\,(\log m)$. Salpeter (1955) found that the IMF follows a power law distribution described by

$$\xi(\log m) \propto m^{-1.35}, \tag{1.17}$$

which holds for stellar masses in the mass range between 0.4 $M_\odot$ to 10 $M_\odot$. However, outside of this mass range there were substantial uncertainties in the shape of the IMF. Re-analysis of the IMF at the low-mass end (e.g. Scalo, 1986) suggests that there are two local maxima in the IMF, the first (primary) at a few tenths of a solar mass, suggesting that stars form preferentially in this mass regime, and the second maximum ($\sim 1.2 M_\odot$) is believed to be an indicator for bimodal star formation (Shu et al., 1987).

It is found that the IMF is remarkably uniform across different populations, such as field stars and stellar clusters, for both the peak at sub-solar to solar masses and the high-mass power-law tail (e.g. Krumholz, 2011, 2014). The origin of the IMF is still an open question in the context of star formation theory, especially the reason as to why it has these two distinct features at different masses (Krumholz, 2014). One of the more prominent questions as a result of these features is:

is the IMF already determined at the early stages of fragmentation of the molecular cloud, or is it determined by the subsequent accretion processes in cluster environments? The observational study of high-mass star formation may be able to provide answers to these questions. One way in which this was approached was to investigate the mass distribution of the cores in molecular clumps prior to star formation, both for low-mass stars (Motte et al., 1998, André, 2001, André et al., 2001, Andrè & Motte, 2001, Motte & André, 2001) and high-mass stars (Beuther et al., 2004, Williams et al., 2004). These authors found that the mass distribution of the cores or (*Core Mass Function*, CMF) resembles the IMF. There are, however, still uncertainties as to how the CMF maps to the final stellar masses.

1.4 High-Mass Star Formation (HMSF)

To describe the formation of high-mass stars both observationally and theoretically, the formation of low-mass stars is briefly described. Garay & Lizano (1999) summarize the formation of low-mass stars as the quasi-static collapse of the central region of a dense core as a result of ambipolar diffusion. Magnetic support diminishes, and result in the core being supported against gravitation by thermal pressure alone. At this point the stage of free-falling collapse starts, followed by these four evolutionary stages (Shu et al., 1987), known as Class 0-III. The stages are as follows:

- Class 0: the infalling gas and dust is transported onto the central object via an accretion disk, and the angular momentum of the material is dissipated by the disk before it can accrete onto the central protostar (Andre et al., 1993). This is followed by jets and molecular outflows, which are due to the release of the gravitational potential energy of the infalling material, removing the angular momentum from the disk. The protostar is still deeply embedded at this stage, with $M_\star < M_{env}$, where M_{env} is the envelope mass (e.g. Andre et al., 2000, McKee & Ostriker, 2007).
- Class I: in this stage, the protostar still has a surrounding disk, however, the envelope has become diffuse, where $M_\star > M_{env}$ (e.g Andre et al., 2000, McKee & Ostriker, 2007).
- Class II: infall has stopped, and jets and outflows have considerably weakened, exposing the circumstellar disk. At this time these stars are PMS stars. Final contraction kick-starts thermonuclear fusion in the core and these stars join the *main sequence* (MS).
- Class III: at this stage, the circumstellar envelope has been completely removed by the stellar winds and outflows, and the disk has become optically thin (Andre et al., 2000).

Now that the path low-mass stars follow as they are formed has been discussed, what path does high-mass stars follow in their formation process? As stated earlier in this chapter, the study of

high-mass stars is made difficult by the generally large distances at which they are found, their rarity, and the accompanying high visual extinction magnitudes (A_v) (e.g. Lada & Lada, 2003, de Wit et al., 2004, Zinnecker & Yorke, 2007). Due to these factors, our knowledge about their formation is still incomplete. An understanding of the formation of high-mass stars is critical in that it is necessary to be able to describe the formation of stars across the entire IMF, with special attention to the universal slope of the high-mass end.

From Section 1.3.3 for the case of $t_{KH} < t_{ff}$, for massive stars this implies the protostar will have started hydrogen burning before accretion has stopped. Consequently, massive protostars will start to radiate while still accreting material from their surroundings. In theory, the radiation pressure produced should be capable of stopping further accretion as early investigation by Yorke & Kruegel (1977) indicates. This brings us to the crossroad, if the formation of massive stars were to proceed by the standard theory by which low-mass stars form, massive stars should not exist, although they are observed (see e.g. Zinnecker & Yorke, 2007, Beuther et al., 2007, for reviews). On the other hand, numerical simulations including collapse with rotation, resulting in a disk, with the incorporation of radiation pressure, show the star builds up a larger mass ($\simeq 40 M_{\odot}$) before the radiation pressure terminates accretion (see e.g. Wolfire & Cassinelli, 1987, Jijina & Adams, 1996, Yorke & Sonnhalter, 2002). This is still inconsistent with the highest observed stellar masses (e.g. Crowther et al., 2010). Due to this shortcoming, the following competing theories have been proposed:

- a process involving multiple lower mass stars called *coalescence* or merger of low- and intermediate mass stars to produce a massive star in very dense clusters (e.g. Bonnell et al., 1998, Bonnell, 1999, Bally & Zinnecker, 2005).
- a scaled-up version of the *monolithic collapse* picture of low-mass star formation, but in this case via enhanced accretion rates (e.g. McKee & Tan, 2003) so as to be able to overcome radiation pressure, and enhanced disk accretion onto a single massive star (e.g. McKee & Tan, 2003, Jijina & Adams, 1996, Yorke & Sonnhalter, 2002), also known as *direct accretion*.
- a process called *competitive accretion*, which also takes place in a clustered environment. However, here the cluster members compete for material from the same reservoir, with the central members at the bottom of the potential well (e.g. Bonnell et al., 1997, 2001, 2004), followed by individual *monolithic collapse*.

In the *coalescence* scenario, proposed from observational evidence that high-mass stars form at the dense centers of stellar clusters (*mass segregation*) (e.g. Hillenbrand & Hartmann, 1998, Raboud & Mermilliod, 1998), the stellar densities should be high enough ($\sim 10^8$ stars pc^{-3}) so that the cluster members undergo physical collisions and merge, i.e. bypassing the radiation

pressure limitation (e.g. Bonnell et al., 1998). However, the densest clusters observed to date suggests stellar densities of $\sim 10^6$ stars pc^{-3}, which is two orders of magnitude less than the density suggested to make collisions unavoidable, making it an unlikely suspect to produce the highest mass stars observed. This leaves *competative accretion* and *monolithic collapse/direct accretion* as alternatives. These theories both agree on the presence of an accretion disk, and are supported by observational evidence of the presence of jets and bipolar outflows (e.g. Henning et al., 2000, Zhang et al., 2007, Beuther et al., 2005), or circumstellar disks (e.g. Cesaroni et al., 1997, Zapata et al., 2009, Beuther et al., 2012). From these observations, indicating the presence of the same structures found in low-mass stars, various authors (e.g. Wolfire & Cassinelli, 1987, Jijina & Adams, 1996, Yorke & Sonnhalter, 2002, McKee & Tan, 2003, Krumholz et al., 2005, 2007, Zinnecker & Yorke, 2007, Kuiper et al., 2010, 2011) have since devised possible solutions to try and account for the large stellar masses that have been observed. The possible solutions include, (1) enhanced accretion rates of the order of, $\sim 10^{-4} - 10^{-3} M_{\odot} yr^{-1}$, for which the momentum of the infalling material will be high enough to overcome the radiation pressure of the star. (2) reducing the luminosity of the accreting star, by the escape of photons through the bipolar outflows relieving radiation pressure on the disk, the so-called *flashlight* effect. Pudritz et al. (2007) see it as variations in the photospheric temperature from the equatorial to the polar regions, i.e. bolometric luminosity variations. (3) Incorporating the so-called *dust sublimation front* to correctly compute the anisotropy of the re-emitted radiation from the dust grains, a more realistic treatment of the radiation physics omitted by e.g. Yorke & Sonnhalter (2002) and Krumholz et al. (2005, 2007). Kuiper et al. (2010, 2011) showed that including the *dust sublimation front*, preserves the shielding of the accretion disk and the anisotropy of the radiation field, yielding sustained accretion and larger stellar masses ($\simeq 137\ M_{\odot}$).

From the above discussion, and years of observational evidence (the reviews by e.g. Churchwell, 2002, Zinnecker & Yorke, 2007, Beuther et al., 2007) have sketched a crude evolutionary scenario for high-mass star formation, which is similar to that of low-mass stars, with the main differences the influence UV radiation has on the surrounding cloud core, and the much stronger accretion of high-mass star formation. The different stages are given as: (1) **Clumpy molecular clouds**:containing clumps and dense knots of cold molecular material which have already started the star formation process, as they have started to fragment and collapse. (2) **High-Mass Starless Core (HMSC)**: these cores are embedded within *Infrared Dark Clouds* (IRDCs) (Zinnecker & Yorke, 2007). The knots in the MCs have started to collapse into cores, but they do not contain protostars yet (Beuther et al., 2007). (3) **High-Mass Cores harbouring low-intermediate mass accreting protostars**: the embedded stars have masses $< 8\ M_{\odot}$ and have not started hydrogen burning yet, and their luminosity is dominated by accretion (Sridharan et al., 2002). (4) **Hot Molecular Cores (HMC)**: the cold cores are heated by the embedded protostar(s), making them luminous (Churchwell, 2002, Beuther et al., 2007, Zinnecker & Yorke, 2007). Molecular outflows start to develop as a signature of the accretion process (e.g. Garay & Lizano, 1999).

(5) **Hyper Compact HII region (HCHII)**: the accreting protostar has reached a mass of $\sim$ 8 $M_{\odot}$ and has begun hydrogen burning, starting to produce copious amounts of UV radiation which photo-ionizes the accretion disk and thus forms a small ionized region around the protostar (e.g. Churchwell, 2002, Zinnecker & Yorke, 2007). (6) **Ultra Compact HII region (UCHII)**: The star has reached its final position on the main sequence (Final star, Beuther et al., 2007), and the UV radiation results in an evolving ionization front, which starts to be observable at radio frequencies (e.g. Churchwell, 2002, Beuther et al., 2007). (7) **Compact and classical HII regions**: continued expansion of the ionization front of a *Ultra compact* HII region results in the observation of a compact radio source, with further expansion leading to a classical HII region. Consequently, the further evolution will result in dissipation of the parental cloud, exposing the driving source(s).

1.5 On the formation of Binaries

The evolutionary stages of low- and high mass stars have been described, however, only for the formation of a single star at the center of the collapsing cloud core. It has, however, been recognized that the angular momentum in these collapsing cloud cores is several orders of magnitude too large to be contained within a single star (e.g Bodenheimer, 1995), the so-called "angular momentum problem". Several explanations have been proposed, however, for the purpose of this thesis let us assume the explanation that the angular momentum is converted into the orbital motion in a binary system or multiple system. Additionally, at the low-mass end, several observational surveys show that the majority of stars indeed form in binary or multiple systems (e.g Duquennoy & Mayor, 1991, Zinnecker & Mathieu, 2001). This is also the conclusion made from results of further theoretical and numerical work, which handles the formation process as collapse with rotation, and single stars form only in special cases (e.g. Bodenheimer et al., 1993, Bonnell, 1999, Zinnecker & Mathieu, 2001, Bate et al., 2002a,b, 2003). According to e.g. Bodenheimer et al. (1993) and Bodenheimer (1995) the angular momentum of a typical cloud core is comparable to that of a wide binary, and wide binaries at least may directly form from direct fragmentation of the rotating cloud core. However, this cannot explain the observed close binary systems, thus this cannot be the only process playing a role in the formation of these close binary systems. On the other hand, purely dynamical interactions in multiple and binary systems can account for some of the observed binary properties (e.g. Kroupa & Burkert, 2001), but not for close binary systems. The numerical simulations of Bate et al. (2002a,b, 2003) produces many close binary systems. Bate et al. (2002b) attribute this behaviour to three mechanisms, (1) the continued accretion of gas by the forming binary if the accreted gas has a smaller specific angular momentum than the binary, (2) the loss of angular momentum from a forming binary due to tidal interaction with circumbinary gas, (3) dynamical interaction in forming multiple systems

that tend to extract angular momentum from the closer binaries. Bonnell (2001) and Bonnell et al. (2004) also suggest, from their numerical simulations, that the closer the components of the binary system are (i.e. the shorter the orbital period), the mass ratio of the binary systems tends to be close to unity.

For high-mass stars on the other hand, according to a survey by Mason et al. (1998), a fraction as high as ~ 75 % of high-mass stars was found to be part of a binary or higher order systems. This result was obtained by either spectroscopy or confirmed visually. These binary companions also tend to be massive (e.g. Mason et al., 1998, Stahler et al., 2000, García & Mermilliod, 2001), with mass ratios ≥ 0.5. The numerical simulations of Bonnell et al. (1997) and Bate et al. (2003) seem to reproduce the same multiplicity trend for high-mass stars as for low-mass stars, and Larson (2003) states that these simulations seem to produce the stellar IMF. Thus, it is reasonable to assume that a considerable fraction of current HMSFRs are in the process of forming binary or multiple systems. The high binary fraction found from observations and numerical simulations gives strong support to this work.

1.6 Masers as tracers of HMSF

As the title of this thesis suggest, it is necessary to give an overview on masers, as some maser molecules are exclusively associated with HMSF. Here a brief overview of the primary associated maser molecules, namely water (H_2O), methanol (CH_3OH) (e.g. Ellingsen, 2006, Breen et al., 2013), and hydroxyl (OH) (Weaver et al., 1965) will be given.

Since the discovery of strong OH masers by Weaver et al. (1965) in regions of active star formation, various authors have postulated possible underlying mechanisms by which the OH masers are pumped. The first consideration was that these OH masers are located at the surfaces of HII regions. From a theoretical viewpoint, the OH masers are produced in the shocked gas of the expanding shell in front of the ionization front, where the shock has enhanced the density and the OH abundance (Elitzur, 1992). Hydroxyl masers are believed to be radiatively pumped. Observations of 22.2 GHz water masers reveal the association with collimated flows of gas (jets) and molecular outflows (e.g. Torrelles et al., 1996, 1997, 1998b,a, 2003, Moscadelli et al., 2005). This suggests that water masers trace an early phase in the formation of high-mass stars, where collimated outflows and ionized jets are present, indicating that water masers are collisionally pumped.

The other well known maser type, which is of central importance to this thesis is the widespread class II methanol (CH_3OH) masers at 6.7 GHz first observed by Menten (1991), and the 12.2 GHz methanol masers (Batrla et al., 1987). They are *radiatively* pumped by the IR field of the warm dust surrounding the exciting *Young Stellar Object* (YSO). From the models of e.g. Cragg

et al. (2005, and references therein), the conditions necessary to efficiently pump methanol are: (1) dust temperatures of $\simeq$ 100-300 K, (2) methanol relative abundances of ($> 10^{-7}$) or column densities in the range of 10^{15} - 10^{17} cm^{-2}, and by proxy hydrogen densities of $\simeq 10^{6}$-10^{9} cm^{-3} from the high hydrogen column densities found towards HMSFRs (e.g. Beuther et al., 2002a, Anderson et al., 2009, Liu et al., 2011). Hartquist et al. (1995, and references therein) found that purely gas-phase chemical processes can not account for the high methanol abundance, and they proposed methanol to be accounted for by photo-evaporation of methanol from ice mantles of dust grains. Codella et al. (2004) have found water and methanol masers to be associated with an evolutionary stage of HMSF where outflows occur. According to Kurtz et al. (2000) the HMC phase of HMSF has a very brief lifetime of between $\simeq 2 \times 10^3$ and 6×10^4 years. On the other hand, van der Tak et al. (2000) showed that a time of $\approx 10^4$-10^5 yr from the onset of cloud collapse, is necessary to obtain high enough methanol abundances in *Hot molecular cores* (HMCs). Thus, methanol masers tend to appear towards the end of the HMC phase. Additionally, from a statistical consideration van der Walt (2005) suggests that the lifetime of 6.7 GHz methanol masers is brief, lasting $\simeq$ 2.5 - 4.5 $\times$ 10^4 yr, and according to e.g. Codella & Moscadelli (2000) and Codella et al. (2004), the methanol masers disappear as the UCHII region evolves. Observational evidence indicate that these masers are distributed with a variety of structures, circumstellar disks (e.g. Norris et al., 1993, 1998, Phillips et al., 1998, Pestalozzi et al., 2004), outflows (e.g. De Buizer, 2003), also exhibiting ring-like structures (e.g. Bartkiewicz et al., 2009, 2014). Recently, evidence has been presented suggesting that methanol masers are associated with a later stage, where *ultra compact* HII region are present (e.g. Caswell, 2009, Caswell & Breen, 2010, Sanna et al., 2010, Hu et al., 2016, and references therein).

Putting all this together, Breen et al. (2010) proposed a tentative picture of which masers operate during which stage of HMSF. Masers disappear as the UCHII region evolves, before this happens the possibility exists that methanol masers can be projected against the HII region before the evolving HII region destroys the masing column. This is suggested by the association of 6.7 GHz class II methanol masers with HII regions (Caswell, 2009, Caswell & Breen, 2010, Sanna et al., 2010, Hu et al., 2016). In the next section, with this possibility in mind, a model with the HII region as the driving mechanism is proposed to explain the recently discovered periodic methanol masers, which is the subject of this thesis.

1.7 Problem statement and identification

In the last decade it has been firmly established that class II 6.7 and 12.2 GHz methanol masers are exclusively associated with HMSF (Minier et al., 2002, Ellingsen, 2006, Breen et al., 2013). To date $\sim$ 1000 methanol masers have been detected in HMSFRs (Caswell et al., 2010, 2011, Green et al., 2010, 2012). Furthermore, six out of a sample of 54 of these methanol maser sources

examined by Goedhart et al. (2003, 2004) show periodic/regular flaring. The first such source, G9.62 + 0.20E (with a period of $\simeq 243 \pm 2$ days), was very interesting in that the increase in the flux density is very rapid with the onset of a flare, after which it decays. The decay continues to the point it reaches a quiescent intensity, where it remains until the next flare starts (see e.g. Goedhart et al., 2003, 2004, van der Walt et al., 2009, van der Walt, 2011, Goedhart et al., 2014). The questions is, what astrophysical process can be causing this repetitive behaviour in HMSFRs?

From numerical simulations of masers, it is believed that class II methanol masers are radiatively pumped (e.g. Cragg et al., 2005). The possibility also exists that changes in the masing region can influence the maser. However, *Very Long Baseline Array* (VLBA) observations carried out during a flare and during the quiescent state of G9.62+0.20E suggest that there are no changes in the masing region (see e.g. Minier et al., 2002, Goedhart et al., 2005). Therefore, the periodicity of the maser cannot be explained with changes in the masing region. In the case of the masers being radiatively pumped, several emerging hypotheses have been proposed to explain the periodic/regular flaring masers. Araya et al. (2010) proposed that the periodicity arises from periodic accretion onto a circumbinary disk, where the periodic accretion causes an increase in the dust temperature and thus increasing the IR radiation field. Similar to Araya et al. (2010), Parfenov & Sobolev (2014) postulated that the periodicity of the masers originates from rotating spiral shock waves in the gap of a circumbinary disk. On the other hand, Inayoshi et al. (2013) approached the problem from a different perspective, where they attribute the periodicity to stellar pulsations in a PMS stage of stellar evolution. Sanna et al. (2015) also attribute the periodicity to stellar pulsation. Their considerations suggest that the IR radiation field of two objects are super-positioned, where one maintains the maser population inversion and the second results in variability. The second is attributed to a pulsating young star, and the pulsating star is the same as what Inayoshi et al. (2013) modelled. It was argued in van der Walt et al. (2009) that the hypothesis made by Araya et al. (2010) is unlikely, as this would mean that the time-dependent periodic accretion would have to look exactly like the flare profile. This is because the cooling time for dust is very short (as discussed in van der Walt et al. (2009)). Similarly for the other proposals very specific conditions would be necessary to describe the flare profiles as due to variations in the dust temperature (van der Walt et al., 2016).

The mechanism that will be explored in this thesis is that the masers amplify changes in the radio free-free emission from a background HII region. This idea was proposed by van der Walt et al. (2009) and van der Walt (2011) for G9.62+0.20E, motivated by the flaring profiles of the masers, where the decay of the flare resembles that of a partially ionized recombining gas. There is also evidence that the methanol masers are projected against the *ultra compact* HII region associated with this source (see e.g. Garay et al., 1993, Hofner et al., 1996, Sanna et al., 2015). This scenario is shown with the schematic representation in Figure 1.2. The hypothesis is that

the flare profile is caused by a *Colliding Wind Binary* system. In this scenario, the UV and X-ray photons produced in the very hot (10^6-10^8 K) shocked gas of the colliding stellar winds are modulated by the stars' orbital motion in an eccentric system. This results in a short-lived "pulse" of ionizing photons around periastron. The "pulse" of ionizing photons causes additional ionization in the partially ionized gas of the ionization front of the HII region, where we propose the masers are projected. The additional ionization causes an increase in the electron density in the partially ionized gas of the ionization front, and subsequently an increase in the radio free-free emission from the partially ionized gas of the ionization front of the background HII region. The flare is caused by the increase in the electron density at the ionization front, and the subsequent decay of the flare is caused by the decrease in the electron density due to recombination as the "pulse" of ionizing photons diminishes.

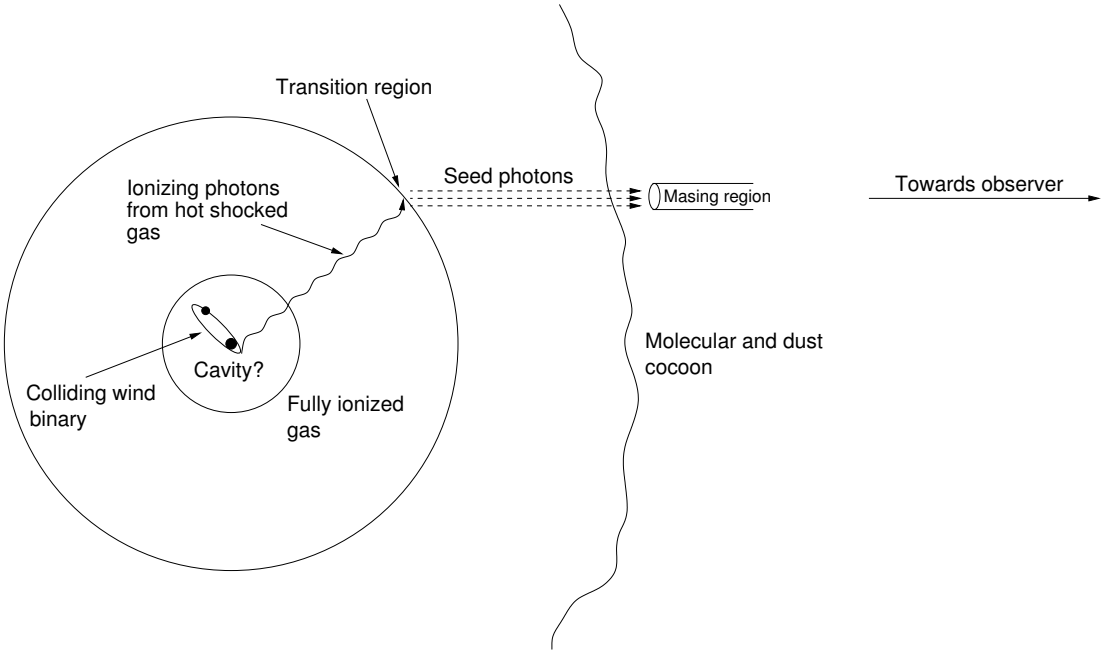

FIGURE 1.2: Schematic representation of the geometry involved in describing the colliding wind binary model for periodic masers, adapted from van der Walt (2011).

Here we compare the methods used in this thesis with the simplifications of the toy model of van der Walt (2011), originally used to fit the periodic masers with the CWB model.

- The simple toy model was applied by van der Walt (2011) to G9.62+0.20E under the assumption that the shocked gas behaves adiabatically (see e.g. Luo et al., 1990, Stevens et al., 1992) for the entire orbit, in which case the luminosity, L_{shock}, generated in the shocked gas changes as the inverse of the stellar separation $L_{shock} \propto D^{-1}$, where D is the stellar separation. It was argued that the same dependence applies for the influence of the additional ionizing photons on the ionization front. In this approach van der Walt (2011) had to assume an eccentricity of $\epsilon = 0.9$ to fit the maser light curve. This high eccentricity

may perhaps be unrealistic. In this work we simulate the shocked gas of the colliding winds hydrodynamically and incorporate the effect of radiative cooling of the shocked gas, i.e. so as to include the possibility that the gas may also cool radiatively during an orbit. If radiative cooling starts to play a role the eccentricity would not need to be as high, as the luminosity for radiative conditions increases considerably faster than the $L_{shock} \propto D^{-1}$ dependence.

- In the toy model, the shocked gas was assumed to be a single temperature gas from which the *Spectral Energy Distribution* (SED) was calculated using *Cloudy* (Ferland et al., 1998). This will be explained in 2. Additionally, van der Walt (2011) used the resulting single temperature SED to show that there can be a significant increase in the electron density at the ionization front for a high enough luminosity. This was, however, a very simplified assumption, because for gas expanding adiabatically the shocked gas constitutes a multi-temperature gas. In this thesis, the shocked gas will be treated as a multi-temperature gas, where the SED will be calculated from the physical properties of the shocked gas. Subsequently, the SEDs with their associated luminosities are used directly to determine whether there is a significant increase in the electron density at the ionization front. This raises the question of whether or not the shocked gas generates enough energy to cause these changes at the ionization front, because $L_{shock} \ll L_{wind} \ll L_{\star}$.

- Lastly, as previously mentioned, van der Walt (2011) only showed that there can be a significant increase in the electron density at the ionization front due to the ionizing photons produced in the shocked gas. Here we will use a maser spot projected onto the ionization front to show that if the position of the ionization front is changed by the additional ionizing photons from the shocked gas, it will increase the electron density the maser "sees" at the ionization front and thus the free-free emission in the optically thin limit ($\tau < 1$), because for optically thin conditions the free-free emission is simply proportional to n_e^2.

The rest of this thesis is set out as follows. In Chapter 2, the background of the different components of the CWB model will be described. Chapter 3 will show the behaviour of the individual components described in Chapter 2. In Chapter 4 the flare profile will firstly be analysed as being due to the recombination of a partially ionized gas, and then the CWB model will be compared to four periodic maser sources (of which G9.62 + 0.20E in one) with the same flare profiles. In Chapter 5, with the assumption of the presence of a CWB, the shocked gas SED will be used to calculate the possible flux of X-rays that may be observed if *Chandra* were to be used to observe some of these star forming regions.

Chapter 2

Theoretical and numerical aspects of the CWB model

2.1 Introduction

The focus here is to give a very brief description of the numerical approach followed for the CWB model in this work, which will be described in much more detail. The layout consists of the theoretical background relevant to each component, followed by a description of the numerical method used to perform the required calculations. Apart from the description of the binary orbit given in the next section, the different components of the CWB model are shown in Figure 2.1. The first component, which is the hydrodynamical code ARWEN (Astrophysical Research With Enhanced Numerics), simulates the shocked gas of the CWB system. ARWEN was developed by Julian Pittard, and the simulations are done in 2D. The shocked gas is simulated for several separation distances between the primary star (hereafter referred to only as the primary) and secondary star (hereafter referred to only as the secondary). This is shown in Figure 2.2, where the separation distances are the lines joining the primary and the secondary. This was done for an entire orbit with stellar separation intervals of 0.1 AU, and repeated for three mass-loss rate combinations of the primary and secondary. Additionally, for each stellar separation several "snapshots" (states) of the shocked gas are generated. For the second component, the Emission code, the output from the hydrodynamic simulations were used to calculate an average SED from the shocked gas for energies 0.01-10 keV. This was done from the "snapshots" for every stellar separation distance, for all three mass-loss rate combinations. The third component, the photo-ionization code *Cloudy* (Ferland et al., 1998), then uses these average SEDs as input to show that the additional ionizing photons influence the position of the ionization front of the HII region. This is done by first simulating the HII region with the star represented as a

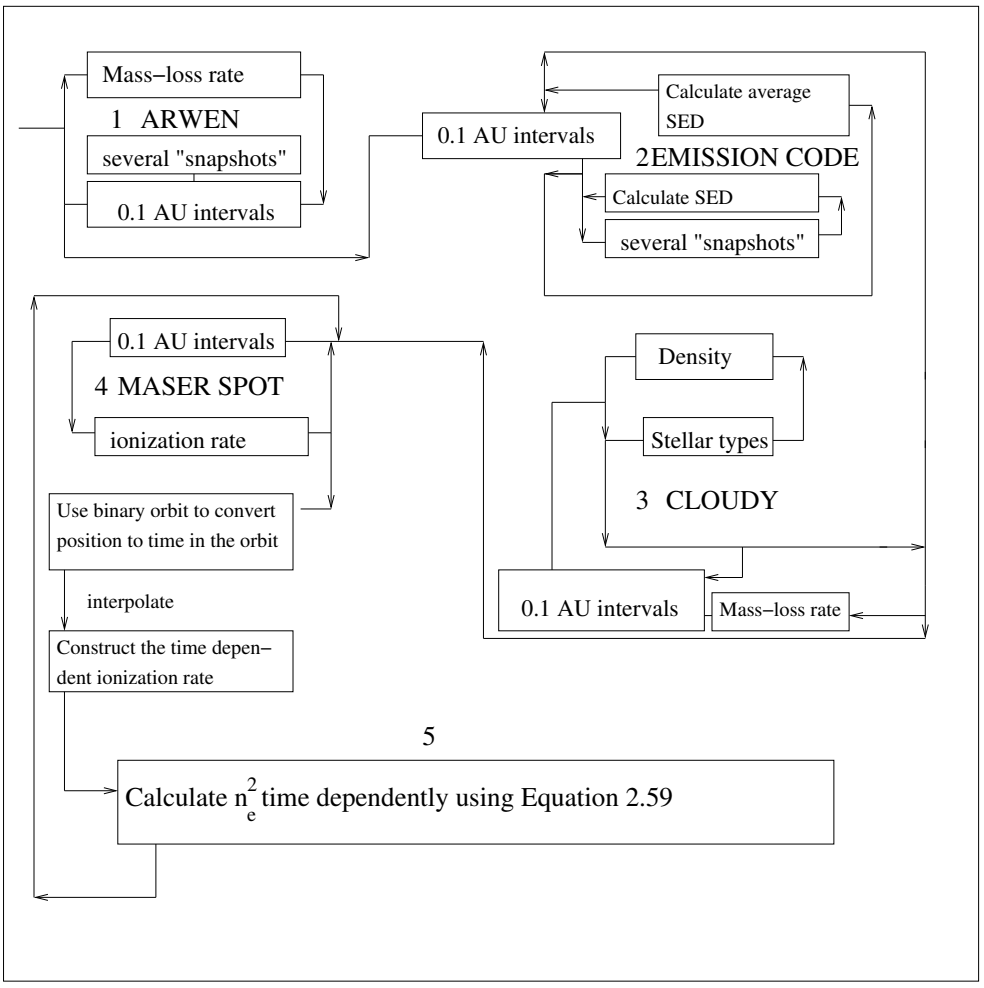

FIGURE 2.1: The diagram shows the path followed to connect the different components of the model to get to the final solution.

black body, then adding the additional ionizing photons. The *Cloudy* calculations were done for several densities, several stellar types, three mass-loss rate combinations, and a complete orbit. These *Cloudy* simulations result in equilibrium states of the position of the ionization front. The fourth component, the Maser spot model, uses the equilibrium states obtained from the *Cloudy* simulations to calculate an ionization rate for every stellar separation distance. This was done for the above mentioned parameter combinations, and additionally for several different positions of the maser spot on the ionization front. All these ionization rates are used to convert them into a quasi-time-dependent ionization rate for each parameter combination. The quasi-time-dependent ionization rates are then interpolated for every single orbit to construct the time-dependent ionization rates for every orbit. The fifth and last component then uses the time-dependent ionization rate for every orbit to solve n_e^2 time-dependently.

2.2 Binary orbit

Here a description of the orbital motion of a binary system is presented. Kepler's three laws of planetary motion are used, as described in Carroll & Ostlie (2007). The first law states that the motion of the secondary around the primary is an ellipse, with the primary situated at one of its foci. Mathematically this is represented by

$$r = \frac{a(1-\epsilon^2)}{1+\epsilon\cos\theta} \tag{2.1}$$

where r is the radial distance between the primary and the secondary (the distance which is going to be referred to throughout the rest of the thesis as the separation distance), θ the angle between the secondary's position and that of closest approach (periastron, i.e., for $\theta = 0$), ϵ the eccentricity of the orbit and a the semi-major axis. The semi-major axis is related to the position of the secondary on the ellipse by

$$r + r' = 2a \tag{2.2}$$

where r is given in the first law, and r' is the radial distance from the other focus point to the secondary, as shown in Figure 2.2.

Kepler's second law states that the line joining the secondary and the primary sweeps out equal areas in equal time intervals. The second law is mathematically expressed as

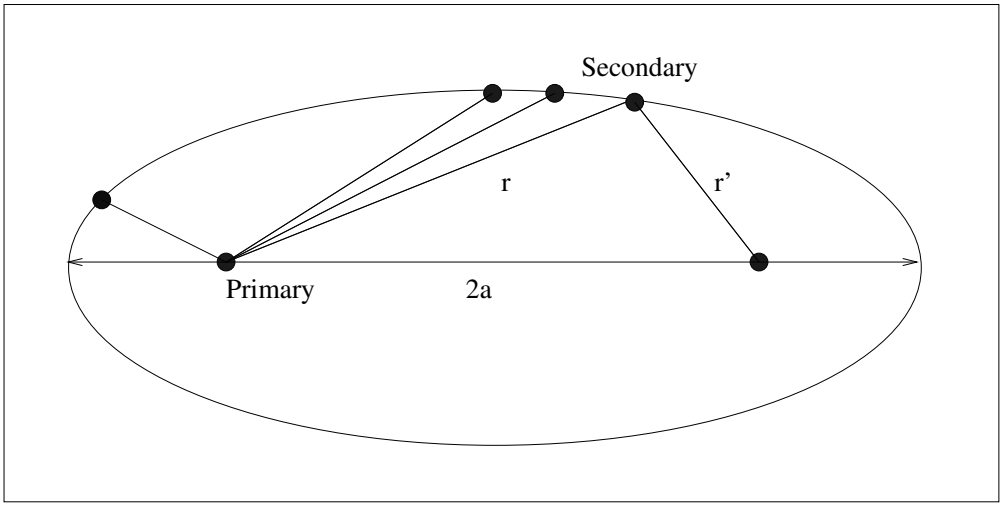

FIGURE 2.2: Schematic representation of the orbit of a binary system in a fixed frame of reference with respect to the primary.

$$r^2 \frac{d\theta}{dt} = \frac{L}{\mu} \tag{2.3}$$

where r is the radial distance given above, $d\theta/dt$ is the angular velocity perpendicular to the radial vector, and μ is the reduced mass of the system, which is given by

$$\mu = \frac{m_1 m_2}{m_1 + m_2}, \tag{2.4}$$

with m_1 and m_2 the masses of the primary and secondary respectively, and the angular momentum L of the system given by

$$L = \mu\sqrt{G(m_1 + m_2)a(1 - \epsilon^2)}. \tag{2.5}$$

From Equation 2.3 it is easy to see that the secondary star's angular velocity will be the smallest near apastron and the largest near periastron in order to sweep out equal areas.

The third law, known as the harmonic law, states that the square of the orbital period is directly proportional to the cube of the semi-major axis a, so that

$$a = \left[\frac{G(m_1 + m_2)P^2}{4\pi^2}\right]^{1/3}. \tag{2.6}$$

Here G is the universal gravitational constant and P the orbital period. The time dependent change of r is calculated using Kepler's second law.

From Equations 2.1 and 2.6 the parameters needed to calculate the orbit are the total mass, period and eccentricity of the system. For an assumed total mass, the period P of the system can be calculated as function of eccentricity. This is done by writing Equation 2.1 in terms of the semi-major axis a for $\theta = 0$, and substituting into Equation 2.6 to obtain

$$\left(\frac{r(1 + \epsilon cos\theta)}{(1 - \epsilon^2)}\right)^3 = \frac{G(m_1 + m_2)P^2}{4\pi^2}. \tag{2.7}$$

Substituting $K = G(m_1 + m_2)$ and expressing the period P in terms of the eccentricity leads to

$$P = \sqrt{\frac{4\pi^2 r_p^3}{K}}(1 - \epsilon)^{-\frac{3}{2}}, \tag{2.8}$$

with r_p the periastron distance. Equation 2.8 is then used in this work to determine: first, the eccentricity for a given periastron distance for a fixed orbital period, and second how the eccentricity will change by changing the total system mass.

2.3 Colliding Wind Binary (CWB)

2.3.1 Basic Structure

In the simplest case, i.e. that of two identical stars in a binary system, the colliding stellar winds will form opposite facing shocks separated by a *Contact Discontinuity* (CD), with the CD being a plane equidistant from either star. This is shown in the schematic representation in Figure 2.3, an example adapted from Stevens et al. (1992). The shock front (stagnation point of the shock) of each wind will form at a distance d from the star. The shock heated gas will flow away perpendicularly from the line of centers (the line which joins the stars) driven both by the thermal pressure gradient and remaining momentum in the shocked gas. The post-shock gas near the line of centers will be subsonic due to the jump conditions behind the shock. Moving away from the line of centers, the stellar winds shock at an oblique angle θ, shown in Figure 2.3, such that the post-shock velocity normal to the shock decreases. The flow velocity of the shocked gas, however, increases with distance further from the line of centers and remains supersonic with velocities close to the stellar wind velocity behind the shock. This is because the velocity component perpendicular to the shock normal increases further from the line of centers. For adiabatically cooling gas this description scales to any separation (neglecting binary rotation), but it breaks down when radiative cooling becomes important.

For high mass stars with surface temperatures of several times 10^4 K and stellar winds that are regulated by their photospheric temperature, the stellar winds can generally be accelerated to velocities of $\approx$ (1-5) $\times$ 10^3 km s^{-1} (Usov, 1992). For such supersonic stellar winds the strong shock conditions are adopted: the post-shock density, velocity, and temperature are respectively taken to be $\rho_s = 4\rho_w$, $v_s = v_w/4$, and $T_s = 3\overline{m}v_w^2 16k$, for an ideal gas. Here $\overline{m} = 10^{-24}$ g is the average mass per particle for solar abundances. From the previous expression for the temperature, it follows that the temperature behind the shocks is $\approx 1 \times 10^7\ v_8^2$ K, where v_8 is the pre-shock velocity in units of 10^8 cm s^{-1}. If, however, we are dealing with a more evolved system such as a Wolf-Rayet (WR)-O star binary, where the WR wind has an enhanced heavy element abundance (thus increasing the average mass per particle), the post-shock gas temperature will be higher (Stevens et al., 1992).

For unequal winds, the position where the CD and the line of centers intersect can be found with a one-dimensional momentum flux balance, $\rho_1 v_1^2 = \rho_2 v_2^2$, given by

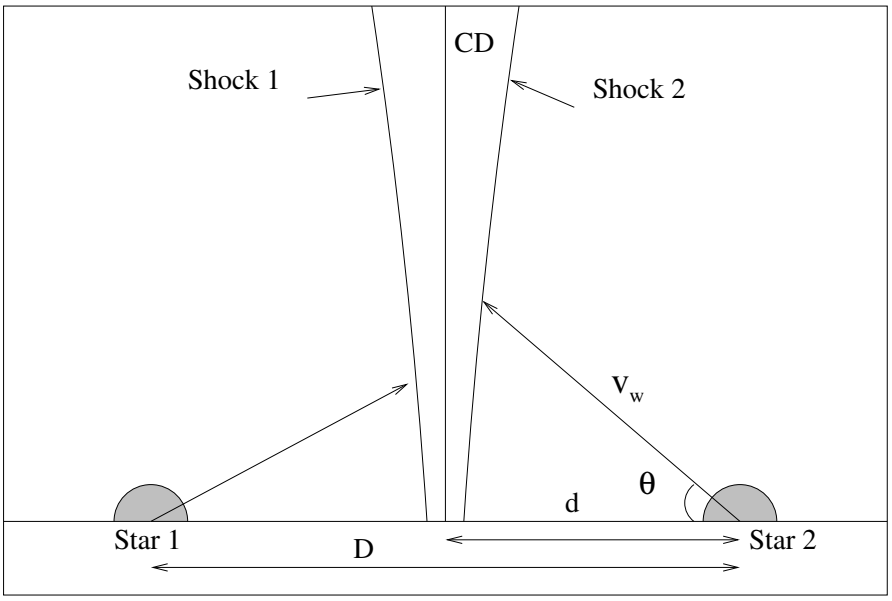

FIGURE 2.3: Schematic representation of the interacting winds of a binary system. The straight line between the oppositely facing shocks is the contact discontinuity, with either star a distance d from the individual shock fronts. The stars are a distance D apart, and the line joining the two stars is called the line of centers. This figure was adapted from Stevens et al. (1992).

$$\eta = (\frac{\dot{M}_1 v_1}{\dot{M}_2 v_2})^{1/2} = \frac{d_1}{d_2}, \tag{2.9}$$

under the assumption that both winds have reached their terminal velocities before being shocked. In Equation 2.9 $\dot{M}_1$ and $\dot{M}_2$ are the respective stellar mass-loss rates, v_1 and v_2 the respective terminal stellar wind velocities, and d_1 and d_2 the respective distances from the center of each star to the stagnation point of the individual wind shocks. For close binaries, the stagnation point of the shock may be within the acceleration zone of one or both of the stellar winds, and a velocity law for the stellar winds is required to solve the momentum balance (see Stevens et al., 1992, for a more complete description) . From Stevens et al. (1992) the stellar winds of binaries with periods of more than a few days will have reached their terminal velocity before being shocked. For winds that have reached terminal velocity and have unequal wind momenta, there are two possibilities for the formation of the shocks: first, the wind momentum of either star (conventionally assumed as the primary) can completely dominate the wind momentum of the other (secondary) and there exists no point of momentum balance, in which case the shocked gas collapses onto the surface of the secondary. Second, for unequal stellar winds which have a stable point of momentum balance, the CD is no longer a plane but a curved surface, with the concave side facing the star with the weaker wind. The surface of momentum balance is now determined by solving the equation of momentum balance in two dimensions. The momentum flux is equated normal to the CD from both winds, using the angles defined and illustrated in

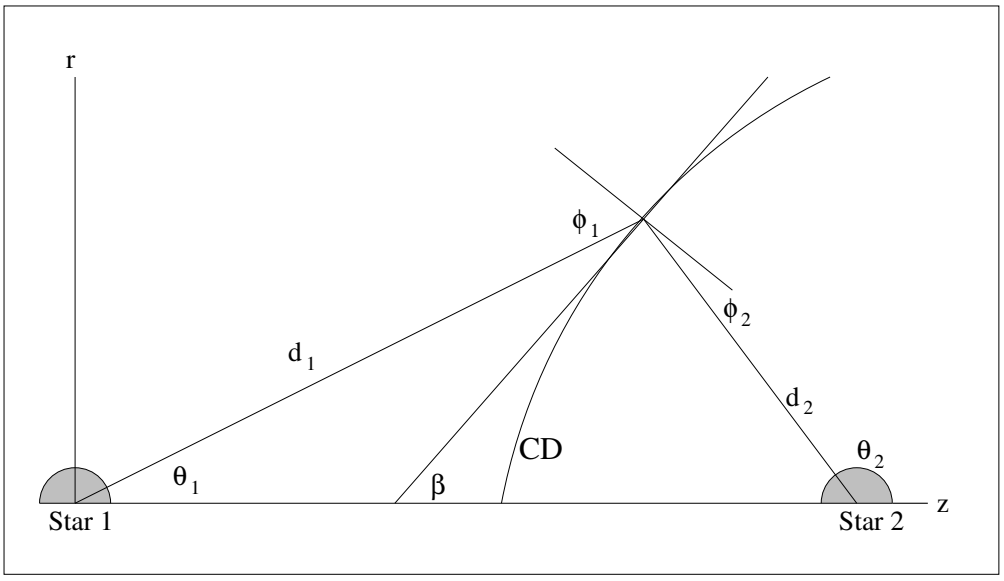

FIGURE 2.4: A schematic representation of the geometry for 2D momentum balance for unequal wind momenta, taken from Stevens et al. (1992). Lengths d_1 and d_2 are the respective distances from the star to the CD. The angles ϕ_1 and ϕ_2 are the angles of momentum balance surface normal to the wind velocity vector as used in equation 2.10, and θ_1 and θ_2 are the angles between the z-axis and the line from each star to the surface of the CD. The quantity β is the angle between the line of centers and the tangent line to the CD surface. This figure was adapted from Stevens et al. (1992).

Figure 2.4 as

$$\frac{\dot{M}_1 v_1}{4\pi d_1^2}\cos^2\phi_1 = \frac{\dot{M}_2 v_2}{4\pi d_2^2}\cos^2\phi_2 \tag{2.10}$$

where ϕ_1 and ϕ_2 are the angles of the momentum balance surface normal to the wind velocity vector, i.e. $v_i \cdot \mathbf{n} = |v|\cos\phi_i$, as discussed by Stevens et al. (1992). From Figure 2.4, the angles θ_1 and θ_2 are the angles between the z-axis and line between the stars and the surface of the CD, and d_1 and d_2 are the distances from the individual stars to the contact surface. The reader is referred to Stevens et al. (1992) for the rest of the derivation.

The geometry considered in Figure 2.4 for unequal wind momenta implies changes to the post shock flow with respect to the case of equal winds. Thus, if the angle of incidence for the primary wind is more oblique than for the equal wind momentum case, the post shock velocity normal to the shock may be significantly lower and the flow velocity higher. In this case the temperature of the shocked gas of the primary will be lower. Thus, although according to the χ value (Section 2.3.2.1) the gas should behave adiabatically, this effect may cause radiative cooling. On the other hand for the secondary, the angle of incidence only becomes oblique with respect to the shock normal much further from the line of centers, thus the post-shock velocity normal to the shock front stays low further out from the line of centers. This also means that the post-shock temperature stays high further from the line of centers. This description gives some insight into

the possibility of the onset of radiative cooling in a seemingly adiabatic-behaving shocked gas. Although this scenario may only happen in the case where the wind momentum of the primary totally dominates that of the secondary, it is also useful to consider for unequal wind momenta with an equilibrium momentum-balance position.

2.3.2 Hydrodynamics

For our purposes, we used the hydrodynamical code ARWEN (Astrophysics Research With Enhanced Numerics) developed by Julian Pittard, based on the VH-1 code (Blondin & Stevens, 1990, and co-workers), to simulate colliding stellar winds. The code is set up to simulate colliding stellar winds as done in the work of Stevens et al. (1992). The simulation is set up on a grid of 500 $\times$ 500 cells with a spatial extent of 10 AU $\times$ 10 AU, using 2D cylindrical symmetry. The stellar winds are set as spherically symmetric, and to emanate from two stationary points a distance D apart and equidistant on either side of the mid-plane of the grid on the symmetry axis. The winds are initiated at the locations of the two stars on either side of the mid-plane of the grid, with their fixed terminal velocities and density mapped onto a few cells around the center of each star before every time step. This is called the remap radius. The mapping of the stellar winds onto the grid results in a minimum separation distance that can be used, because the stagnation point of either of the shocks cannot be within the remap radius. Reflection symmetry is imposed at the symmetry axis, and inflow/outflow conditions at the other three boundaries. The code uses Eulerian hydrodynamics with piecewise linear interpolation of the fluid variables and solves the Riemann problem at each cell boundary to determine time-averaged values at the boundary interfaces, then solving the hydrodynamics equations:

$$\frac{d\rho}{dt} + \nabla \cdot (\rho \vec{u}) = 0 \tag{2.11}$$

$$\frac{\partial \rho \vec{u}}{\partial t} + \nabla \cdot (\rho \vec{u} u + P) = 0 \tag{2.12}$$

$$\frac{\partial \rho \epsilon}{\partial t} + \nabla \cdot [(\rho \epsilon + P)\vec{u}] = -n^2 \Lambda(T). \tag{2.13}$$

where $\epsilon = \frac{\vec{u}^2}{2} + \frac{e}{\rho}$ is the total specific energy, ρ the mass density, e the internal energy density, P the pressure, T the temperature. An ideal gas equation of state $e = \frac{P}{(\gamma-1)}$ is used, with $\gamma = \frac{5}{3}$ as the ratio of specific heats. The quantity $\Lambda(T)$ is the radiative cooling function, shown in Figure 2.5 where it is generated for temperatures in the range $4.0 < \log T < 9.0$ from the Raymond-Smith plasma model (Raymond & Smith, 1977), using the plasma code Mekal of Kaastra & Mewe (2000). The plasma is assumed to be in *Collisional Ionization Equilibrium* (CIE). The radiative cooling is treated self-consistently by using the exact integration method discussed in Townsend (2009).

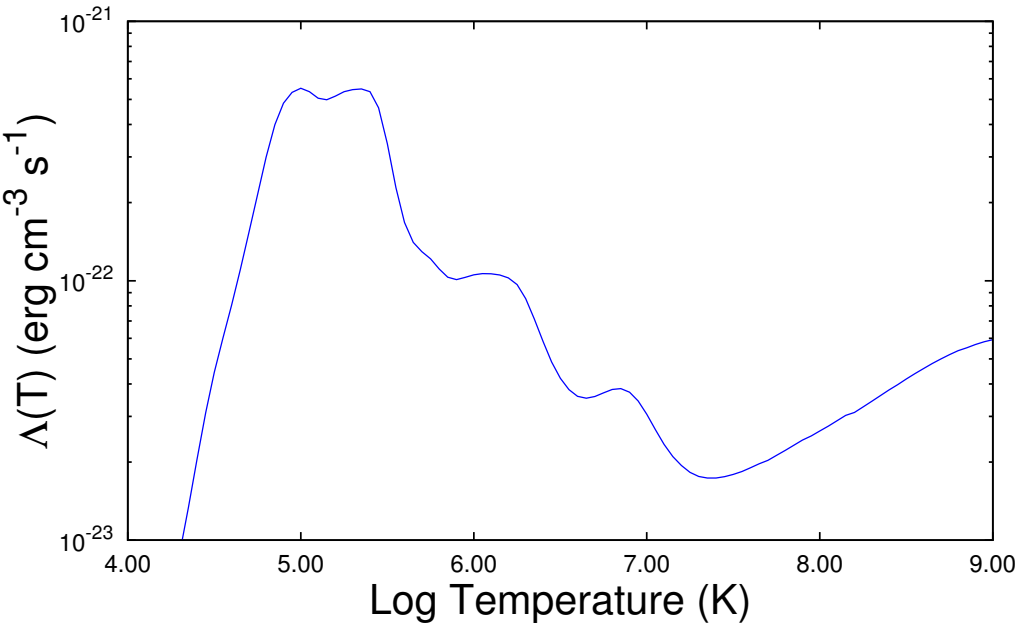

FIGURE 2.5: The temperature dependent total cooling rate for ISM abundances between temperatures of $4 < \log T < 9$.

2.3.2.1 Cooling/Emission

The shocked gas remains adiabatic if no heat is transferred to or from the surroundings and it only does work on the surroundings in order to expand into the unshocked winds. However, gas at the temperatures involved (10^4K - 10^9K) tends to loose energy through radiative cooling. The radiative cooling of the gas is controlled by several processes. The processes that play a significant role in the cooling of the gas are recombination, collisional excitation, collisional ionization and free-free emission (bremsstrahlung). The efficiency of these processes is temperature dependent and will be discussed in Section 2.4.1.

The importance of cooling in the shocked gas is determined by the parameter χ, defined in Stevens et al. (1992) as the ratio between the radiative cooling time and the escape time (dynamical time). A length scale which measures the importance of cooling can be defined by $l_{cool} = t_{cool} v$, where v is the post shock flow velocity away from the line of centers. For a gas cooling with a volumetric emission rate $\Lambda(T)$ (erg cm^{-3} s^{-1}), the cooling time is approximated by (Stevens et al., 1992),

$$t_{cool} = \frac{kT_s}{4n_w \Lambda(T_s)} \tag{2.14}$$

where n_w is the wind number density behind the shock and T_s the temperature of the shock heated wind. Note that the right hand side of Equation 2.14 is of the form $E/(dE/dt)$ where

$E = kT_s$ is the typical energy of a particle in the shocked gas, and $4n_w\Lambda(T_s)$ is equivalent to a energy loss as a result of radiative cooling. On the other hand, the escape time t_{esc} is defined by

$$t_{esc} = \frac{d}{c_s} \tag{2.15}$$

where d is the distance from the star to the CD, which is approximately the radius of curvature, and c_s the sound speed in the shocked gas. The dependence of the cooling parameter on the wind velocity arises from the cooling function's dependence on temperature ($\Lambda \approx T^{-1/2}$). This effectively means that $t_{cool} \propto T^{3/2}$, and with the temperature's dependence on the wind velocity ($T \propto v_w^2$), $t_{cool} \propto v_w^3$ (Dyson & Williams, 1997). Additionally, the sound speed in the shocked gas is close to the velocity of the shocked wind away from the line of centers, i.e., $c_s \approx v_w$. Lastly, from the inverse square law dependence of density on mass-loss rate $n_w \propto \dot{M}/d^2$, the cooling parameter χ is approximated by

$$\chi = \frac{t_{cool}}{t_{esc}} \approx \frac{v_w^4 d_{12}}{\dot{M}_{-7}}, \tag{2.16}$$

where v_w is the wind velocity in units of 10^8 cm s^{-1}, d_{12} is the distance to the CD in units of 10^{12} cm, and $\dot{M}_{-7}$ is the mass-loss rate in units of 10^{-7} $M_\odot$ yr^{-1}.

For $\chi \gg 1$ the shocked gas can be assumed to be adiabatic, while for $\chi \ll 1$ the shocked wind is assumed to be radiative and roughly isothermal. However, χ is only a measure of the importance of radiative cooling, it gives a characteristic value to the bulk of the shocked gas, whereas in reality every single cell in the shocked gas has its own value. It is, however, a useful measure to describe the role of radiative cooling in CWBs.

2.3.2.2 Instabilities

For the situation of CWBs, there are two prominent states in which the shocked gas can be. The gas can either be adiabatic behind the shock or radiative cooling can become important behind the shock. From the adiabatic simulations done by Luo et al. (1990) no instabilities were found, however, these authors point out that the CD should be subject to *Kelvin-Helmholtz* instabilities, provided there exists a velocity shear across the CD. Stevens et al. (1992) found the *Kelvin-Helmholtz* instabilities in their 2D cylindrically symmetric simulations. In the case where the shocked gas is subjected to radiative cooling, the shocked gas will tend to be influenced by local thermal instabilities (Stevens et al., 1992). If $\chi \leq 1$, the shocked gas will cool so as to result in a collapsed, thin shell of cold and dense gas behind the shock. The thin shell is also susceptible to instabilities and is similar to the problem Vishniac (1983) investigated of a thin

shell confined by thermal pressure on one side and ram pressure on the other. All these effects are part of the hydrodynamical solution, so no further detail will be given on instabilities.

2.3.2.3 Luminosity

From the high temperatures produced in the shocked gas behind the shocks, the gas is expected to radiate at X-ray energies. In order to estimate the X-ray luminosity from the shocked gas, some simple qualitative arguments are given to understand how the X-ray luminosity will scale with system parameters. Rough estimates and scaling relations in the adiabatic limit or the complete radiative (isothermal) case are given. In the adiabatic limit, which applies to most systems with periods greater than a few days, the geometry of the colliding winds is scale-free (Stevens et al., 1992), i.e. the volume of the shock-heated gas simply scales as D^3, where D is the binary separation. Furthermore, the total luminosity is given by the emissivity per unit volume ($n^2\Lambda$) times the volume of the shocked heated wind, where the density n is proportional to $\dot{M}/D^2$, resulting in the total luminosity scaling inversely with separation, $L \propto \dot{M}^2/D$. Thus for a highly eccentric orbit the luminosity should exhibit an increase from apastron to periastron as the separation decreases (in the limit that radiative cooling is unimportant). However, the dependence of Λ on the post-shocked temperature (and hence v_w) is more complicated and an equality relation is not possible. If we approximate the temperature as the post shock temperature near the line of centers, and assume a dependence of $\Lambda \propto \mathrm{T}^{-0.5}$, the approximate adiabatic luminosity is given as

$$L \propto \dot{M}^2 v^{-3} D^{-1}(1+\eta)/\eta^4, \tag{2.17}$$

where the approximate effect of unequal winds is included using the wind momentum ratio η (Stevens et al., 1992). In the isothermal limit for binary systems with strong stellar winds and short periods, all the wind kinetic energy normal to the wind shock is radiated away and the total luminosity is some fraction of the wind kinetic luminosity $L \approx f\dot{M}v^2$, where f is the fraction of the wind luminosity lost in the wind shock (Luo et al., 1990, Stevens et al., 1992). Provided that the system remains in the isothermal limit and $v_w(R)$ is constant, the shocked wind luminosity is independent of separation, as established by Stevens et al. (1992) and Pittard & Stevens (2002).

Considering two unequal winds, the luminosity generated from the weaker wind will be greater than the luminosity from the stronger wind, in that more of the weaker wind will be shocked closer to the secondary (Stevens et al., 1992). This is confirmed from the numerical calculations done by Pittard & Stevens (2002). These authors defined the parameter, Ξ, as the fractional wind kinetic power normal to the contact discontinuity i.e., $L = 0.5\Xi\dot{M}v^2$, for the stronger wind. The same can be applied to the secondary to calculate its luminosity contribution.

2.4 Plasma emission

In environments where the formation of a shock (supernova explosion, bipolar outflows, colliding stellar winds, etc.) or the presence of a source of ionizing photons such as an hot star raise the temperature of the gas to and above 10^4 K, the gas reacts so as to return to thermodynamic equilibrium by means of radiative cooling. Depending on the temperature of the gas, there is a number of processes that cause cooling in such plasmas: recombination cooling, free-free continuum emission/cooling (bremsstrahlung), and line emission from collisionally excited or collisionally ionized ions.

2.4.1 Emission processes

- Recombination cooling:

  This is the process of recapture of a free electron by an ion into an excited state, followed by radiative transitions into the ground state with the emission of line photons (Osterbrock, 1989). The energy removed from the thermal electron plasma when electrons recombine with ions depends on the electron's energy. The recombination cross-section depends on the relative velocities of the electrons and protons, so that the recapture of slower electrons is favoured over that of faster electrons (Dyson & Williams, 1997). This has interesting implications for the plasma's temperature: if recombination was the only cooling mechanism available to the gas, the resulting electron temperature T_e would actually be slightly higher than the initial temperature before recombination cooling.

  One of the special cases of recombination cooling is that of two-photon continuum emission. This happens by way of a forbidden transition state where, due to the dipole selection rules, radiative transitions to the ground state cannot occur. However, it can proceed by way of two-photon emission, where the energies of the two photons have to equal the energy difference between the excited state and the ground state (Draine, 2011).

- Collisional cooling:

  Cooling by means of collisions is driven by two processes, i.e. collisional excitation and collisional ionization. These processes become important at high densities where collisions are more frequent.

  - Collisional-excitation: in environments where ionizing photons have caused a substantial amount of ionization, a free electron can collide with an atom/ion and excite it. The ion may undergo another collision with an electron and de-excite the ion before it can emit a photon, in which case there will be no net change in the free electron plasma. However, if the ion can radiatively de-excite before the next collision, it emits

a photon that escapes from the plasma, leading to a net loss of energy from the free electrons (i.e. electron kinetic energy has been converted into photons that escape).

  - Electron-Ion impact excitation of metal ions followed by the radiative emission of line photons is the dominant cooling mechanism in ionized plasmas with metallicities only slightly greater than that of the solar abundance. This cooling mechanism is so efficient that it drives the electron temperature to well below the stellar photosphere temperature (Dyson & Williams, 1997). Collisional excitation energies in the ground state fine structure levels of these ions have typical excitation potentials of a few eV. The thermal energies of the electrons are also of the order a few eV for typical nebular temperatures of 10^4 K. This makes electron-ion impact excitation of the metal ions very efficient.
  - Collisional-ionization: as for photo-ionization, it is assumed that collisional ionization can only occur from the ground-state due to the very fast radiative decay rates (Osterbrock, 1989). The importance of collisional-ionization depends strongly on the free-electron temperature, in order for there to be electrons with high enough kinetic energies to cause ionization out of the ground-state.

- Free-Free emission:

  In an ionized gas, the free electrons "scatter" off the positive ions due to the coulomb force, and cause acceleration of the free electron. The acceleration leads to the emission of a photon, the energy of which is dependent on the energy of the electron before the interaction and the distance between the electron and ion, otherwise known as the impact parameter (Rohlfs & Wilson, 2000). Free-free emission occurs over a wide range of temperatures, and is fairly inefficient when the only sources of cooling are free-free emission and recombination cooling. However, it dominates at high temperatures (10^{7-8} K) where the plasma is fully ionized (Dyson & Williams, 1997).

2.4.2 Emission model

The model that calculates the emission from the shocked gas was developed by Dougherty et al. (2003) and Pittard & Dougherty (2006). It utilizes the cylindrical symmetry of the 2D hydrodynamical grid by rotating the 2D grid through 360° and mapping it onto a 3D cartesian grid. In this way the volume of the individual cells on the 3D grid is calculated by simply obtaining the volume of an annulus around the symmetry axis, given the coordinates and the dimensions of the cell. Thus the emission from a cell is calculated by using emissivity data and the volume of that cell around the symmetry axis. To do this, however, it is necessary to obtain the density and pressure values for the cell from the hydrodynamic simulation to calculate the temperature in each cell. The temperature in each cell is calculated using the ideal gas law:

$$T = \frac{P\mu}{\rho k}, \tag{2.18}$$

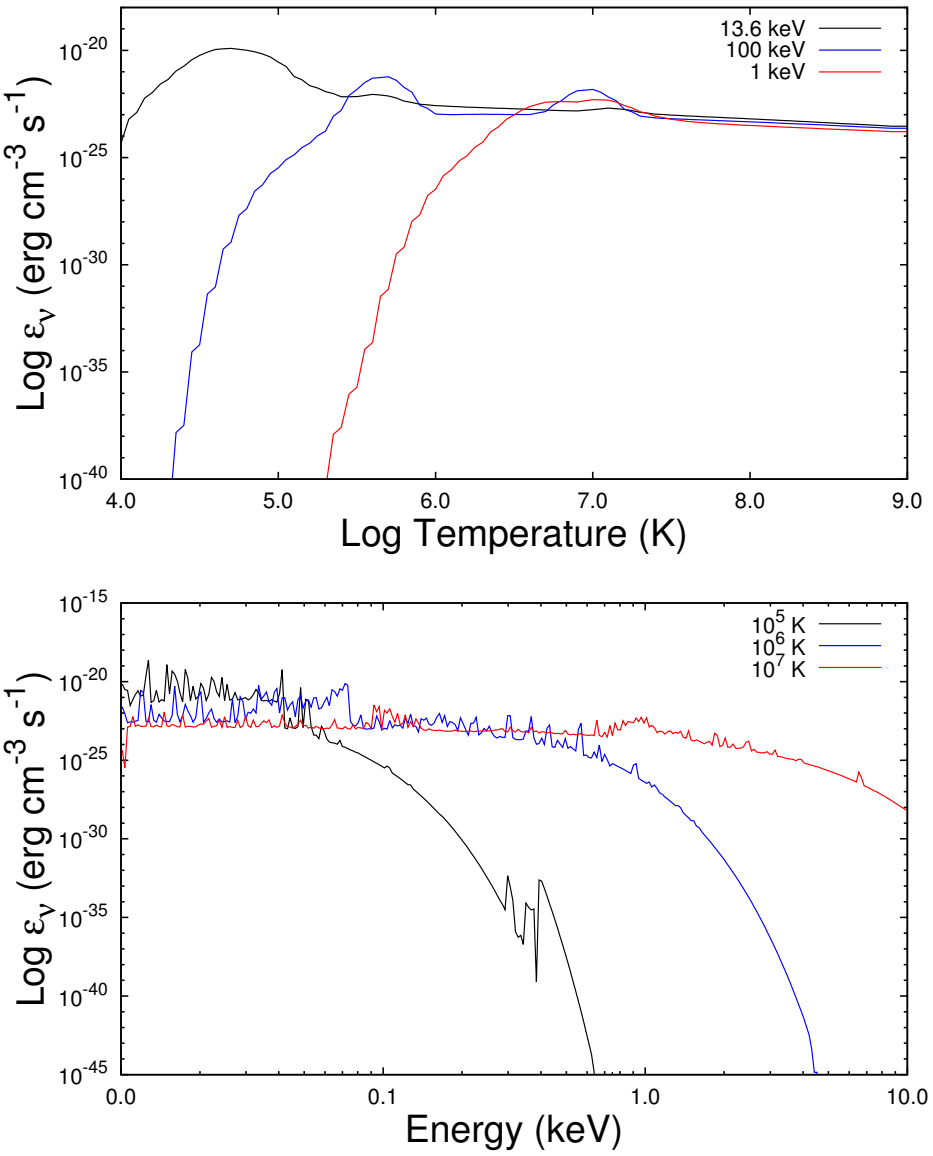

FIGURE 2.6: Top panel: emissivity as function of temperature ($4 < \log T < 9$) for three separate photon energies , 13.6 eV, 100 eV and 1 keV. These temperature-dependent emissivity values are used to interpolate between consecutive temperature values. The bottom panel shows the energy dependent emissivity values at three different temperatures. This shows the energy dependence of the emissivity as function of temperature, i.e. low temperatures will mainly lead to the emission of low energy photons and vice versa for high temperatures.

where μ is the mean molecular weight of the gas, k is Boltzmann's constant, P the pressure and ρ the density. With the temperature known, the volumetric emissivity can be found from a look-up table which is calculated by the *Mekal* plasma code (see e.g. Kaastra & Mewe, 2000, and references therein). The lookup table consists of 300 logarithmically spaced energy bins in the range 0.01-10 keV, and 101 logarithmically spaced temperatures from 10^4-10^9 K. The emissivity

data includes the effects of free-free continuum emission, two-photon and recombination continua, and emission lines of the following elements: H, He, C, N, O, Ne, Mg, Si, S, Ar and Fe.

As the calculated temperature is probably not the same as the temperatures in the lookup table, the emissivity is obtained by interpolating the emissivity as function of temperature for each energy bin. The emission from each cell is then just the emissivity multiplied by the volume. Figure 2.6 illustrates the behaviour of the volumetric emissivity as function of temperature for three photon energies (top panel), and as function of energy for three temperatures (bottom panel). To calculate the total emission, the emissions from all individual cells are simply summed. Although additional information can be obtained from the entire range of temperatures, in this work we only consider emission above the hydrogen ionizing potential (13.6 eV) that is to say temperatures greater than or equal to $\simeq 1.5 \times 10^5$ K. Although lower temperatures can produce hydrogen ionizing photons, Dougherty et al. (2003) and Pittard & Dougherty (2006) found its contribution to the total luminosity to be negligible.

In the case where a HII region is present, we assume that the stellar winds are fully ionized and that the flux of ionizing photons produced in the shocked gas propagate outwards virtually unattenuated. Therefore the absorption of the ionizing photons from the shocked gas is neglected in the stellar winds. The same approach was used by Garcia-Segura & Franco (1996) in their study of the evolution of HII regions and wind-driven bubbles in dense molecular clouds.

2.5 HII regions

As described in Section 1.7, the variability of the masers is proposed to originate in a background HII region, thus the formation and evolution of an HII region is described here in this context. A description of the simulation of an HII region using the photo-ionization code *Cloudy* will also be given.

2.5.1 The case of a pure hydrogen region

Consider the most basic HII region, an ionized region consisting only of pure hydrogen that surrounds a hot star. The hot star is assumed to radiate as a black body, although authors like Puls (2009) investigated the effect electron scattering in stellar atmospheres has on the emergent photon spectrum. Their results suggest that the spectrum of hot stars may not reflect that of a pure black body.

Nevertheless, if for the sake of simplicity we assume that the star radiates as a black body, then the Planck function describes the SED the star produces for a given surface temperature. Wien's law gives the frequency where the maximum flux for a given surface temperature occurs.

If the surface temperature is high enough (for example, greater than 30000 K), the maximum flux lies close to but below the hydrogen ionizing frequency ($\nu_0 \approx 3.29 \times 10^{15}$ Hz). For such high temperatures, a star will produce copious amounts ($\geq 10^{48}$ s^{-1}) of ionizing photons (≥ 13.6 eV), the number of which can be calculated from:

$$S_\star = \int_{\nu_0}^{\infty} \frac{L_\nu}{h\nu} d\nu, \tag{2.19}$$

where L_ν is the spectral luminosity. The number of photo-ionizations per second is then,

$$n_{H^0} \int_{\nu_0}^{\infty} \frac{L_\nu}{h\nu} \sigma(H, \nu) d\nu, \tag{2.20}$$

where n_{H_0} is the neutral hydrogen number density and $\sigma(\nu, H)$ is the photo-ionization cross-section of hydrogen (Osterbrock, 1989). Photons with energies $h\nu \geq 13.6$ eV will be absorbed by the atom and eject an electron from the atom, with the excess energy going into the kinetic energy of the free electron. The kinetic energy distribution of the electrons immediately after the photo-ionization will reflect that of the photon energies. Electron-electron interactions are, however, so efficient that the kinetic energies of the electrons thermalize almost instantaneously. The free electrons are thus assumed to have a Maxwellian velocity distribution, and hence a temperature can be assigned to the gas.

Apart from the process of ionization, the strong Coulomb forces between the electrons and ions tends to lead to the process of recombination. The recombination rate depends on the level of ionization of the gas, so that it is proportional to the product of electron and proton number densities n_e and n_p, which in the case of pure hydrogen is simply n_e^2 ($n_e = n_p$). It also depends on the electron temperature, in that the probability of recombining into a given energy level depends on the electron's energy, and the rate at which protons interact with electrons also depends on the electron's velocity and thus on the electron temperature. Thus, the recombination rate into level n can be written (Dyson & Williams, 1997) as:

$$N_n = n_p n_e \beta_n(T_e) = n_e^2 \beta_n(T_e), \tag{2.21}$$

where $\beta_n(T_e)$ is called the recombination coefficient into level n. In order to balance the ionizations and recombinations, the total recombination rate over all energy levels has to be used. This is done by the summation of Equation 2.21 over all energy levels. Photons produced during recombinations directly into the ground state, are absorbed in the immediate vicinity where they were produced, the so-called "on the spot" approximation. This phenomenon has no net effect on the ionization state of the gas, as one recombination leads to one ionization. Thus the total

recombination coefficient is obtained by summing over recombinations to all levels above the ground state given by:

$$N_r = \sum_{n=2}^{\infty} N_n = n_e^2 \beta_2(T_e) \tag{2.22}$$

from which the equation of ionization balance can be written, by setting Equation 2.20 equal to Equation 2.22, giving:

$$n_{H^0} \int_{\nu_0}^{\infty} \frac{L_\nu}{h\nu} \alpha(H,\nu) d\nu = n_e^2 \beta_2(T_e). \tag{2.23}$$

Now that we have the equation of ionization balance the size of a pure hydrogen HII region can be estimated if the physical properties are known. Consider then a hot molecular cloud core in which a star resides, and assume the gas surrounding the star to be of constant density. Such a star can ionize only a finite amount of the surrounding gas. Thus, there exists a volume at which the total recombination rate just equals the total photo-ionization rate. The size of this region, with radius R_S, can be obtained by the condition of ionization balance using Equations 2.19 and 2.22:

$$S_\star = \frac{4}{3} \pi R_S^3 n^2 \beta_2(T_e). \tag{2.24}$$

where $S_\star$ is the rate at which the star emits ionizing photons, R_S is the so-called initial Strömgren radius (Strömgren, 1939), and n is the neutral density. Rearranging Equation 2.24 we obtain R_S as follows:

$$R_S = \left(\frac{3 S_\star}{4 \pi n^2 \beta_2(T_e)} \right)^{\frac{1}{3}}. \tag{2.25}$$

For representative values for the ionizing flux of massive stars, densities of the environments of such stars, and the recombination coefficient ($\beta_2(T_e) = 2.6 \times 10^{-13}$ cm^3 s^{-1}), one can calculate this radius. The estimate is, however, for a fully ionized region within the radius R_S and for the ionization state of the gas only to change appreciably as one approaches R_S, in other words the transition from fully ionized to neutral, called the ionization front, is small compared to R_S. The linear extent of the ionization front is approximately the mean-free path of an ionizing photon, given by

$$l = \frac{1}{\sigma_\nu n_{H^0}}, \tag{2.26}$$

where σ_ν is the photo-ionization cross-section and n_{H^0} is the neutral hydrogen density. The mean-free path of a 13.6 eV photon in an environment with a density of 10^6 cm^{-3} is $\simeq 1.6 \times 10^{11}$ cm. The ionization front thus provides a well defined region of partially ionized gas where the influence of an additional source of ionizing photons (the "pulse" of ionizing photons from the shocked gas of the colliding winds) can be investigated. It is, however, a bit more complex than that because the assumption of a pure hydrogen nebula is naive. A more realistic approach that includes helium and other heavy elements has to be considered. The next subsection will give a qualitative discussion of the greater complexity that arises if helium and the heavier elements are included.

2.5.2 The influence of including He and heavier elements

Adding helium to the pure hydrogen scenario increases its complexity in that helium has two electrons and three ionic states, although its relative abundance with respect to hydrogen is small with a ratio of ~ 0.1. The two ionization potentials of helium are 24.6 eV and 54.4 eV respectively, both of which are greater than that of hydrogen. From Figure 2.7, the photo-ionization cross-section of neutral helium He^0 is ~ 6 times larger than that of hydrogen at 13.6 eV ($\nu_0 = 3.29 \times 10^{15}$ Hz). This implies that the fraction of photons that will ionize neutral helium with energies $h\nu \geq 24.6$ eV is given as (Osterbrock, 1989, Draine, 2011)

$$y = \frac{n_{He^0}\sigma(He^0,\nu)}{n_{He^0}\sigma(He^0,\nu) + n_{H_0}\sigma(H^0,\nu)}, \tag{2.27}$$

where $\sigma(H^0,\nu)$ and $\sigma(He^0,\nu)$ are the photo-ionization cross-sections of hydrogen and helium respectively, and n_{H^0} and n_{He^0} their densities. For a hydrogen density of 5 $\times 10^6$ cm^{-3}, this fraction is 40% at 24.6 eV. This has significant implications on the ionization equilibrium balance and the structure of the nebula. The ionization of hydrogen will mainly be from photons with energies 13.6 eV $\leq h\nu \leq$ 24.6 eV. On the other hand, a significant fraction (40%) of the photons above 24.6 eV will be absorbed by neutral helium, which results in a central He$^+$ zone surrounded by H$^+$ and He^0 due to the differential absorption of photons with the highest energies closest to the star, a phenomenon called ionization stratification, depicted in Figure 5.3 of Dyson & Williams (1997). Furthermore, the addition of helium will remove most of the excess energy from the free electrons and the temperature of the nebula will decrease.

Heavy elements have much lower relative abundances than helium. Therefore, the absorption of photons by heavy elements does not significantly modify the radiation field of low density nebulae. There are, however, situations where the absorption in specific resonance lines can be important, especially at higher densities, which may be the case for an HII region deeply embedded within a dense molecular cloud, which is important in this thesis. Another effect of heavy elements is

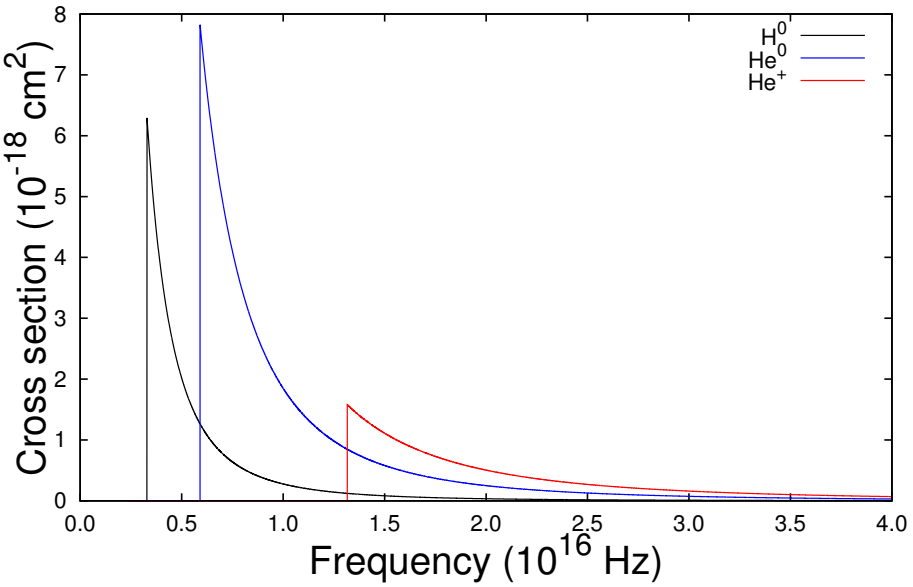

FIGURE 2.7: Frequency dependent photo-ionization cross-sections of: neutral hydrogen (black line), neutral helium (He^0) (blue line) and singly ionized helium (he^+) (red line).

the influence they have on the temperature of the nebula, as heavy elements mostly have high ionizing potentials which will extract energy from the free electrons and significantly cool the nebula (e.g. Osterbrock, 1989, Draine, 2011). However, cooling is mainly due to the escape of photons from the gas when an excited state electron decays to the ground state, as these photons cannot ionize hydrogen.

2.5.3 Evolution of an HII region

The formation of the initial Strömgren sphere was discussed in Section 2.5.1, and the distance at which the ionization equilibrium condition is met was derived. The details of the evolution of the HII region, however, also needs to be addressed. The evolution leading up to ionization equilibrium and subsequent evolution to ultimately reach pressure equilibrium with the surrounding neutral gas is discussed here.

In order to describe the evolution leading up to ionization equilibrium, the quantity of interest is the velocity at which the ionization front propagates into the surrounding neutral gas. The ionization front velocity depends on the flux of photons and the density of the neutral gas, such that the number of photons available for absorption in a time interval dt is equal to the number of neutral atoms ionized by these photons, in the limit where we assume that one photon only ionizes one atom, i.e. $\sigma = 1$. If J (cm^{-2} s^{-1}) is the flux of ionizing photons at a distance R from the star at time t, the total number of ionizations at a time $t + dt$ will be $n_o dR$ at the position $R + dR$, such that for a constant neutral density of n_o,

$$Jdt = n_0 dR. \tag{2.28}$$

Assuming a simple one dimensional slab approach, as shown by the schematic representation in Figure 2.8, the velocity of the ionization front is simply

$$\frac{dR}{dt} = \frac{J}{n_0}. \tag{2.29}$$

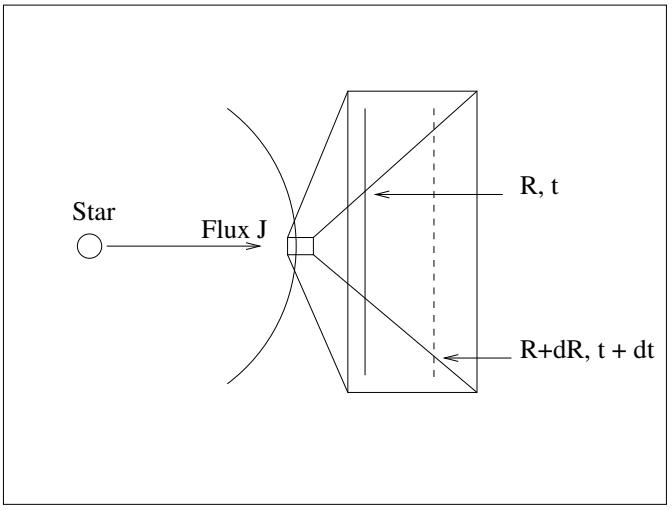

FIGURE 2.8: A schematic diagram of the theoretical considerations for the propagation of the ionization front of the HII region before the initial Strömgren sphere has been set up, as adapted from Dyson & Williams (1997).

In order to solve for the velocity, the flux J is needed. The one-dimensional argument used to obtain Equation 2.29 is, however, insufficient to obtain an analytic expression for the flux J. For the flux J spherical geometry has to be considered. For spherical geometry one has to consider two effects: first, that the ionization front is a sphere with the hot star at its center, and the radiation field is subjected to dilution by the inverse square law; and second, that recombination takes place continuously throughout the ionized region, creating neutral atoms that absorb photons, and causing an additional reduction in the radiation field. The total output of the hot star ($S_\star$) and the flux of the radiation field at the ionization front J are related by

$$S_\star = 4\pi R^2 J + \frac{4}{3}\pi R^3 n_0^2 \beta_2. \tag{2.30}$$

Assuming that ionization balance holds, then the flux J of the radiation field at the ionization front is given by

$$J = \frac{S_\star}{4\pi R^2} - \frac{1}{3} R n_0^2 \beta_2. \tag{2.31}$$

Substituting Equation 2.31 into Equation 2.29 gives the resulting velocity of the ionization front (Dyson & Williams, 1997) as

$$\frac{dR}{dt} = \frac{S_\star}{4\pi R^2 n_0} - \frac{1}{3} R n_0 \beta_2. \tag{2.32}$$

The above expression gives the velocity of the ionization front as function of distance from the star. The velocity of the ionization front will decrease as it moves further away from the star, due to the velocity's R^{-2} dependence on the ionizing flux. The decrease in velocity will continue as the ionization front moves further out. In this expanding phase, the velocity of the ionization front is much higher than the neutral gas can react to, i.e. the expansion velocity is much larger than the sound speed in the neutral gas (Dyson & Williams, 1997), and the neutral gas is thought of as stationary, also called the R-type shock (Shu, 1992). The further the ionization front moves from the star, the slower it will become, and at some point will reach ionization equilibrium. A measure of the time it takes to reach the ionization equilibrium condition, is the characteristic recombination time t_R of the ionized gas, which is given by

$$t_R = (n_0 \beta_2)^{-1}. \tag{2.33}$$

To put this into context for reasonable densities found in high-mass star forming regions, such as 10^4, 10^5 and 10^6 cm^{-3}, the characteristic recombination time for such densities is $t_R \approx 12.2$ yr, 1.22 yr and 0.12 yr, respectively. Substituting Equations 2.33 and 2.25 into Equation 2.32 one obtains

$$\frac{d(R/R_S)}{d(t/t_R)} = \frac{1}{3}\left[\frac{1-(R/R_S)^3}{(R/R_S)^2}\right] \tag{2.34}$$

which has the solution

$$R = R_S \left[1 - \exp^{-t/t_R}\right]^{1/3}. \tag{2.35}$$

From Equation 2.35, at times equal to and greater than t_R the position of the ionization front is very close to R_S and the velocity at which the ionization front progresses slows down considerably and reaches a velocity of $\sim c_s$ (the sound speed in the ionized gas). At this point in the evolution the confined HII region is not in pressure equilibrium with the surrounding cool neutral gas. Subsequently the HII region will start to expand as a result of the pressure imbalance. The velocity c_s at which the ionized gas expands is, however, supersonic with respect to the surrounding neutral gas, and a shock forms which sets the neutral gas into motion. The expansion

will, in principle, stop when pressure equilibrium is reached between the confined hot ionized gas and the surrounding cool neutral gas. The condition for pressure equilibrium is simply

$$2n_f kT_i = n_0 kT_n, \tag{2.36}$$

where the factor 2 is for the increase in density due to photo-ionization of pure hydrogen, n_f is the final ionized gas density and n_0 the neutral gas density. Temperatres T_i and T_n are the respective ionized and neutral gas temperatures. For the ionized and neutral gas we take representative values of $T_i = 10^4$ K and $T_n = 10^2$ K. However, the ionized gas must still absorb all of the ionizing photons. Thus

$$S_\star = \frac{4}{3}\pi R_f^3 n_f^2 \beta_2, \tag{2.37}$$

where R_f is the final radius of the ionized gas. Using Equations 2.24, 2.36 and 2.37, the final ionized gas density is

$$n_f = \left(\frac{T_n}{2T_i}\right) n_0, \tag{2.38}$$

and

$$R_f = \left(\frac{2T_i}{T_n}\right)^{\frac{2}{3}} R_S. \tag{2.39}$$

The ratio between the final ionized gas density and the neutral gas density n_f/n_0 is ≈ 0.005, and the size of the final ionized region R_f relative to the initial strömgren radius R_S, R_f/R_S is ≈ 34. This is, however, the result of the final stage of evolution where the pressure equilibrium condition is met. From the initial strömgren radius the HII region expands with an initial velocity $\sim c_i$ towards pressure equilibrium between the ionized and neutral gas.

A number of assumptions were made in order to describe the evolution. First, that the shocked neutral gas layer is thin because of the compression across the shock, and the shock velocity and ionization front velocity are assumed to be the same. Secondly, we assume that the pressure is uniform in both the shocked neutral gas and the ionized gas (but still time dependent). This is a good approximation if the sound travel times across the neutral shocked gas and the ionized gas is smaller than the time-scale in which considerable change takes place (Dyson & Williams, 1997) in either gas. Thirdly, since the shock is strong (the so-called D-type shock Shu, 1992), it moves supersonically into the neutral gas, thus the strong shock relations as mentioned in Section 2.3.1 are used. Additionally the recombination rate in the ionized gas balances the stellar ionizing

photon output rate, and lastly it was assumed that the neutral gas is at rest, such that the shock velocity relative to the neutral gas says constant.

Putting this into a model (Dyson & Williams, 1997), the pressure P_i in the ionized gas is given by

$$P_i = 2n_i kT_e = n_i m_H c_i^2 \tag{2.40}$$

and by the use of the strong shock relation the pressure P_S behind the shock is related to the shock velocity V_S, and the upstream density, ρ_0, by

$$P_S = \rho_0 V_S^2 \tag{2.41}$$

for an isothermal shock, assuming very effective cooling in the neutral shocked gas. From the assumption that the pressure is uniform behind the shock one gets

$$P_S = P_i = n_0 m_H \dot{R}^2, \tag{2.42}$$

for $\dot{R} = dR/dt = V_S$. Thus, Equations 2.40 and 2.41 give

$$\dot{R}^2 = \left(\frac{n_i}{n_0}\right) c_i^2. \tag{2.43}$$

This result, together with the assumption of ionization balance (Equation 2.37), yields

$$R^{3/2}\dot{R}^2 = \left(\frac{n_i}{n_0}\right)\left(\frac{3S_\star}{4\pi n_i^2 \beta_2}\right)^{1/2} c_i^2 = \left(\frac{3S_\star}{4\pi n_0^2 \beta_2}\right)^{1/2} c_i^2 = c_i^2 R_S^{3/2}. \tag{2.44}$$

From this, using the notation in Equation 2.34, one obtains the differential equation

$$(R/R_S)^{3/4}\, d\,(R/R_S) = \frac{c_i dt}{R_S}. \tag{2.45}$$

Now substitute the dimensionless variables, $\lambda = R/R_S$ and $N = c_i dt/R_S$, and integrate with $\lambda = 1$ for $N = 0$. Note that this is equivalent to assuming that the time it takes to set up the initial strömgren sphere is much shorter then the lifetime of the HII region; This then yields

$$\lambda = (1 + \frac{7}{4}N)^{4/7}, \tag{2.46}$$

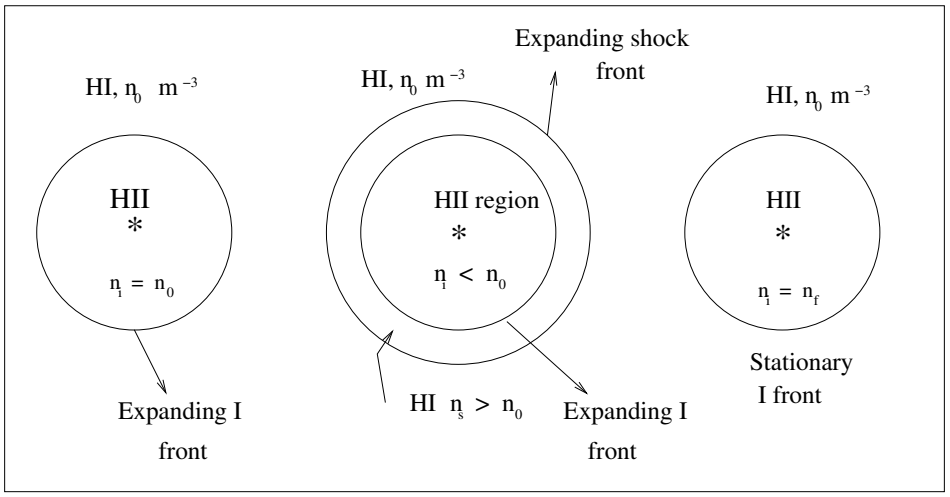

FIGURE 2.9: Schematic representation of the evolutionary sequence of a HII region. The initial phase where the ionization front expands freely up to where the Strömgren sphere is reached (left). In the intermediate evolution phase, where the ionization front expands because of pressure imbalance between the ionized gas and the neutral gas surrounding it, the expansion is supersonic and a shock wave forms (middle panel). Finally the right panel shows the stage where pressure equilibrium with the surroundings is reached. This diagram was adapted from Dyson & Williams (1997).

or

$$\dot{\lambda} = (1 + \frac{7}{4}N)^{-3/7}. \tag{2.47}$$

Yorke (1986) and Franco et al. (1990) amongst others have also derived these results analytically.

From the above result, $\dot{R} = c_s$ initially, and then drops quickly below c_s as the HII region expands. From previous analysis the distance at which pressure equilibrium is reached is ~ 34 R_S, which from Equation (2.46), means a ratio of N ~ 273. Substituting, the time it takes to reach equilibrium is $t_{eq} = 273\ R_S/c_s$, which by making use of the characteristic value of R_S with $S_\star = 10^{48}$ s^{-1}, gives $t_{eq} \simeq 8.41 \times 10^{13}\ n_0^{-2/3}$ yr. Thus, from this result the lifetime of an HII region in gas with a density of 10^2 cm^{-3} is $\sim 3.9 \times 10^8$ yr. This is longer than the lifetime of a massive star, which is a few million years (Tayler, 1994), so the HII region will not reach pressure equilibrium within the stellar lifetime. However, in the local environments of young massive stars, deeply embedded in their natal cloud cores with densities in excess of 10^5 cm^{-3} (Kurtz et al., 1994), the HII region may reach pressure equilibrium with its surroundings before the star reaches the end of its life. In Figure 2.9 the different stages of the evolution of an HII region is shown, as adapted from Dyson & Williams (1997). The left most diagram shows the stage of expansion of the ionization front up to the point of ionization equilibrium, the middle diagram shows the expanding phase from ionization equilibrium to pressure equilibrium and the right-most diagram the pressure equilibrium with the surrounding neutral gas.

2.5.4 Numerical simulation of an HII region

To simulate an HII region such as described earlier, the photo-ionization code *Cloudy* (Ferland et al., 1998) was used. As mentioned in Section 2.5.1, the ionization front provides a well defined region of partially ionized gas (of which the width is $\sim 10^{11}$ cm, for a density of $\sim 5 \times 10^6$ cm^{-3}). The ionization front can thus be used to examine if the additional ionizing radiation from the shocked gas can cause additional ionization, i.e. if the additional flux of ionizing photons can increase the electron density at the ionization front. This is done as follows: (1) an HII region is simulated by specifying only the radiation field of the high mass star; and (2) an HII region is simulated with the addition of the SED from the shocked gas. To this end, the theoretical model of Sternberg et al. (2003) is used to quantify the physical properties of the star.

In *Cloudy* a radiation field is specified by a set of two commands, *shape* and *intensity*. The *shape* of the radiation field of the star is specified as a black body with a given temperature, whereas the *intensity* is specified as the number of photons per second the star produces above the hydrogen ionizing threshold Q(H), given by

$$Q(H) = S_\star = \int_{\nu_0}^{\infty} \frac{L_\nu}{h\nu} d\nu \tag{2.48}$$

where L_ν is the spectral luminosity, ν_0 is the hydrogen ionizing threshold frequency, and the total luminosity of the star is defined by

$$L = 4\pi R_\star^2 \sigma T^4. \tag{2.49}$$

The additional SED produced from the shocked gas of the CWB is included by specifying another command set, i.e. another *shape* and *intensity* command. The *shape* parameter of the shocked gas SED is specified as calculated by the emission model in subsection 2.4.1. The *intensity* parameter of the SED is specified by its luminosity over the energy range, 0.01 - 10 keV used in the emission model.

For the dense gas core the massive star resides in, a constant density is assumed (the final configuration of the gas after star formation). The physical extent is assumed to be large enough to confine the HII region, where the density is specified as the neutral hydrogen density. As mentioned earlier, to exclude interstellar medium (ISM) abundances would not be realistic, as discussed in Section 2.5.2, which gives a qualitative description of the influence on the HII region if ISM abundances were included. The ISM abundance set from *Cloudy*'s database was used. Note that in *Cloudy* the elements are added by specifying each element with an abundance relative to that of hydrogen.

These two simulations were done in order to establish if the additional SED of the shocked gas has enough energy to influence the position of the ionization front of the HII region, i.e. can the SED cause an increase in the electron density at the ionization front. From Section 1.7, we propose that the maser probes this change in the electron density, and thus probes the change of the free-free emission. The next section gives a brief background to radiative transfer and a description of the numerical model along a line of sight passing through the ionization front of an HII region.

2.6 Radiative transfer

This section will serve so as to firstly give a brief background on radiative transfer. It will then endeavour to describe radiative transfer through a specific part of a simulated HII region. described in subsection 2.5.4.

2.6.1 Basic definitions and theory

Consider radiation with specific intensity I_ν propagating in a given direction. The change in intensity through a slab with thickness ds is summarized in the equation of transfer:

$$\frac{dI_\nu}{ds} = -\kappa_\nu I_\nu + \varepsilon_\nu. \tag{2.50}$$

For the optical depth ($d\tau_\nu$) defined as

$$d\tau_\nu = -\kappa_\nu ds, \tag{2.51}$$

the equation of transfer is rewritten as

$$-\frac{1}{\kappa_\nu}\frac{dI_\nu}{ds} = \frac{dI_\nu}{d\tau_\nu} = I_\nu - B_\nu(T), \tag{2.52}$$

where $B_\nu(T) = \frac{\varepsilon_\nu}{\kappa_\nu}$ (*Kirchhoff's law*), and we obtain the solution by multiplying by $e^{-\tau_\nu(s)}$ and integrating by parts(assuming $B_\nu(T)$ is constant throughout the source):

$$I_\nu(s) = I_\nu(0)e^{-\tau_\nu(s)} + B_\nu(T)(1 - e^{-\tau_\nu(s)}). \tag{2.53}$$

2.6.2 Radio free-free emission from a simulated HII region

The previous subsection gave the theoretical description of radiative transfer. The application of radiative transfer to radio free-free emission has been done under the assumption of a constant density and constant temperature nebula consisting of pure hydrogen (e.g. Rohlfs & Wilson, 2000, Kurtz et al., 2000). Franco et al. (2000) amongst others have also done this assuming a power-law density distribution, a radially-dependent electron density with a $n_e(r) \propto r^{-\alpha}$ dependence and a constant electron temperature. Both these approaches calculated the estimated SED from an HII region in the radio frequencies. However, we are interested in calculating the radio free-free emission through a small section of the HII region, as we assume that the maser probes a small volume of the HII region. We assume LTE conditions and therefore that the source function for the ionized gas is simply the Planck function, as given before

$$B_\nu(T) = \frac{\varepsilon_\nu}{\kappa_\nu}, \tag{2.54}$$

where the emission (ε_ν) and absorption (κ_ν) coefficients are given by

$$\varepsilon_\nu = \frac{8}{3}\frac{Z^2 e^6}{c^3}\frac{N_i N_e}{m^2}\sqrt{\frac{2m}{\pi kT}}\ln\frac{p_2}{p_1}, \tag{2.55}$$

$$\kappa_\nu = \frac{4Z^2 e^6}{3c}\frac{N_i N_e}{\nu^2}\frac{1}{\sqrt{2\pi(mkT)^3}}\ln\frac{p_2}{p_1}. \tag{2.56}$$

Where c is the speed of light, e the electron charge, m the electron mass, T the temperature of the ionized gas, and N_i and N_e the ion and electron densities, respectively. The quantities p_2 and p_1 are the impact parameters, ν the frequency in question, Z the atomic charge, and k the Boltzmann constant. From the definition of optical depth (Equation 2.51), and the definition of *Emission Measure* (EM) given by

$$\frac{EM}{pc\,cm^{-6}} = \int_0^{s/pc}\left(\frac{N_e}{cm^{-3}}\right)^2 d\left(\frac{s}{pc}\right), \tag{2.57}$$

the optical depth can be written as

$$\tau_\nu = 3.014\times10^{-2}\left(\frac{T_e}{K}\right)^{-3/2}\left(\frac{\nu}{GHz}\right)^{-2}\left(\frac{EM}{pc\,cm^{-6}}\right) < g_{ff} >, \tag{2.58}$$

where the Gaunt factor (g_{ff}), which gives an approximation for the impact parameters for free-free transitions, is given by

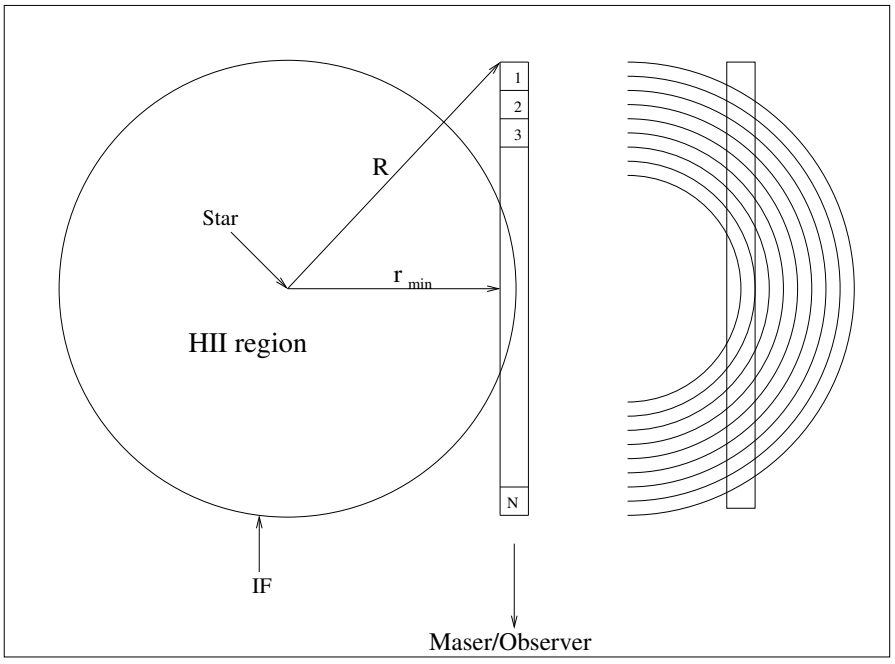

FIGURE 2.10: Schematic representation of the geometry of a spherically symmetric HII region, and the geometry considered to extract the properties along the line of sight through the HII region towards the maser. The left panel shows the HII region and the line of sight of the maser through the ionization front. It also shows the geometry used to extract the density and temperature profiles along the line of sight. The right panel shows the approximate radial intervals of the density and temperature and how the line of sight intersects the profiles.

$$< g_{ff} >= \ln\left[4.955 \times 10^{-2}\left(\frac{\nu}{GHz}\right)^{-1}\right] + 1.5\ln\left(\frac{T_e}{K}\right). \tag{2.59}$$

The geometry we consider for this calculation is shown by the schematic representation of the radially dependent structure of the HII region in Figure 2.10. The rectangle represents the line of sight through the HII region we consider for the calculations. The right panel shows how the line of sight intersects with the radially-dependent structure of the HII region, where the focus of the semi-circles represent the position of the central star, and the smallest semi-circle represents the position of the ionization front. The radio free-free *intensity* at the surface of the HII region is calculated as

$$I(l) = \sum_{j=1}^{N-1} B_{\nu,j}(1 - e^{-\tau_{\nu,j}})e^{-\sum_{i=j+1}^{N}\tau_{\nu,i}} + B_{\nu,N}(1 - e^{-\tau_{\nu,N}}), \tag{2.60}$$

where $B_{\nu,j}$ is the source function from each interval along the line of sight through the HII region (along the rectangle shown in Figure 2.10, where the intervals are numbered 1 to N), in the direction of the maser. If the HII region is optically thin ($\tau_\nu < 1$) for radio free-free emission, the source function, $\tau_\nu B_\nu$, reduces to $\varepsilon_\nu ds$ and we can write

$$I(l) = \sum_{j=1}^{N-1} \varepsilon_{\nu,j} \cdot ds_j e^{-\sum_{i=j+1}^{N} \tau_{\nu,i}} + \varepsilon_{\nu,N} \cdot ds_N. \quad (2.61)$$

In the optically thin limit the radio free-free emission is proportional to n_e^2 at the hydrogen ionization front. For the assumption of optically thin conditions and that the maser simply amplifies the radio free-free emission from the background HII region, the flux density observed from the masers reflects variations in n_e^2. In Chapter 3, it will be shown that the HII region is optically thin ($\tau_\nu < 1$) at the frequencies in question, justifying the use of n_e^2 as a measure of the variability in the free-free emission. From the approach followed with *Cloudy*, the static equilibrium solutions do not reflect the time-dependent changes of the ionization front. Thus, we can not use the static equilibrium solutions to solve n_e^2 time-dependently. The time-dependent solution of n_e^2 will be described in the next section.

2.7 Probing the background HII region with a maser

As discussed in Section 1.7, one of the assumptions of the CWB hypothesis is that the maser spot is projected against a region of partially ionized gas. Within the framework of an ideal spherical HII region, the only such part of the HII region is the ionization front. Given that the ionization front has a relatively sharp transition ($\simeq 10^{11-13}$ cm, for several densities and an photon energy of 13.6 eV), and that it is located far from the ionizing star, the question is whether the ionizing photons from the shocked gas can affect the ionization front sufficiently to produce a significant change in the electron density and thus alter the free-free emission from that part of the HII region.

To examine, as a preliminary test, whether the shocked gas from the colliding stellar winds produces enough energy to cause changes in the electron density at the ionization front, synthetic SEDs were generated by assuming a single temperature gas in collision ionization equilibrium (CIE). This was done using the "coronal equilibrium" command of *Cloudy*, for a temperature of 10^6 K and three different luminosities, namely $\log(L_{cor}/L_\star)$ = -4, -3.5, and -3, respectively. Here L_{cor} is the luminosity of the shocked gas, and a central B0 star with luminosity $L_\star \approx 10^{38.5}$ erg s^{-1} was assumed following Sternberg et al. (2003). The top panel of Figure 2.11 shows the synthetic SED from the CIE calculations, where the flux simply increases with increasing luminosity of the shocked gas. However, it is seen in the bottom panel of Figure 2.11 that the ionization front moves $\simeq$ 0.25 AU in the case where the luminosity of the shocked gas is $\log(L_{cor}/L_\star)$ = -3, i.e. $\simeq 10^{35.5}$ erg s^{-1}. The question now is whether this change in the position of the ionization front will change the radio free-free emission significantly.

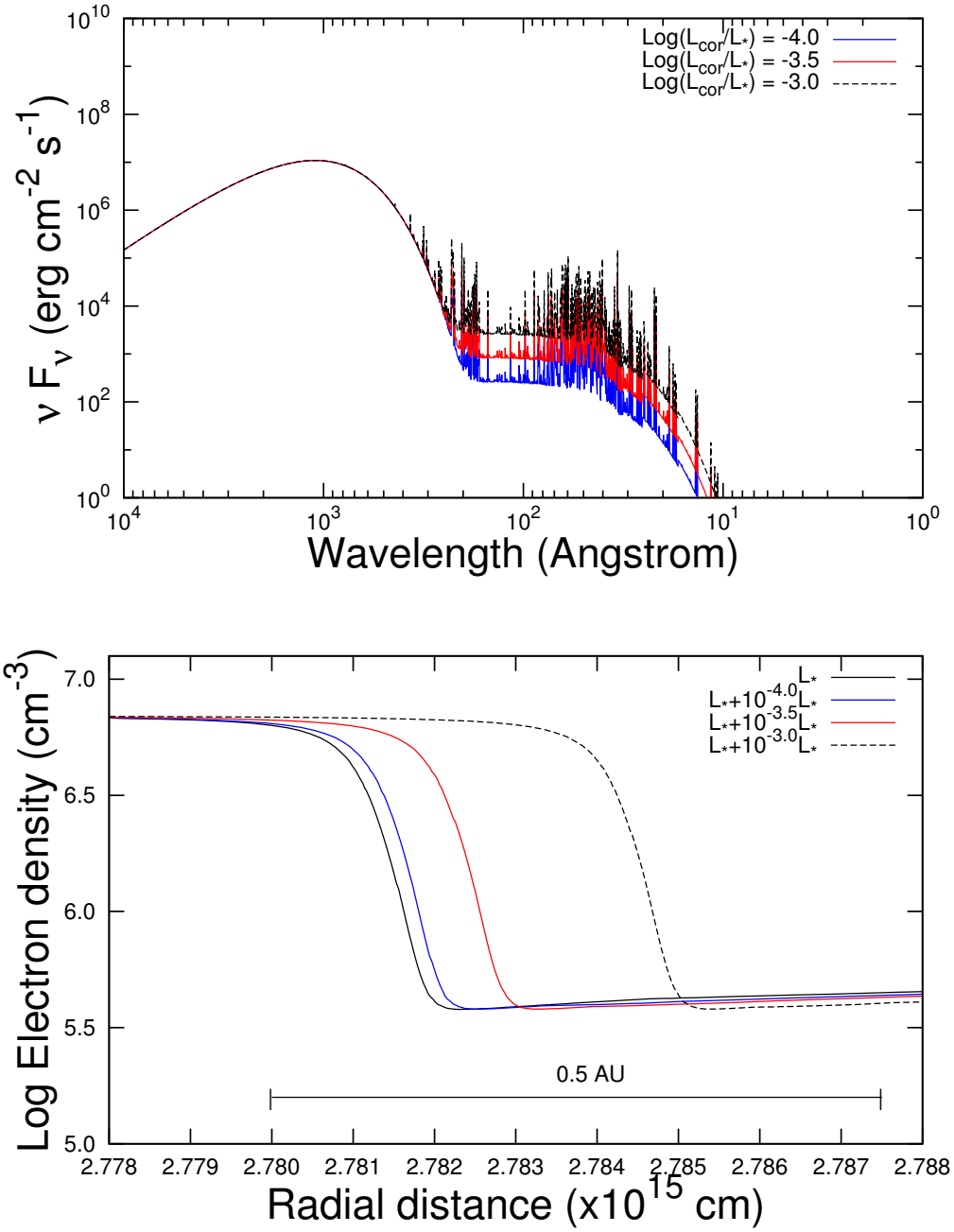

FIGURE 2.11: Top panel: combined black body and single temperature synthetic spectra generated for collisional ionization equilibrium (CIE) conditions. The different colours represent three luminosities of the the shocked gas, the values of which are $\log(L_{cor}/L_\star)$ = -4.0, -3.5, and -3.0. Bottom panel: the respective influence of the synthetic spectra on the ionization front, where the colours match with the spectra in the top panel.

With the assumption that the HII region is optically thin between the ionization front and the maser, n_e^2 can be solved for in a time-dependent way to represent the time-dependent radio free-free emission. The time-dependence of the electron density in the partially ionized gas of the ionization front of the HII region can be solved with

$$\frac{dn_e}{dt} = -\beta_2 n_e^2 + \Gamma_p(t) n_{H^0}, \tag{2.62}$$

from van der Walt et al. (2009) and van der Walt (2011), where the first term on the right-hand side is the decrease in the electron density due to recombinations, and the second the increase in electron density due to ionizations, where n_{H^0} is the neutral hydrogen density. The quantity $\Gamma_p(t)$ is the combined time-dependent ionization rate determined by both the star and the "pulse" of ionizing photons from the shocked gas, where the ionization rate is determined by

$$\Gamma_p(t) = \frac{n_e^2 \beta_2}{n_{H^0}}, \tag{2.63}$$

which is obtained from the equation of ionization balance, given by

$$n_{H^0} \int_{\nu_0}^{\infty} \frac{J_\nu}{h\nu} \sigma(\nu, H) d\nu = n_e^2 \beta_2. \tag{2.64}$$

The observations done by Minier et al. (2002) and Goedhart et al. (2005) of the masers in G9.62+0.20E indicate that the masing regions are of the order of a few AU in extent. From the considerations of Kylafis & Pavlakis (1999), where a masing cloudlet is assumed to be approximately spherical, the maser with the strongest gain will emerge from the longest path through the centre of the masing cloudlet and the path through the center is approximated by a cylinder. Thus it is reasonable to assume, to zeroth order, that the maser probes a small circular volume at the ionization front of the HII region, where the average electron density is determined by the geometric considerations in the bottom panel of Figure 2.12 as

$$\overline{n_e} = \sum_{i=1}^{n} \frac{n_{e,i} d\sigma_i}{\sum_{i=1}^{n} d\sigma_i}, \tag{2.65}$$

where $n_{e,i}$ is the radially dependent electron density, $d\sigma_i / \sum_{i=1}^{n} d\sigma_i$ the corresponding area-weighted contribution to the average from each interval, and $\sum_{i=1}^{n} d\sigma_i$ the total area of the maser spot. The top panel of Figure 2.12 shows how we project the maser onto the ionization front of the HII region, and the bottom panel shows the schematic representation of the maser spot and the radially-dependent electron density the maser spot probes at the ionization front (the vertical lines).

To determine the time-dependent ionization rate, the maser is projected against the ionization front of the HII region. For the radially-dependent electron density obtained from the simulation, where only the stellar SED was used, the minimum value for $\Gamma_p(t)$ is determined using Equation

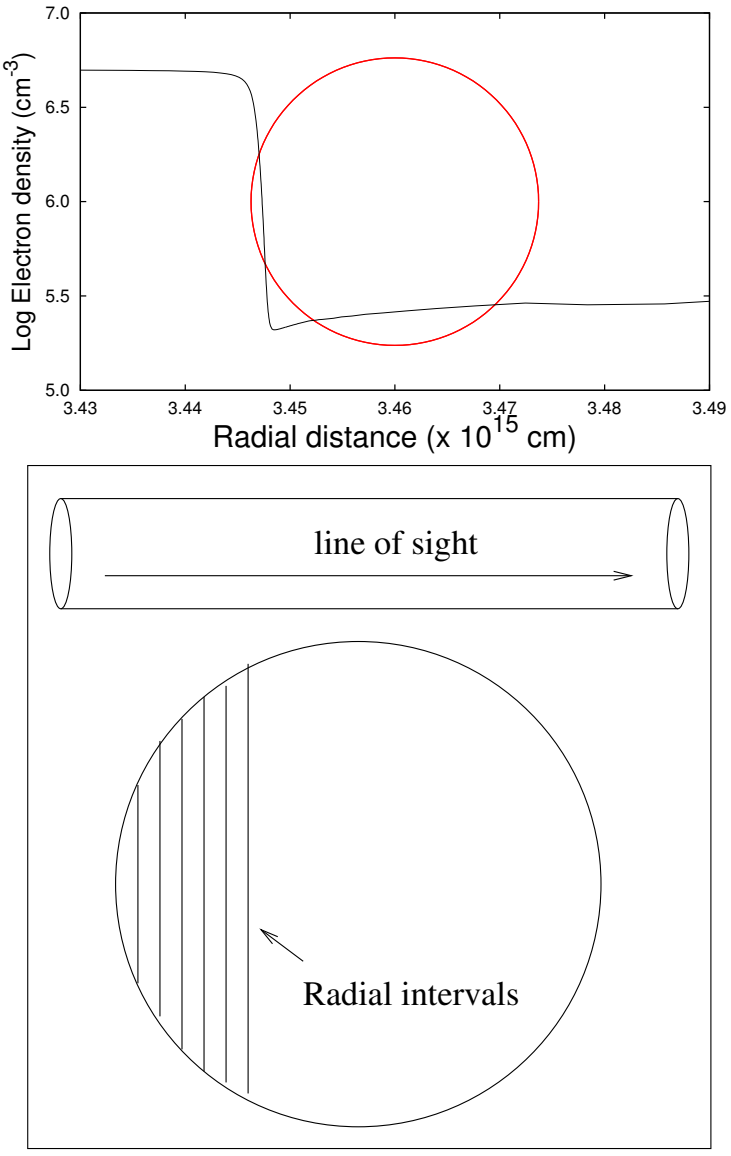

FIGURE 2.12: Top panel: the maser projected at the ionization front (red circle). Bottom panel: schematic representation of the projection, where the vertical lines represent the different lines of sight, and the radial electron density intervals.

2.63, as the star still sustains the position of the ionization front, with or without additional ionizing photons from the shocked gas. When the additional SED of the emission from the shocked gas is added to the SED of the star, and the extra ionizing photons tend to cause more ionization at the ionization front (examples of which are shown in the bottom panel of Figure 2.11), the ionization rate will increase above that of the star alone for the same maser spot projection. Thus, from the effect the SEDs from individual stellar separations have at the ionization front, we can construct a quasi-time-dependent ionization rate, as each SED represents a certain time in the orbit of the binary system. From the quasi-time-dependent static equilibrium solutions from *Cloudy*, the time-dependent ionization rate is obtained using a cubic interpolation scheme. This, however, results in a symmetric time-dependent ionization

rate, as the static equilibrium solutions leads to identical results for stellar separations on either side of periastron. As HII regions are dynamical structures, something to take note of is that cooling processes in the ionized gas can result in variations in the position of the ionization front. Such variations were investigated by García et al. (2013) for a density of 10^4 cm^{-3} assuming a pure hydrogen nebula. They found that such variations do occur. However, for the densities we use in this work these variations should be minimal due to the increased external pressure. Thus, to first order we take the position of the ionization front for only the star as the background state.

Now that the time-dependent ionization rate has been obtained, the time-dependent electron density can be solved for, using Equation 2.62. With a symmetric ionization rate around periastron, the electron density will increase towards periastron. For $n_e^2\beta_2 < \Gamma_p(t)n_{H^0}$, the electron density will keep on increasing, that is to say while ionization dominates recombination. When the point is reached where $n_e^2\beta_2 \simeq \Gamma_p(t)n_{H^0}$, the recombination rate becomes larger than the ionization rate and recombination starts to dominate. From where recombination dominates, the time-dependent electron density is governed by (van der Walt et al., 2009)

$$n_e^2(t) = n_{e,b}^2 \left(\frac{u_0 + \tanh(\alpha n_{e,b} t)}{1 + u_0 \tanh(\alpha n_{e,b} t)} \right)^2 , \tag{2.66}$$

where $n_{e,b}$ is the background to which the electron density returns, $u_0 = n_{e,0}/n_{e,b} > 1$ the ratio between $n_{e,b}$ and $n_{e,0}$, and $n_{e,0}$ the maximum electron density from where recombination commences. This process describes the decay of the maser flare. In Chapter 3, Equation 2.66 will be used to illustrate the general behaviour of recombination using different $n_{e,b}$ and $n_{e,0}$ values.

Chapter 3

General model behaviour

3.1 Introduction

In Chapter 2 the theoretical background and numerical methods used were discussed. This chapter is dedicated to showing how the different components of the numerical model behave. First, the behaviour of the binary orbit for several periastron distances, and several system masses is shown. Second, it is shown how the shocked gas behaves for adiabatic cooling and radiative cooling. Third, from how the shocked gas behaves in the adiabatic cooling and radiative cooling regimes, it is shown how the SED behaves. Fourth, from the SEDs it is shown how the influence on the ionization front changes for SEDs produced from adiabatic cooling and radiative cooling gas. Furthermore, from the *Cloudy* simulations it is shown that the HII region is optically thin for radio free-free emission, for the frequencies in question. Lastly, from this result n_e^2 can be used to simulate the time-dependent change in the radio free-free emission, as our hypothesis assumes its the change in the radio free-free emission from the background HII region that causes the periodicity in periodic masers.

3.2 Binary orbit

From Kepler's three laws three parameters are needed to describe the orbit of the secondary star on its elliptic orbit around the primary star in the binary system. The three parameters are, (i) the orbital period of the system (P), (ii) the eccentricity of the system (ϵ) and (iii) the total mass of the binary system (M_{tot}). For the application to the periodic methanol masers, the period of the binary system is the same as the period of the periodic methanol masers as suggested in Chapter 1. In order to estimate the total mass of the system, observational evidence from Hofner et al. (1996) for the star in G9.62+0.20E suggests that the primary (main contributing

source which maintains the *ultra compact* HII region) is an early spectral type of B0. From the theoretical model of Sternberg et al. (2003), the mass of a B0 star is $\simeq 21\ M_{\odot}$. For the presence of a binary system reasonable assumptions have to be made for the parameters of the stellar companion. Surveys of e.g. Mason et al. (1998), with the focus on O and B eclipsing and visual binaries, show the mass ratio between the secondary and primary tends to be ≥ 0.5.

Thus, with this in mind, there are three possibilities that we can consider, (i) the primary and secondary are identical, in which case we assume the equivalent ionizing flux equal to that of a B0 star, (ii) the primary is a B0 star with mass $\simeq 21\ M_{\odot}$ (Sternberg et al., 2003), and the secondary somewhat less massive, and (iii) the mass of the secondary is considerably less than the primary, but still massive enough to produce strong stellar winds necessary for the hydrodynamical simulations. In the case of (i) the parameters in Sternberg et al. (2003) can be used to assume that two identical B0.5 stars with masses $\simeq 19\ M_{\odot}$ have the equivalent ionizing flux of one B0 star. For (ii) and (iii) a B0 star is used for the primary and a variety of masses can be used for the secondary. To this end, the range for the total mass of the binary system is taken to be between 30-40 $M_{\odot}$. The value of 40 $M_{\odot}$ is included for good measure, however, if we assume a B0 and B0.5 (for the 19 $M_{\odot}$ star) as the members of the binary system, the question arises as to whether the B0.5 star will have an influence on the HII region. For simplicity we assume that this will not be the case. The lower limit is set for the condition that the mass ratio is approximately ≥ 0.5, i.e. the mass of the secondary star varies between 9-19 $M_{\odot}$.

Let us assume possibility (i) in which case the binary system consists of two similar B0.5 stars of which the individual masses are $\simeq 19\ M_{\odot}$, translating to a total system mass of 38 $M_{\odot}$. From the CWB hypothesis, the time-dependent ionizing flux from the colliding stellar winds produce a "pulse" around periastron, i.e. suggestive of a relatively high eccentricity. The relatively high eccentricity will sufficiently modulate the ionizing flux between periastron and apastron to create the "pulse". Unfortunately, as discussed in Chapter 2 the boundary conditions of the 2D hydrodynamic simulation put an upper limit on the eccentricity, in that there is a minimum stellar separation distance between the stars (approximately 0.50 AU), where one or both of the shocks would be inside the remap radius (boundary condition) of the simulation. For the periods of the periodic masers considered here, that is with periods of 179 days, 196 days, 237 days, and 244 days respectively, the upper limits of the eccentricities are 0.76, 0.78, 0.80, and 0.81 respectively, for a system mass of 38 $M_{\odot}$.

The state of the shocked gas during the binary orbit was simulated at several discrete stellar separation distances, and the interval between these discrete separations is 0.1 AU. From Equation 2.8 the eccentricity can be determined if the periastron distance and period is known. Figure 3.1 shows the period of a binary system (with total system mass of 38 $M_{\odot}$) as function of eccentricity, for several different periastron distances between 0.5 AU and 1.2 AU. For a given periastron distance, the eccentricity can easily be obtained from Figure 3.1, for any orbital period. The

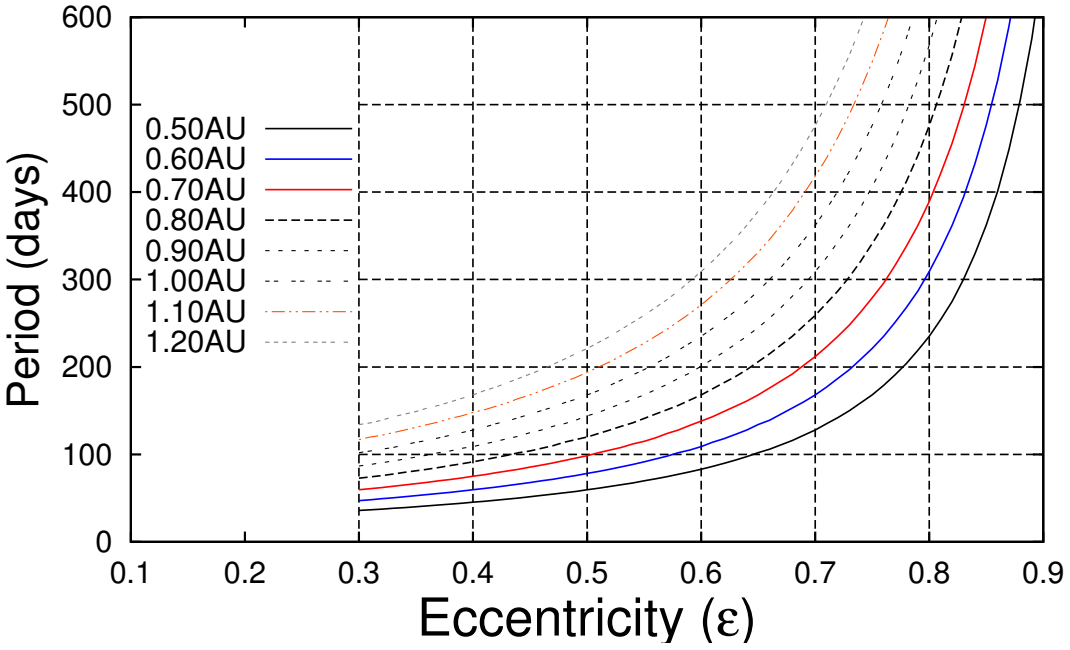

FIGURE 3.1: The period of a binary system as function of eccentricity for several periastron distances as indicated by the different colours which range between 0.50 AU and 1.20 AU. This was for a total system mass of 38 $M_{\odot}$.

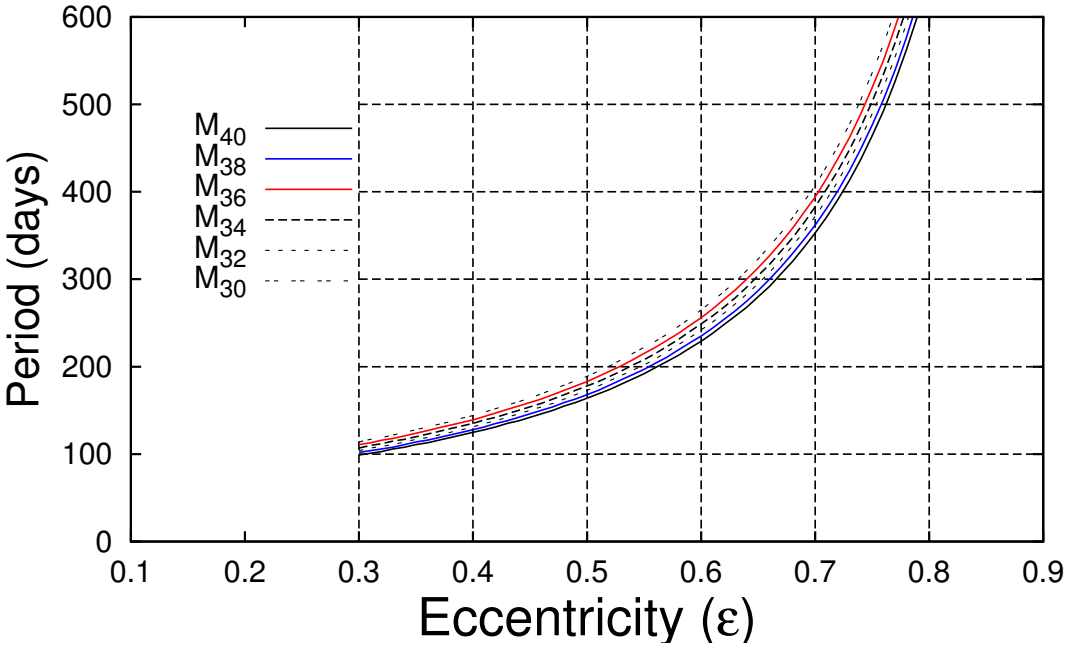

FIGURE 3.2: The period as function of eccentricity for several total system masses for a periastron distance of 1.00 AU.

binary orbit for a specific orbital period, eccentricity, and a chosen periastron distance can then be calculated. To show how the eccentricity of the system will change for the range of total system masses given above (30-40 $M_{\odot}$), Figure 3.2 shows the period as function of eccentricity for a periastron distance of 1.0 AU, where the system mass ranges between $30M_{\odot}$ and $40M_{\odot}$

with $2M_{\odot}$ intervals. For a lower system mass the eccentricity decreases and vice versa for a higher system mass from the $P \propto M_{tot}^{-1/2}$ dependence. As the above description was only for the source G9.62+0.20E with an assumed B0-B0.5 star, the other sources which will be investigated may possibly have different stellar types associated with them, thus the total system mass may also differ. For higher system masses the orbit will change with the period-mass dependence.

3.3 Stellar parameters and the shocked gas properties

First, the parameters used for the stars in the hydrodynamical simulations are given in Table 3.1. Three different combinations of mass-loss rates for the primary and secondary were used to simulate the colliding winds, given in Table 3.1 as models CWB1, CWB2, and CWB3. The stellar wind velocities were taken from observational results (Bernabeu et al., 1989), and theoretical considerations (Sternberg et al., 2003) of O and B type stars. From the observations of Bernabeu et al. (1989), the observed range of stellar wind speeds of B0V-O8V stars overlap to a large extent, of which the velocities are $\simeq (1670 \pm 610)$ km s^{-1} for stars associated with clusters/associations. Thus, for the type of sources we consider in this thesis for which we have only approximate stellar types, the stellar wind speeds should be consistent with these observations, and we choose two stellar wind speeds within the abovementioned velocity range. The theoretical models of Sternberg et al. (2003) and Vink et al. (2000) predicts the mass-loss rate from radiation-driven stellar atmospheres. These mass-loss rate predictions are, however, dependent on stellar wind speed, luminosity, stellar mass, and surface temperature. Variations in these parameters should lead to a wide variety of stellar properties within a given stellar type. The three mass-loss rate combinations which we have chosen are given in Table 3.1. The assumed mass-loss rates are higher than what the models of Sternberg et al. (2003) and Vink et al. (2000) predict. The reason for this is, where G9.62+0.20E is situated for example in the molecular ring (Sanna et al., 2009), the chemical abundance may be enhanced and from Vink & de Koter (2005, and references therein) this may result in higher mass-loss rates. Additionally, some of these star forming regions may still harbour a swollen pre-main sequence star and, according to Hosokawa & Omukai (2008), may lead to an enhanced mass-loss rate due to convection effects in the stellar interior.

From the approach followed with the hydrodynamical simulations, as discussed in Chapter 2, there are a few remarks to be made. To simplify our model, it was assumed that the colliding winds have already been set up, i.e. we investigate an already existing colliding wind binary system with the shocked wind in equilibrium. From the 2D simulations, the shocked gas reaches an equilibrium state after a simulation time of approximately 3×10^6 seconds for adiabatic cooling conditions. For an eccentric orbit, the shocked gas should display adiabatic behaviour for the largest part of the orbit. While the shocked gas behaves adiabatically, it should react

Variables (units)	CWB 1	CWB 2	CWB 3
$M_{\star,1}$ ($M_\odot$)	19	19	19
$M_{\star,2}$ ($M_\odot$)	19	19	19
$\dot{M}_1$ ($M_\odot$ yr^{-1})	1.0×10^{-6}	9.0×10^{-7}	8.0×10^{-7}
$\dot{M}_2$ ($M_\odot$ yr^{-1})	8.0×10^{-7}	6.0×10^{-7}	6.0×10^{-7}
v_1(cm s^{-1})	1.6×10^8	1.6×10^8	1.6×10^8
v_2(cm s^{-1})	1.2×10^8	1.2×10^8	1.2×10^8
η	1.29	1.41	1.33
$\chi_{1,min}$	4.92	5.46	6.14
$\chi_{2,min}$	1.94	2.59	2.59

TABLE 3.1: This table shows the parameters of the winds for the three different CWB models. Here η is the momentum flux ratio, as calculated by equation 2.9. The values $\chi_{1,min}$ and $\chi_{2,min}$ are the minimum values of the cooling parameter for the individual winds for a periastron distance of 0.50 AU.

fast enough to the change in stellar separation, such that a simulation time of 3×10^6 seconds should represent the time dependent state of the shocked gas. However, in the case that the shocked gas becomes radiative or partly radiative around periastron, there is not an "equilibrium" state. For this reason, the simulation time was extended beyond 3×10^6 seconds, and several states ("snapshots") were used to determine a statistical average to represent the shocked gas for radiative conditions. To be consistent, this approach was also applied to the adiabatically cooling shocked gas. Figure 3.3 illustrates the states of the shocked gas states for several stellar

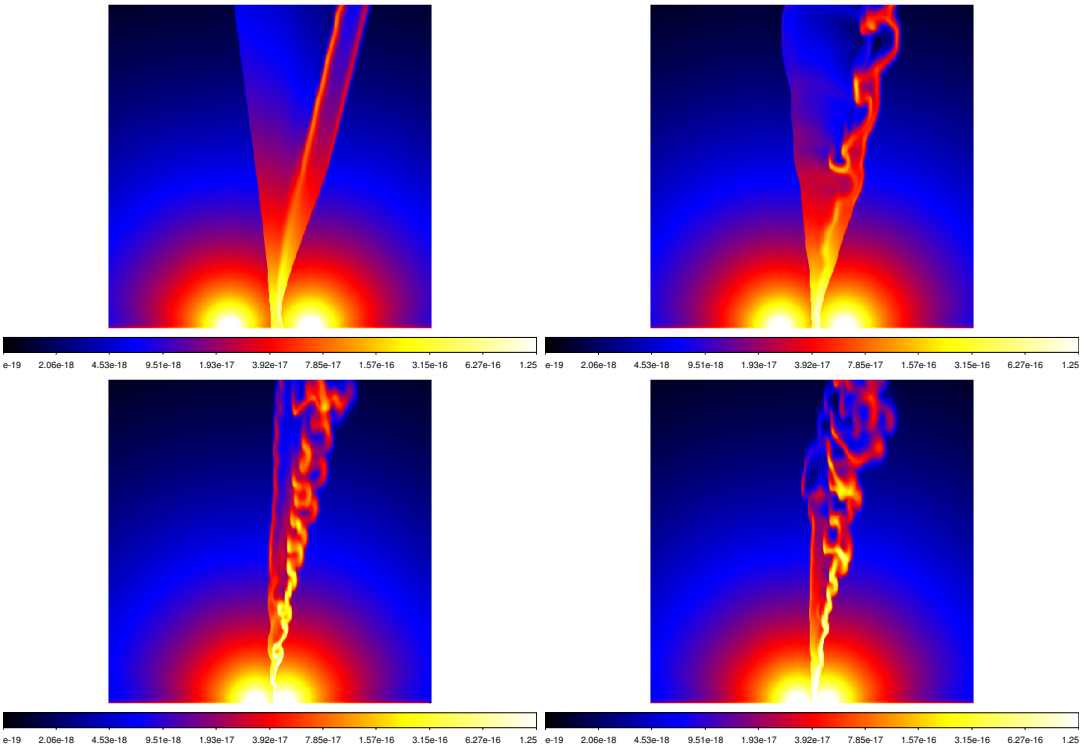

FIGURE 3.3: This figure shows the density profiles of the shocked gas from the hydrodynamic simulations for different stellar separations. Top left: the density profile for a separation of 2.50 AU. Top right: a separation of 2.00 AU. The top panels are both for adiabatic conditions, however in the right panel the Kelvin-Helmholtz instabilities are visible. Bottom panels: the density profiles for a stellar separation of 0.90 AU, for different times during the simulation.

separations. The top left panel shows a smooth flow for a stellar separation of 2.50 AU. The top right panel (for a stellar separation of 2.00 AU) shows signs of Kelvin-Helmholtz instabilities, due to velocity shear across the contact discontinuity. The bottom panels show example states for the shocked gas, where radiative cooling has started to influence the shocked gas. These panels represent a stellar separation of 0.90 AU at two different simulation times, 3×10^6 sec (left panel) and 7.5×10^6 sec (right panel), which shows changes in the shocked gas due to the thermal instabilities caused by radiative cooling, and which shows that there is no equilibrium.

The ultimate aim of the simulation of the shocked gas of the CWB, is to determine how the SEDs produced from the shocked gas will influence the ionization front of the HII region, if at all. The properties of the shocked gas, i.e. density, temperature, and volume governs the SED produced from the shocked gas, so it is necessary to give a brief description of how these properties change as the stellar parameters change. This will be done for both adiabatically - and radiatively cooling gas.

3.3.1 The behaviour of adiabatic cooling gas

The three important properties of the shocked gas are the density, volume and temperature. From the Rankine-Hugoniot jump conditions, the temperature of the shocked gas for each wind should obey the relation $T_s = 3\overline{m}v_w^2/16k$. For the stellar wind velocities from Table 3.1, and $\overline{m} = 1.02 \times 10^{-24}$ g for the mean mass per particle for ISM abundances, the temperature of the shocked gas on either side of the CD is $\approx 3.5 \times 10^7$ K and $\approx 2.0 \times 10^7$ K, respectively. This was confirmed from the numerical simulations. As we are interested in the emission from the shocked gas between 0.01 - 10 keV, we investigate the properties of the shocked gas for temperatures between the maximum temperature (determined by the Rankine-Hugoniot jump conditions for the faster wind) and the minimum temperature (1.5×10^5 K, approximately the hydrogen ionizing threshold temperature). Temperatures below $\simeq 1.5 \times 10^5$ K, have been shown to have a negligible contribution to the emission in this energy range (Dougherty et al., 2003).

For the density and the volume of the shocked gas at the line of centers there are two effects to take note of: (1) the r^{-2} dependence of density, and (2) the volume of the shocked gas as function of stellar separation as determined by the ideal gas law ($PV = nkT$). If the stellar separation decreases/increases the density of the shocked gas will increase/decrease. This is shown in the bottom panel of Figure 3.4, where the largest stellar separation (2.80 AU, the dashed black line) has the lowest density at the highest temperature (on the right hand side), and as the stellar separation decreases the density increase. For the volume of the shocked gas at the line of centers, the temperature is constant from the Rankine-Hugoniot jump conditions. Thus, from the ideal gas law increasing/decreasing the density will have an effect on the pressure and volume

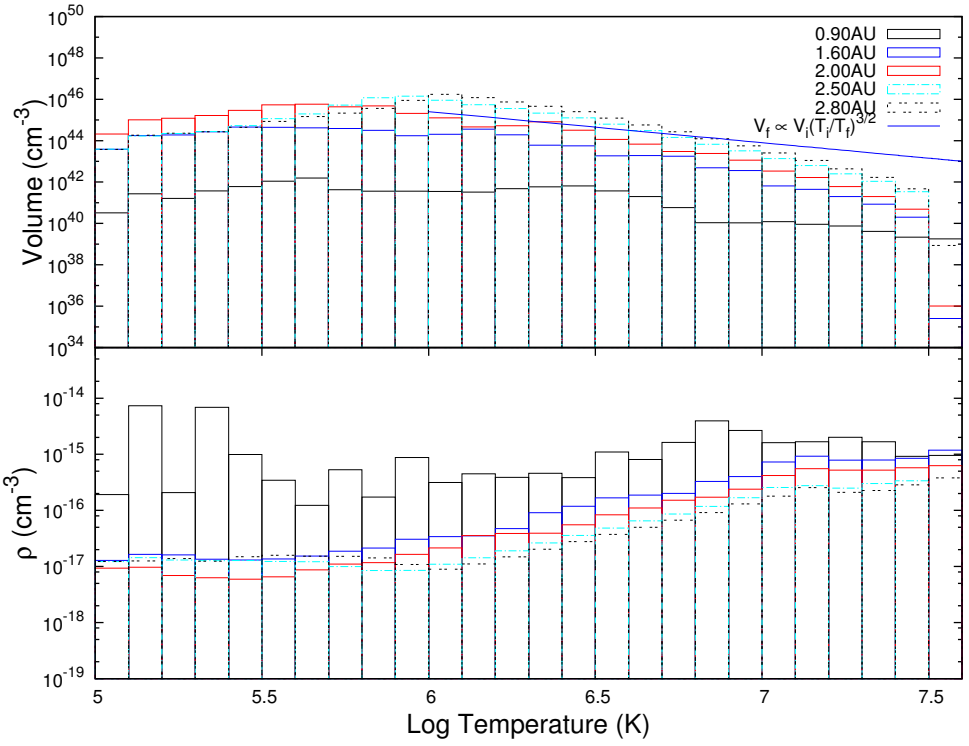

FIGURE 3.4: Top panel: a histogram showing the volume of the shocked gas as function of temperature for several separation distances. Bottom panel: a histogram showing the corresponding density as function of temperature for the same separation distances.

of the shocked gas, as the shocked gas at the line of centers is essentially an isotherm. Increasing/decreasing the density will lead to an increased/decreased pressure and decreased/increased volume. For a large stellar separation the volume of the shocked gas at the line of centers will be the largest, and the volume will decrease as the stellar separation decreases. This is shown in the top panel of Figure 3.4, where the dashed black line has the largest volume (on the right hand side), and the volume decreases as the stellar separation decreases.

The adiabatic expansion of the shocked gas follows the adiabatic relations, $P_i V_i^{5/3} = P_f V_f^{5/3}$ and $T_i V_i^{2/3} = T_f V_f^{2/3}$ with $\gamma = 5/3$, and the adiabatic relation between temperature T and volume V is shown by the blue line in the top panel. It shows that the volume of the shocked gas follows the general behaviour during adiabatic expansion. However, below a temperature of 10^6 K, this relation no longer holds, as the volume no longer follows the adiabatic relation between T and V. This behaviour is most likely due to the sudden increase in the temperature-dependent cooling rate at this temperature (see Figure 2.5). The bottom panel shows how the density in the shocked gas decreases as the volume increases, and as the volume decreases below its expected adiabatic behaviour at a temperature of 10^6 K so does the density, where the density increases due to the decreased volume. This is shown only for one mass-loss rate combination, increasing/decreasing the mass-loss rate will only increase/decrease the density in the shocked gas.

3.3.2 The behaviour of radiative cooling gas

When radiative cooling becomes important (normally in the case of orbital periods of a few days or highly eccentric binary systems) the shocked gas will no longer behave adiabatically. For a stellar separation of 0.90 AU, as shown in Figure 3.4 this is an example of shocked gas cooling radiatively. The volume and density at the line of centers still behaves according to the ideal gas law, the volume is the smallest (the black line in the top panel of Figure 3.4), and the density is the highest (black line in the bottom panel). The effect of radiative cooling is, however, clearly visible in Figure 3.4. The effect of radiative cooling manifests itself as an increased density at lower temperatures above the expected value in the adiabatic case, as seen in the bottom panel of Figure 3.4. The gas at a high temperature cools to a lower temperature but the gas still has its associated density. This results in an increased density at lower temperatures, which is seen in the bottom panel of Figure 3.4.

As described in Section 2.4.1, the emission from the shocked gas depends on the density and the temperature. Thus, for adiabatic cooling and its behaviour shown in Figure 3.4, the emission will increase/decrease as the density increases/decreases. If the expansion is purely adiabatic, we expect the temperature dependent density to linearly increase/decrease as the stellar separation is decreased/increased. The emission should show the same behaviour, and the flux of the SED calculated from the shocked gas will increase/decrease as the stellar separation decreases/increases. However, for radiative cooling the higher temperature gas (with its associated high density close to the line of centers) cools to lower temperatures, and we expect an increased flux at lower energies because of the increased density. The last aspect to mention, is that as discussed earlier, we use an average of several "snapshots" of the shocked gas to represent the time dependent conditions in the shocked gas for the CWB model. This is done for both radiative cooling and adiabatic cooling conditions of the shocked gas to be thorough. Thus, how will the emission from the shocked gas change (SED or luminosity) for adiabatic cooling or radiative cooling conditions at different simulation times? In the next section we will show the calculated SEDs.

3.4 Emission spectra and Luminosity

As already mentioned, the SEDs of several states of the shocked gas were used to calculate an average SED from the shocked gas for every stellar separation, as the shocked gas for radiative cooling conditions continuously changes the properties of the shocked gas. This is done in order to obtain a single SED and luminosity for every stellar separation used in the CWB model.

First, in Figure 3.5 it is shown how the luminosity of the shocked gas changes with simulation time, for several stellar separations, including stellar separations exhibiting radiative cooling. For

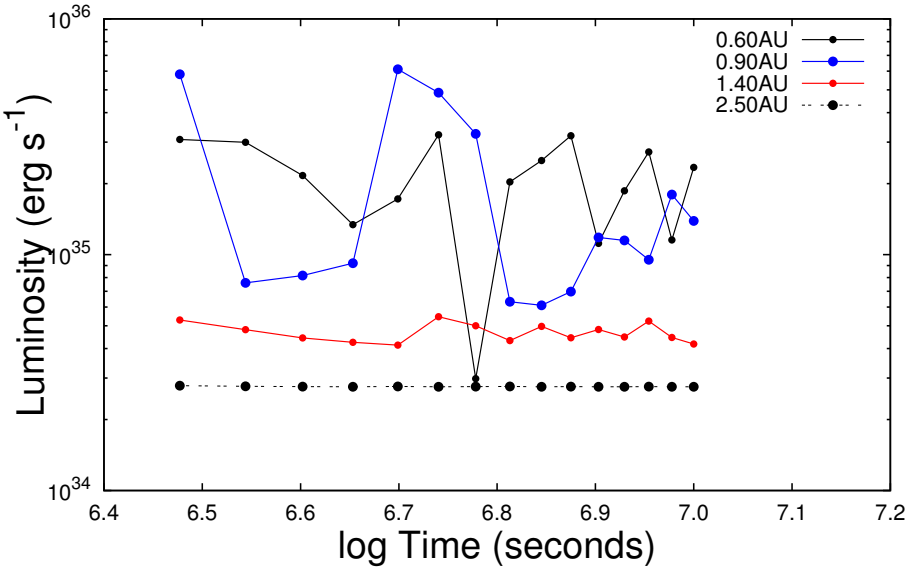

FIGURE 3.5: The calculated luminosity of the shocked gas for each "snapshot", for four different stellar separations, 0.6 AU, 0.9 AU, 1.4 AU and 2.5 AU respectively. For adiabatic conditions (2.5 AU) the luminosities are identical. For the transition between adiabatic and radiative cooling (1.4 AU) the luminosities start to differ, and for radiative cooling (0.6 AU and 0.9 AU), the luminosities differ significantly from "snapshot" to "snapshot".

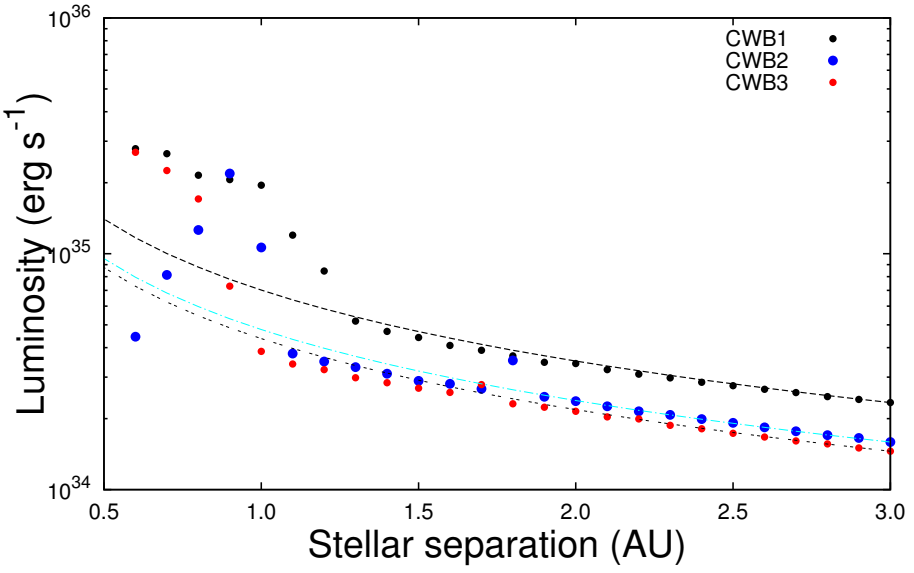

FIGURE 3.6: The luminosity of the shocked gas for stellar separations of 0.6 AU to 3.0 AU. The different colours are for the three different CWB models as given in Table 3.1. For all three models, the L $\propto D^{-1}$ relation is plotted on the simulated results and show that the adiabatic behaviour holds. For the individual models the rapid increase in luminosity occurs at different stellar separations, expected from the cooling parameter χ.

a stellar separation of 2.5 AU (adiabatic) the luminosity stays unchanged with simulation time. On the other hand, as the stellar separation decreases the luminosity of the shocked gas starts to change with simulation time (see the stellar separation of 1.4 AU). For stellar separations of

0.6 AU and 0.9 AU , where radiative cooling definitely plays a role, the luminosities are widely different for different simulation times. From this result it is clear that an average have to be used to represent the shocked gas for radiative cooling conditions. Secondly, for adiabatically cooling gas the $L \propto D^{-1}$ dependence should hold. The luminosities from several stellar separation are shown for the three CWB models in Figure 3.6. The $L \propto D^{-1}$ relation for the three CWB models is shown with respect to a stellar separation of 3.0 AU. There is a slight deviation from the adiabatic behaviour at stellar separations of 1.0 AU - 2.0 AU, for the different CWB models. This is possibly due to the influence of the early onset of radiative cooling effects (a transition region). When the shocked gas starts to cool radiatively, the luminosity starts to increase suddenly as shown in Figure 3.6. The stellar separations where this starts for the three different mass-loss rate combinations are 1.3 AU (CWB1), 1.1 AU (CWB2), and 1.0 AU (CWB3). The shocked gas for CWB2 collapses into a thin shell due to radiative cooling and the luminosity decreases as the stellar separation decreases below 0.9 AU. For this reason CWB2 will not be used further in this work. The luminosities of the shocked gas in the adiabatic regime are between $\log L = 34.37 - 34.71$ (3.0 AU - 1.3 AU) for CWB1 and between $\log L = 34.16 - 34.59$ (3.0 AU - 1.0 AU) for CWB3. In the radiative regime at a stellar separation of 0.6 AU the luminosity is $\log L = 35.45$ for CWB1 and $\log L = 35.43$ for CWB3.

The luminosities for the three CWB models in the adiabatic cooling limit can be described with Equation 2.17, rewritten as:

$$\frac{L_{s,2}}{L_{s,1}} \approx \left(\frac{\dot{M}_2}{\dot{M}_1}\right)^2 \left(\frac{v_2}{v_1}\right)^{-3} \left(\frac{D_2}{D_1}\right)^{-1} \left(\frac{(1+\eta_2)\eta_1^4}{(1+\eta_1)\eta_2^4}\right), \tag{3.1}$$

where the symbols have their previously designated meaning, and the subscripts 1 and 2 are for the initial and new parameters for the wind, respectively. From the D^{-1} dependence of the luminosity, for the same mass-loss rate, the flux of the SED with the smallest stellar separation will have the highest flux, as seen from the ratio in the middle right panel of Figure 3.7, and vice versa. Equation 3.1 provides a generalized equation to describe the luminosity if any stellar parameters were to be changed in the adiabatic limit, with respect to some reference luminosity. For the case where the shocked gas is subjected to radiative cooling, the luminosity cannot be described by this equation, as discussed in Section 2.3.2.3. For radiative cooling the flux is enhanced at low energies, as shown in the bottom left panel of Figure 3.7. Although this behaviour holds for all three CWB models, it commences at different stellar separations, governed by the cooling parameter χ as shown in Figure 3.6.

To investigate the behaviour of the SEDs produced from the shocked gas, SEDs in the adiabatic regime will first be compared to each other. Second, SEDs from the adiabatic regime will also be compared with SEDs in the radiative regime. This is done to show that there are significant

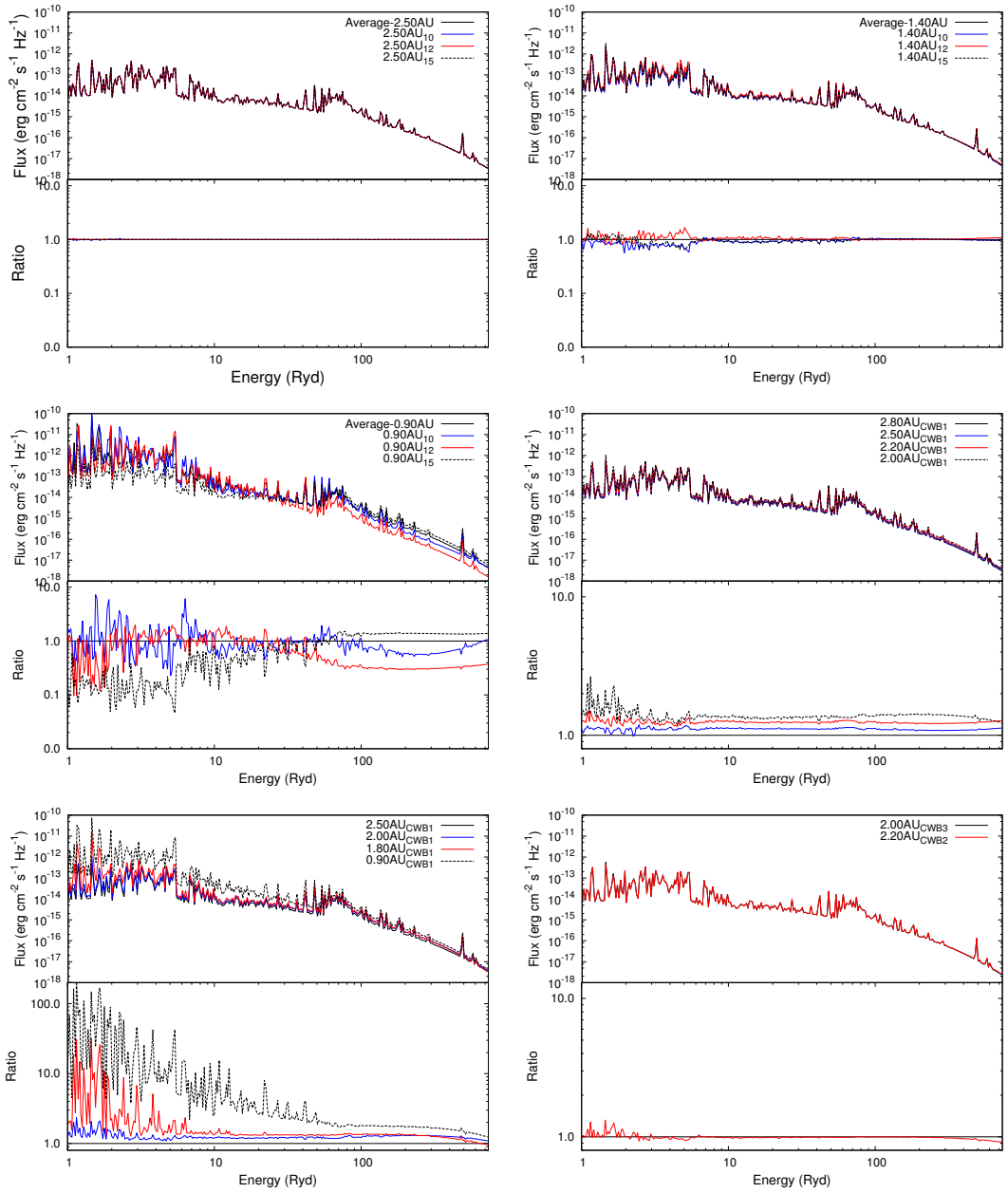

FIGURE 3.7: Top left panel: here the average SED of a stellar separation of 2.5 AU is compared with the SEDs at different simulation times. Top right panel: here the average SED for a stellar separation of 1.4 AU is compared with the SEDs at different simulation times. Middle left panel: here the average SED for a stellar separation of 0.9 AU is compared with the SEDs at different simulation times. Middle right panel: here the average SEDs of four different stellar separations in the adiabatic regime for model CWB1 are compared. Bottom left panel: here the average SED of radiatively cooling gas is compared with three SEDs of adiabatically cooling gas, for model CWB1. Bottom right panel: here two average SEDs (with the same luminosity for different stellar separations) are compared. The subscripts indicate the number of the "snapshot" used. The "snapshots" have 5×10^5 second intervals from the initial condition with subscript 0.

differences in the SEDs for adiabatic and radiative cooling cases. First, for a stellar separation of 2.5 AU, the average SED is compared to SEDs at different simulation times. This is shown in the top left panel of Figure 3.7. The average SED and the SEDs of different simulation times are

identical. The subscripts in the legends of Figure 3.7 indicates the number of the "snapshot", where each "snapshot" represents a simulation time with 5×10^5 sec intervals, and the subscript 0 is the initial condition. For a stellar separation of 1.4 AU, which is in the transition region (shown in the top right panel), there are slight differences between the average SED and the SEDs at different simulation times. On the other hand, the middle left panel shows the SEDs for a stellar separation of 0.9 AU, there is clearly a large difference between the average SED and the SEDs at different simulation times. These changes may influence the solution of the CWB model for consecutive flares, if it is necessary to fit the CWB model with a periastron distance in the radiative regime. The SEDs of different stellar separations in the adiabatic regime is shown in the middle right panel of Figure 3.7. From the ratio between the SEDs it shows that the flux increases as the stellar separation decreases, however, there are slight variations in the SEDs with an enhancement at low energies. The bottom left panel shows the average SED for a stellar separation of 0.9 AU in the radiative regime and three SEDs in the adiabatic regime and transition region (1.8 AU) to show how they compare. The SEDs in the adiabatic regime have much lower fluxes at low energies than the SED in the radiative regime, and the SED in the transition region also show an enhanced flux at low energies. The enhanced low-energy flux in the radiative regime should have a considerable influence at the ionization front, as the low energy photons above 13.6 eV are predominantly responsible for the ionization of hydrogen.

Something to note is that as each wind has its own χ value, the secondary wind starts to suffer from radiative cooling before the primary (for a weaker secondary wind momentum). This is probably the reason for the transition from adiabatic to radiative conditions of the SEDs. Lastly, from Equation 3.1 we can obtain the same luminosities from the shocked gas, for different mass-loss rates. For model CWB2 for a stellar separation of 2.2 AU and model CWB3 for a stellar separation of 2.0 AU, the luminosities are identical. The bottom right panel of Figure 3.7 shows the SEDs of these cases, and they are almost identical except for small differences.

From the description given above, we want to investigate how the different SEDs (both for adiabatically cooling and radiative cooling gas) will influence the ionization front when the individual shocked gas SEDs are added to the stellar SED. In the next section the results of these simulations will be shown.

3.5 The photo-ionization simulations

As mentioned above, we want to determine whether the position of the ionization fronts of these simulated HII regions will be influenced if the SEDs from the shocked gas are added to the stellar SED. To this end, the HII regions simulated using only the stellar radiation field are used as reference positions. It is expected that the environments of massive stars at least have

ISM abundances, for this reason a brief description is given to show how the structure of HII regions would be influenced if heavier elements than hydrogen were to be added. The further calculations includes the complete ISM abundance set of *Cloudy*, as heavier elements such as helium should have an influence on the size of the HII region and possibly on the results.

3.5.1 The influence of adding heavy elements

In Chapter 2 the evolution of an HII region was described using the approximation of a pure hydrogen gas. The influence that heavier elements will have was briefly discussed in Section

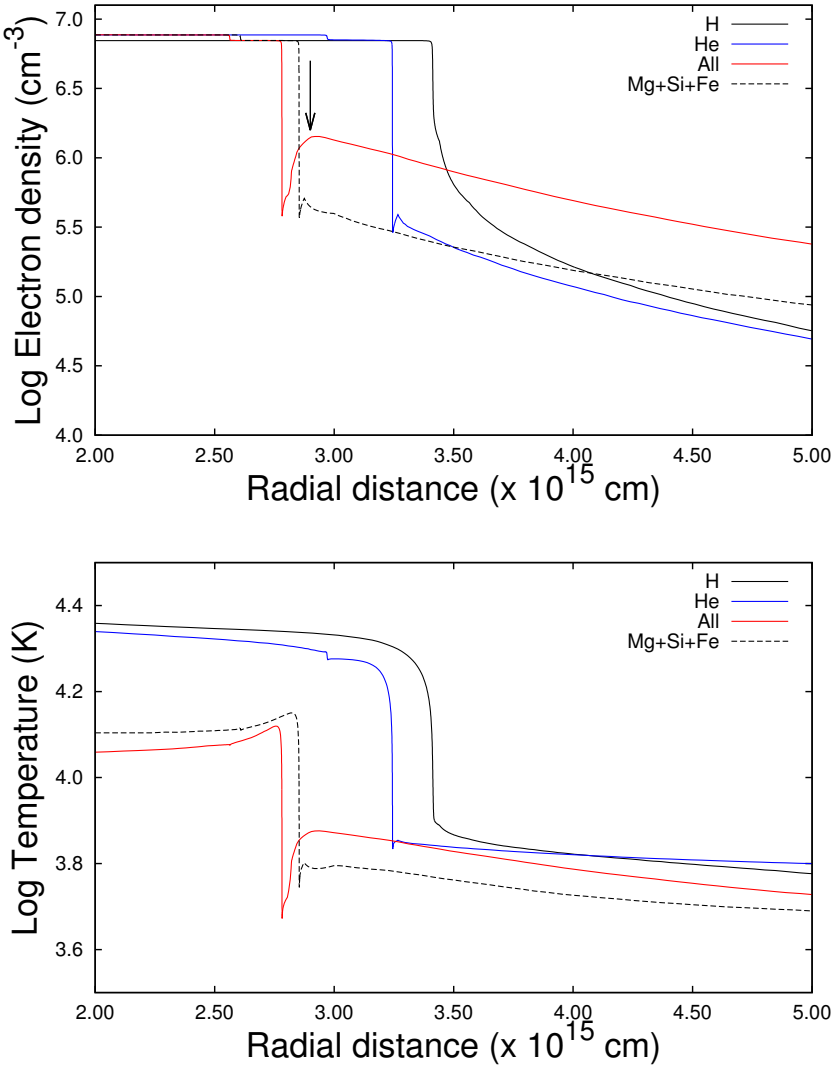

FIGURE 3.8: Top panel: radially dependent electron density for the simulated HII regions. The black line represents a pure hydrogen gas, the blue line when helium is added, the red line for interstellar medium abundances, and the dashed black line for the changed abundances of Mg, Si, and Fe. It shows that the size of the HII region decrease as heavy elements are added. Bottom panel: radially dependent temperature of the simulated HII region. The legend corresponds to that of the top panel.

Element	log(Relative Abundance)
Hydrogen	0
Helium	-1.01
Carbon	-3.60
Nitrogen	-4.10
Oxygen	-3.50
Neon	-3.91
Magnesium	-4.90
Silicon	-5.50
Sulphur	-4.49
Chlorine	-7.00
Argon	-5.50
Iron	-6.20

TABLE 3.2: Here the interstellar abundance set from *Cloudy* is given, with relative abundance given as $\log(n_X/n_H)$, where n_H is the density of hydrogen, and n_X is the density of e.g. helium, oxygen, etc.

2.5.2, i.e. in terms of the change in size and temperature of the ionized region. Figure 3.8 shows the electron density as a function of radial distance in the vicinity of the ionization front as calculated with *Cloudy*. The calculation was done for a pure hydrogen HII region, for hydrogen and helium and for the full ISM abundance set of *Cloudy*. In Table 3.2 the logarithm of the relative abundance of heavy elements (including helium) to hydrogen is given.

It is seen in the top panel of Figure 3.8 that the addition of heavy elements considerably decreases the size of the HII region. This is explained by the fact that elements such as helium and oxygen have ionizing potentials close to that of hydrogen but with cross sections an order of magnitude higher (see e.g. Osterbrock, 1989), so that a significant fraction of stellar photons is absorbed by helium and heavier elements rather than hydrogen. This causes a decrease in the number of photons ionizing hydrogen, which results in a smaller Strömgren radius. This abundance set was taken from the ISM abundance set of *Cloudy* (Ferland et al., 1998). It is shown in Figure 3.8 that as helium (blue line) and the rest of the heavier elements (red line) are added, the electron density outside of the ionization front of the HII region increase with respect to a pure hydrogen (black line) HII region. For the complete abundance set (red line) it is unclear as to what causes the increase in the electron density (indicated with the arrow). According to **?**, and references therein) temperatures of $\sim$ 10-20 K (Bontemps et al., 2010) inside molecular clouds provide the optimal environment for grain formation, and the formation of grains depletes the gas phase abundance of mainly Mg, Si and Fe. The shell-like morphologies of many compact HII regions as seen in the *Mid-Infrared* (MIR) emission (see for example Phillips & Ramos-Larios, 2008), suggests that some of the dust has been cleared out of the ionized volume either through destruction or by radiation pressure. However, there may still be significant amounts of dust inside the HII region, as found by De Buizer et al. (2003) from MIR emission associated with G9.62+0.20E (one of the periodic sources investigated here). Thus, in the vicinity of the ionization front of the HII region (especially far from the star), the destruction of dust may

not be important and the abundance of Mg, Si, and Fe may be low. **?**) demonstrated that these elements should be detectable in ultraviolet or optical spectra. Observations towards HII regions show that these elements are depleted by 1-2 orders of magnitude (Osterbrock et al., 1992, Esteban et al., 1998). We implement the possibility that these elements are still depleted from the gas phase, by decreasing the relative abundance of Mg, Si, and Fe by an order of magnitude, the result of which is shown by the dashed line in Figure 3.8. The considerable increase in the electron density outside the ionization front for the original abundance set disappears when the relative abundance of these three elements is decreased by an order of magnitude. The implications of this result on the radiative transfer calculations will be shown and discussed in the next section. The temperature of the HII region will also be influenced as the heavy elements are included to the photo-ionization calculations of *Cloudy*, as discussed in Section 2.5.2.

3.5.2 Influence of the shocked gas SEDs on the ionization front

As described in the previous section, the SEDs produced from the shocked gas that primarily cools adiabatically differ from those where radiative cooling dominates. The main difference is seen in the flux at low energies just above the hydrogen ionizing threshold. The SEDs produced from the shocked gas in the radiative regime show an increased flux of up to two orders of magnitude with respect to an example SED with adiabatic conditions (see the bottom left panel of Figure 3.7). For the case of SEDs in the adiabatic regime, Figure 3.9 show several results of the influence of the additional emission from the shocked gas on the ionization front obtained from *Cloudy*. It shows that the SEDs produced from gas that cools adiabatically do not influence the position of the ionization front considerably (in the order of 10^{11} cm). Closer inspection shows there are also results that show that the ionization front might even move backwards towards the star for an additional shocked gas SED (see the dashed line for a stellar separation of 2.5 AU). This suggests that there might be a level of uncertainty to the solutions from *Cloudy*, or that some of these SEDs may have specific features that influence the solution due to physical processes in the HII region. As given earlier, the luminosities of the shocked gas in the adiabatic regime for model CWB1 range between log L = 34.37 - 34.71 and log L = 34.16 - 34.59 for CWB3. The immediate implication of these results is that in the regime that the shocked gas only cools adiabatically, it will most probably not be able to explain the periodic variability of the methanol masers within the framework of our hypothesis. This also has consequences for the simple model of van der Walt (2011), because he only considered adiabatically cooling gas.

For the shocked gas dominated by radiative cooling, with the SED showing an increased flux at lower energies (shown in the bottom left panel of Figure 3.7), the influence on the ionization front considerably increases with respect to the adiabatic case to up to $\simeq 2.7 \times 10^{12}$ cm (0.18 AU). This is shown in Figure 3.10. These results are for a B0 star and a hydrogen density of 7

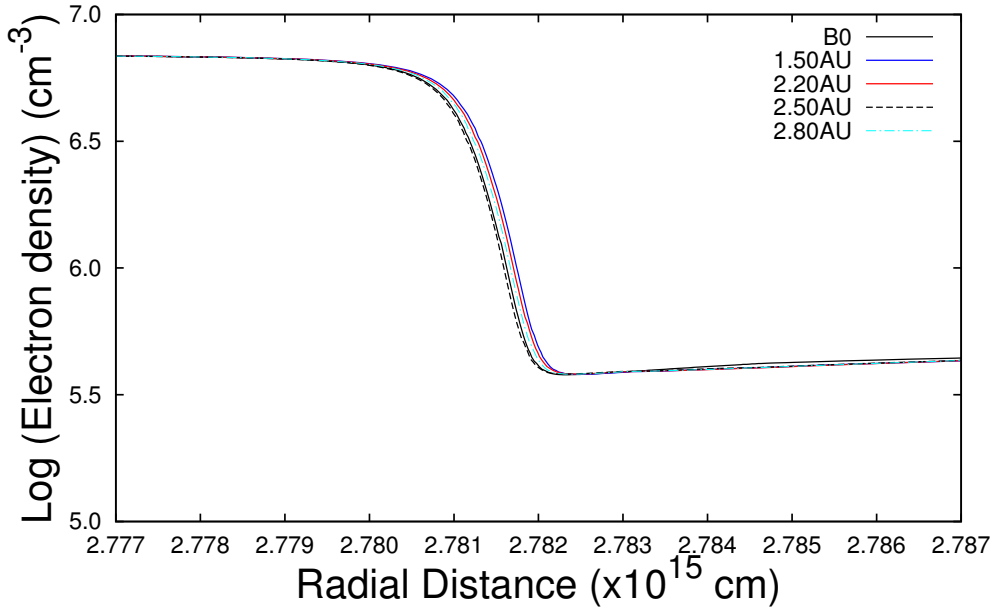

FIGURE 3.9: The resulting positions of the ionization front for several adiabatic SEDs, and the reference position (black line) of the ionization front produced from the star alone (black body).

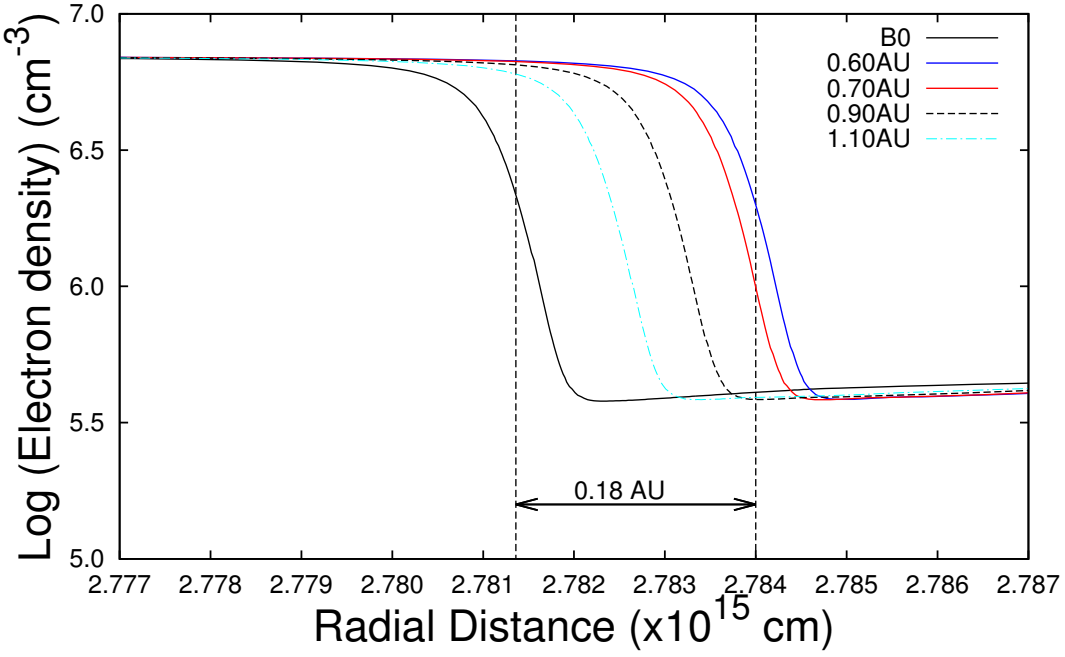

FIGURE 3.10: The resulting positions of the ionization front for several radiative SEDs, as well as the ionization front for the star alone (black body).

$\times 10^6$ cm^{-3}. The luminosities which resulted in these changes in the position of the ionization front are log $L = 35.45$ (0.6 AU), log $L = 35.42$ (0.7 AU), log $L = 35.31$ (0.9 AU), and log $L =$

Spectral type	Surface Temperature (T_{eff})	Density (cm^{-3})	log(Q(H) s^{-1})
B0	33340	4-7 × 10^6	48.02
O9.5	34900	4-7 × 10^6	48.29
O9	35900	4-7 × 10^6	48.47
O8.5	37170	4-7 × 10^6	48.61
O8	38450	4-7 × 10^6	48.75

TABLE 3.3: The stellar parameters of the stars that were used to simulate the HII regions, e.g. spectral type, surface temperature, and log($Q(H)$) s^{-1} as taken from Sternberg et al. (2003), and several assumed hydrogen densities for the cloud in which the stars reside.

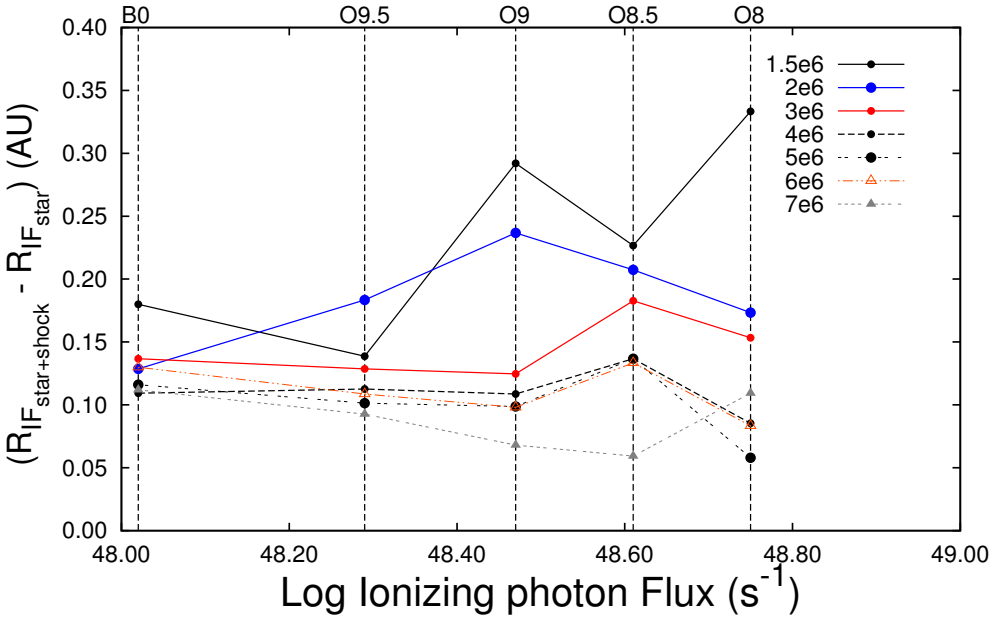

FIGURE 3.11: The influence on the ionization front from the shocked gas SED for a stellar separation of 0.90 AU for model CWB1 (dashed line in Figure 3.10, for several densities and stellar types.

35.08 (1.1 AU). However, both for the abovementioned adiabatic cooling case and the radiative cooling case, this is only for a constant hydrogen density of 7 × 10^6 cm^{-3}.

Let us investigate how the influence on the ionization front will change for different densities and stellar types. For this, we use the example SED generated from the shocked gas for the stellar separation 0.90 AU with a luminosity of log L = 35.31, and the use of an B0 star. For the case of a constant hydrogen density of 7 × 10^6 cm^{-3}, the ionization front is shifted outward with approximately 1.7 ×10^{12} cm, i.e. ∼ 0.11 AU. Figure 3.11 show the results for the influence on the ionization front for several different densities and stellar types. For a density of 7 ×10^6 cm^{-3}, the influence decreases as the stellar flux increases and suddenly increases for a O8 star. As seen, the same increase happens for a O8.5 star for lower densities after which it decreases again for a O8 star. For an even lower density of 2 ×10^6 cm^{-3} the maximum influence shifts to a O9 star, and for a density of 1.5 ×10^6 cm^{-3} it decrease from a O9 to a O8.5 and then increase again for a O8 star.

There are three factors that play a role in what we see in Figure 3.11. First, consider Equation 2.37 given by

$$R_S = \left(\frac{3S_\star}{4\pi n^2 \beta_2} \right)^{1/3}, \tag{3.2}$$

and the definition of optical depth ($\tau = \sigma_\nu nl$), where σ_ν is the photo-ionization cross-section, n the neutral density, and l the path length. We set l equal to the Strömgren radius, and we assume densities of $n_1 = 7 \times 10^6$ cm^{-3} and $n_2 = 1 \times 10^6$ cm^{-3}. From $R \propto n^{-2/3}$, it follows that $R_2/R_1 = 3.65$, for densities n_1 and n_2. For these parameters, $\tau_2 \simeq 0.5\ \tau_1$ at a given frequency, because $\tau_2 = 3.65\sigma_\nu R_1 n_2$ and $\tau_1 = 7\sigma_\nu R_1 n_2$. Thus, the optical depth decreases as the density decreases, this should cause an increased influence at the ionization front as the density decreases, shown in Figure 3.11. Second, since R_S increases as the density decreases, the r^{-2} dilution of the flux of the ionizing photons from the shocked gas should start to play an important role at large distances from the stars, minimizing the influence of the ionizing photons from the shocked gas on the ionization front. This is seen in Figure 3.11 from the decrease of the influence for the densities 3 - 6 $\times 10^6$ cm^{-3} for an O8 star, because the optical depth is still relatively high.

Lastly, the more massive the star, the more ionizing photons it produces above the helium ionizing potential of 24.6 eV. As a consequence, the helium ionization front will be located closer to the hydrogen ionization front as shown in Figure 3.12 for an B0, O9, and O8 star, respectively.

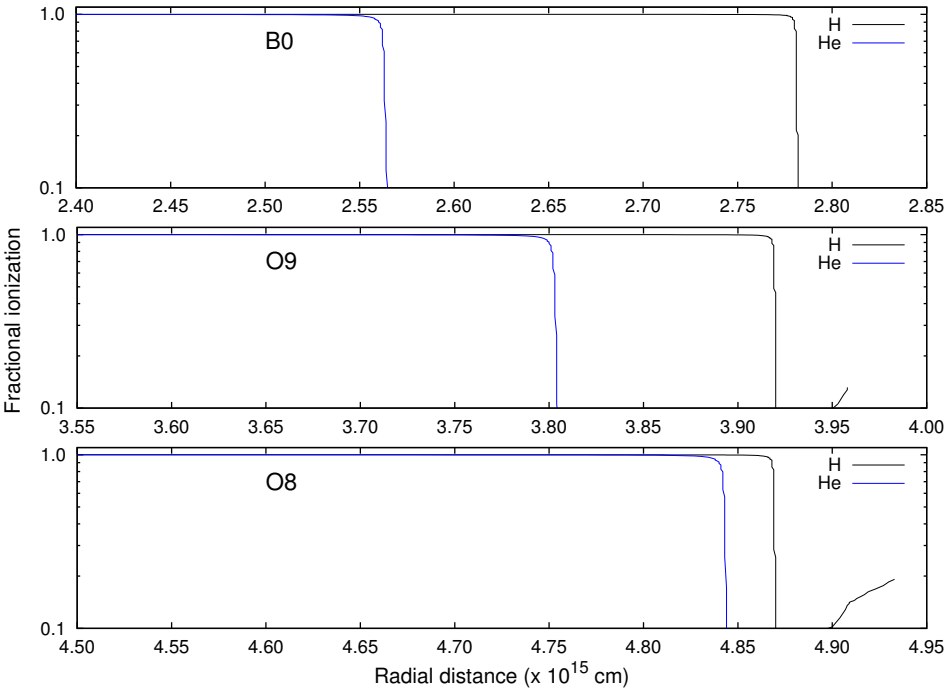

FIGURE 3.12: Here the radially dependent fractional ionization is given for both hydrogen (black line) and helium (blue line), for a B0, O9 and O8 star. It shows that the helium ionization front forms closer to the hydrogen ionization the more massive the star.

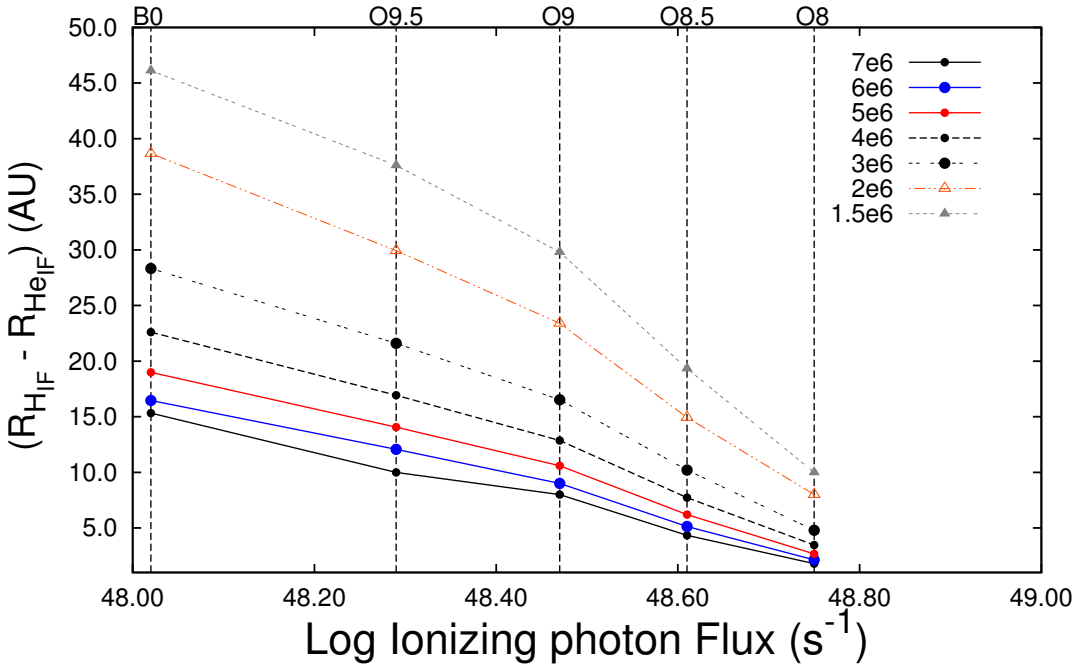

FIGURE 3.13: Here the distance between the H and He ionization fronts is given in AU for several densities and stellar types.

The distances between the helium ionization front and the hydrogen ionization front for stars B0 to O8 and densities 1.5 - 7.0 $\times 10^6$ cm^{-3} are shown in Figure 3.13. It shows how the distance between the H and He ionization front decreases as the stars become more massive. The difference in distance between the H and He ionization fronts ($R_{H_{IF}} - R_{He_{IF}}$, at 50 % of the density) also decrease with increasing density. This results in the optical depth between the H and He ionization fronts to decrease the more massive the star, because a fraction 0.66 of recombinations of helium to the ground state through either its singlet or triplet states results in photons above the hydrogen ionizing threshold of 13.6 eV. The optical depth as function of photon energy (13.6-24.4 eV) between the helium and hydrogen ionization fronts for four densities in the range between 1.5 - 7 $\times 10^6$ cm^{-3}, and stars ranging from B0 - O8 is shown in Figure 3.14. For a density of 7 $\times 10^6$ cm^{-3} in both Figure 3.13 and Figure 3.14, using a B0 star as reference, the optical depth for a O9.5 star is much lower. This is because the distance seems to be lower than the trend in the decrease of the distance (see the black line in Figure 3.13). The same applies for an O9 star: the distance seems to be above the trend and the optical depth is correspondingly higher, and for a O8.5 star the same happens as for a O9.5 star where the distance seems to be below the trend. From these results, it seems that it will be possible for the SEDs generated from the shocked gas of a CWB to influence the ionization front for stars at least as massive as O8 and densities at least as low as 1.5 $\times 10^6$ cm^{-3}. Even if the r^{-2} dilution decreases the flux of the ionizing photons from the shocked gas by a factor of ~ 20 relative to a B0 star and a density of 7.0 $\times 10^6$ cm^{-3}.

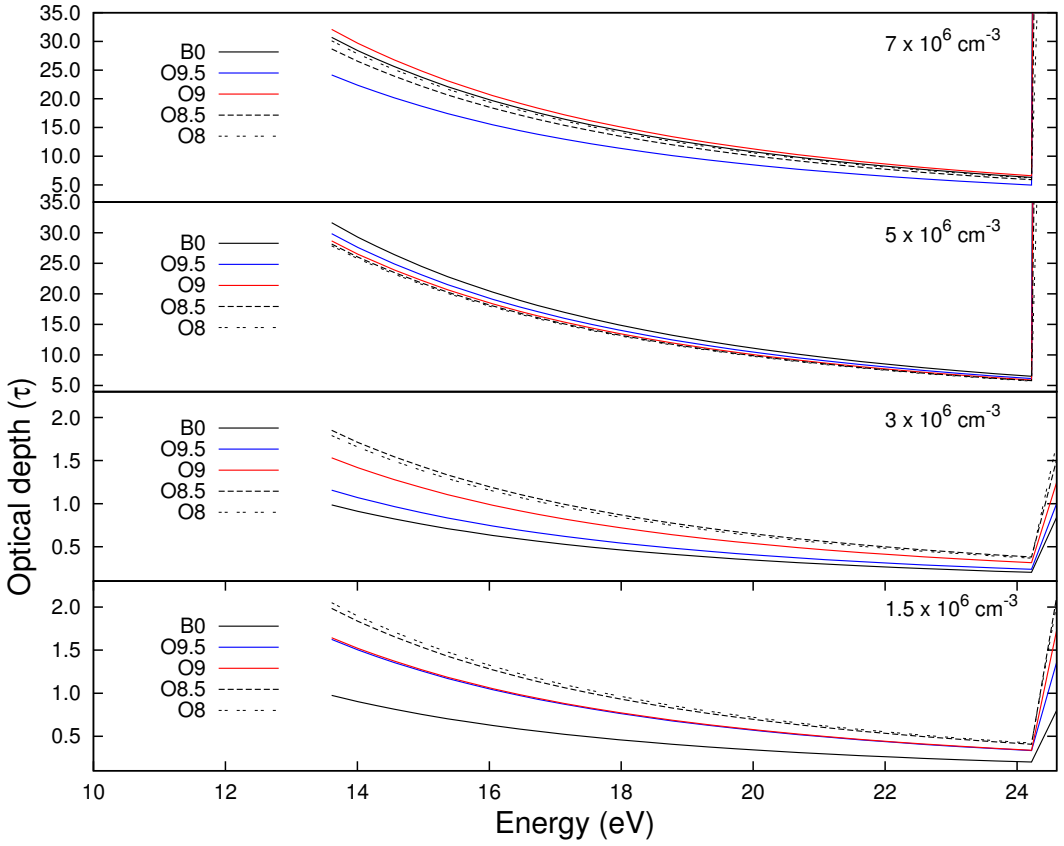

FIGURE 3.14: The optical depth as function of energy (13.6 - 24.6 ev) for four densities and five stellar types.

To summarize, the SEDs produced from the shocked gas are capable of causing additional ionization at the ionization front. The SEDs produced from adiabatically cooling gas, however, do not influence the ionization front very much. The reason is that the flux of low energy photons which is primarily responsible for the additional ionization is much lower than the lower energy flux for gas that is dominated by radiatively cooling, shown in the bottom left panel of Figure 3.7. The influence on the ionization front for a SED produced from adiabatically cooling gas may be maximized for different stellar parameters, as the stellar wind speed controls the temperature of the shocked gas and the luminosity depends on the stellar wind speed as $L_x \propto v_w^{-3}$. As described above, the influence on the ionization front from adiabatic cooling gas may also increase as a result of the decrease in optical depth with density and stellar type as shown for the example SED for radiative cooling conditions. It should be noted that changing the stellar type can change the mass-loss rate and stellar wind speed and thus the generated SED. The ionization front is considerably influenced ($\geq 10^{12}$ cm) by the additional ionizing photons from the shocked gas for radiative cooling conditions, thus there is enough energy generated in the shocked gas to cause changes in the position of the ionization front. This influence is dependent on the density and stellar type used, as shown above. The influence on the ionization front is controlled by the optical depth of the HII region, the optical depth between the helium and

hydrogen ionization fronts, and the r^{-2} dilution of the ionizing flux. Putting all of this together, the ionizing flux produced from the shocked gas can influence the ionization front for stars up to at least a O8 star and densities at least as low as 1.5 $\times 10^6$ cm^{-3}. The reason for this lower limit to the chosen density will be made clear in Chapter 4.

3.6 Free-free emission

3.6.1 Optical depth

As stated at the beginning of this thesis, the goal of this work is to investigate, from a theoretical point, whether the CWB hypothesis is realistic or not. It was also pointed out that in order for the CWB model to be a workable idea, it is necessary to show that the ionizing flux from the shocked gas can effect changes in the electron density at the ionization front, which is large enough to result in changes in the free-free emission from that region that can explain the relative amplitudes of the flaring masers. It therefore follows that it is necessary to calculate the free-free emission "emerging" from the HII region. In fact, in a very strict sense it is necessary to calculate the free-free emission for all stellar separations for which the colliding-wind calculations were done, and that these results have to be compared with the observed maser flare profiles.

The calculations with *Cloudy* give the radially-dependent electron density only for the equilibrium (static) state of the HII region. They do not take any time-dependence, such as the recombination of the plasma, into account. It should therefore be clear that using the static radially-dependent electron density distributions for the different separations between the primary and the secondary to calculate the free-free emission will also not include time- dependent effects due to the recombination of the plasma at the ionization front. In fact, using the static radially-dependent electron density distributions will result in a symmetric change in the free-free emission around the time of periastron passage. Using the static solutions from *Cloudy* will therefore result in symmetric flare profiles for the masers, which certainly is not the case.

To model the time-dependence in the electron density at the ionization front as best as possible, a quasi-time-dependent ionization rate, $\Gamma_p(t)$, was constructed from the series of solutions from *Cloudy* (see e.g. Figure 3.10). As described earlier, it is necessary to know $\Gamma_p(t)$ in order to properly include the recombination of the plasma. However, $\Gamma_p(t)$ was calculated by averaging the ionization rate over the area covered by the maser spot, which includes not only the ionization front but also positions on the inside and outside of the ionization front. The effect of such averaging is to lose all information on the radial variation of the ionization rate. The implication is that the time-dependent electron density that follows from solving Equation 2.66 also is an average and therefore does not contain any detail of the changes in the radial electron density

distribution. To calculate the time-dependent free-free emission requires knowledge of how the radial electron density changes with time. The averaging process, however, does not allow us to have such information.

With the approach followed in this work, one is therefore confronted with a two-fold dilemma: firstly, the static solutions from *Cloudy* give the detailed radial electron distribution necessary to calculate the free-free emission but do not contain any time-dependent information. Secondly, using an average ionization rate allows us to calculate a time-dependent average electron density but does not allow us to calculate the free-free emission. As a "solution" to this dilemma it is noted that the fitting of the recombination curve (Equation 2.66) to the decay part of the flares in G9.62 very strongly suggests that the HII region is optically thin at 12.2 GHz between the observer and the region where the electron density increased due to a pulse of ionizing radiation. What is then required is to investigate, within the framework of the static solutions of the electron density as obtained from *Cloudy*, whether the HII region is indeed optically thin at 12.2 GHz between the observer and the ionization front for both the quiescent state and when the effect of the SED of the shocked gas is included. Should it be the case that the HII region is optically thin, can it be concluded that it is safe to use $n_e^2(t)$ as a measure of the time-dependent free-free emission emerging from the HII region, where n_e is the time-dependent solution from Equation 2.62.

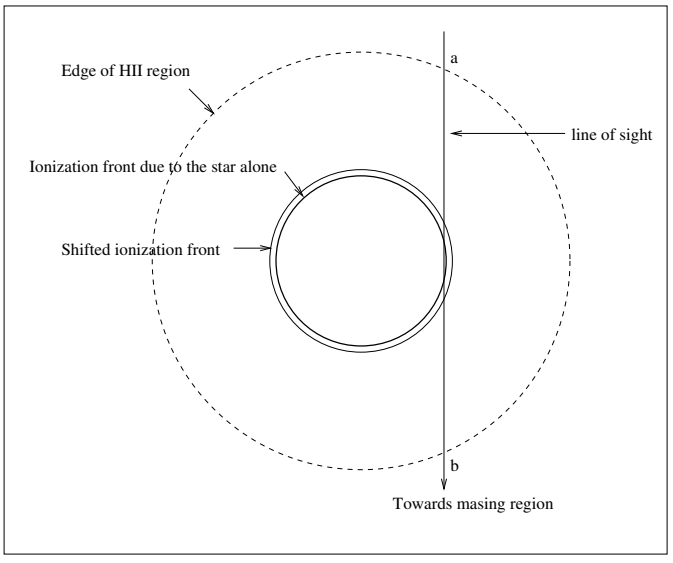

FIGURE 3.15: A schematic representation of the line of sight through the HII region almost at the tangent point of the sphere representing the ionization front. The inner solid sphere representing the ionization front due to the star alone, the outer solid sphere shifted by the additional ionizing radiation, and the outer dashed sphere representing the edge of the HII region.

To investigate to what extent the HII region is optically thin at 12.2 GHz, the geometry as shown in Figure 3.15 is used. The HII region is considered to be spherical and the line of sight almost at the position of a tangent to the sphere. For practical reasons the edge of the HII region was

set at an electron density of 10^4 cm^{-3}. In Figures 3.16 and 3.17 we show the electron density as a function of position along the line of sight, starting at point a and ending at b in Figure 3.15. In each panel is the case for a position of the ionization front in the quiescent state of the maser

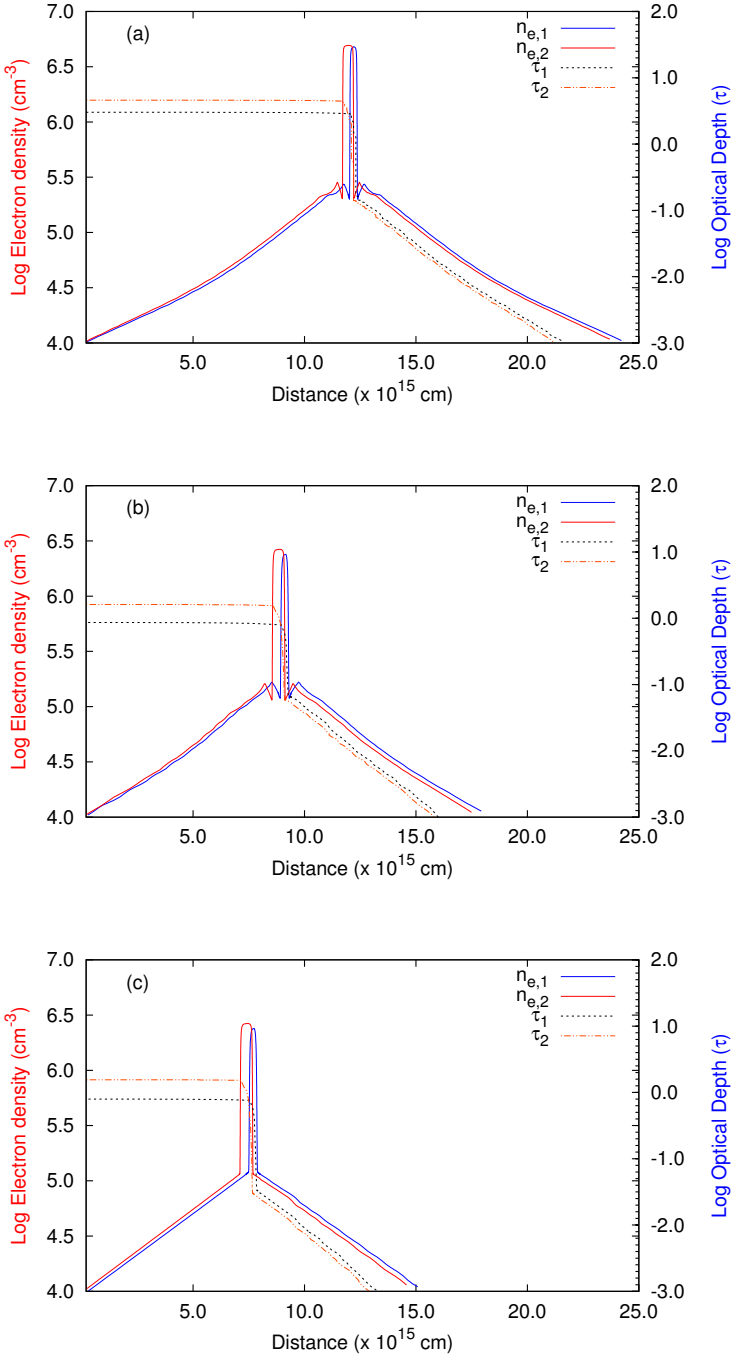

FIGURE 3.16: The electron density as function of distance along the line of sight without ($n_{e,1}$) and with ($n_{e,2}$) there being the extra ionizing photons from the shocked gas for the three density structures discussed. Also shown are the corresponding optical depths τ_1 and τ_2 along a line of sight from a to b, with the line of sight almost tangent to the sphere as shown in Figure 3.15.

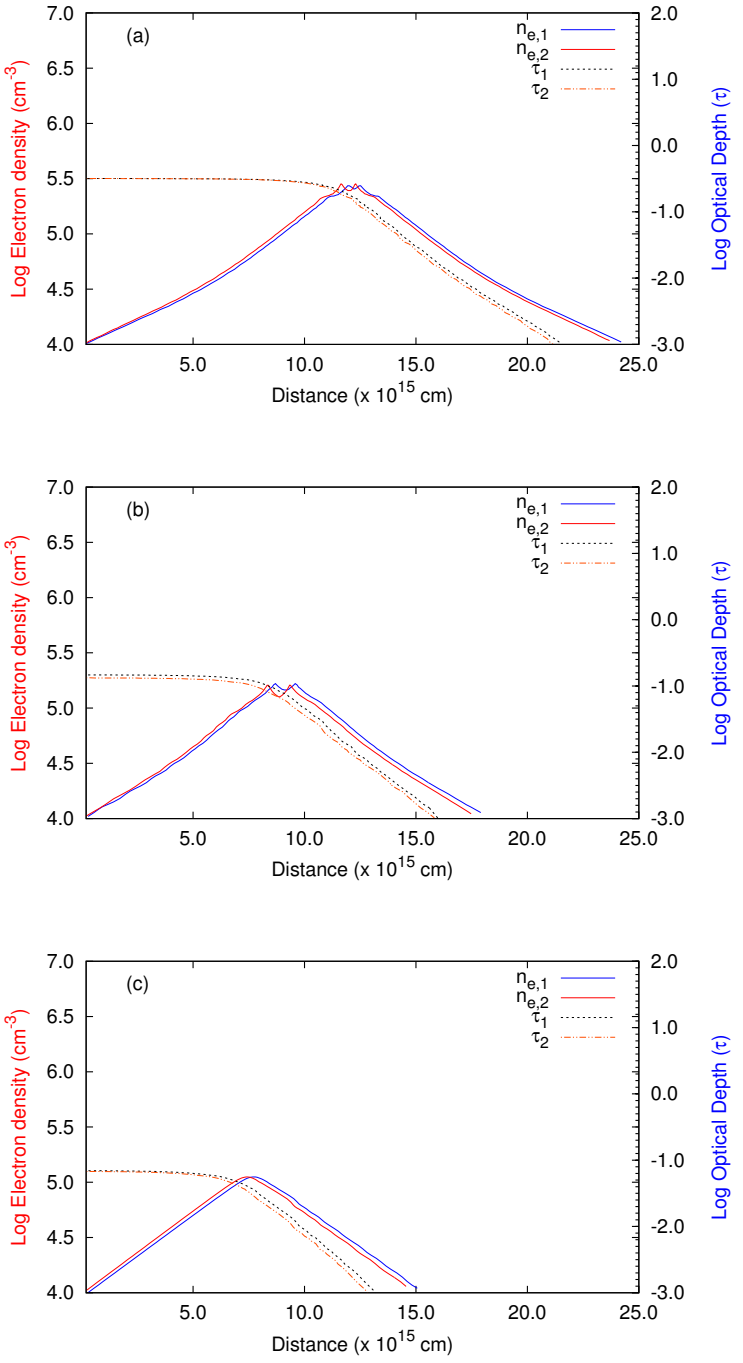

FIGURE 3.17: The same as Figure 3.16, but for a line of sight further away from the tangent point outside of the ionization front through the partially ionized gas.

as well as the case where the ionization front has been shifted due to the additional ionizing radiation from the shocked gas are shown. For both cases the electron density is seen to slowly rise as the ionization front is approached, reaching a maximum at the ionization front and then decreases again.

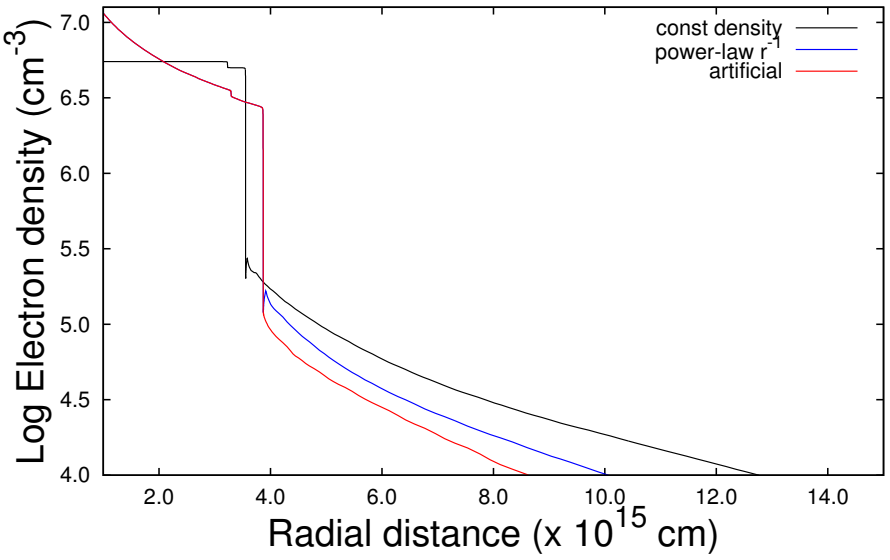

FIGURE 3.18: The radially-dependent electron density structure for a constant density (the black line) cloud, a radially-dependent power-law density (blue line) and the arbitrary structure (red line).

The optical depth at 12.2 GHz from any point on the line of sight to point b (again considering only points between a and b) is also shown in Figures 3.16 and 3.17. The dashed line represents the optical depth (τ_1) from any point on the line of sight to b for the case where the ionization front is in its quiescent state as well as the optical depth (τ_2) for the case where the ionization has been shifted due to the additional ionizing radiation from the shocked gas (dashed-dotted line). Panels (a) in Figure 3.16 and 3.17 show results for a constant neutral hydrogen density, (b) for a radially-dependent power-law density with index -1, and (c) an artificial ionization structure adapted from the radially-dependent power-law density structure. The radially-dependent electron density structures for these three considerations are shown in Figure 3.18. As described in Chapter 2, the maser spot is divided into slices of equal width. Panels (a)-(c) in Figure 3.16 show the position-dependent electron density along the line of sight from point a to b close to the tangent point of the inner solid sphere in Figure 3.15, where the line sight passes through the ionization front, and panels (a)-(c) in Figure 3.17 show the position-dependent electron density along a line of sight from a to b to the outside of the maser spot, away from the tangent point where the line of sight does not pass through the ionization front.

First, for panels (a)-(c) in Figure 3.16 it can be seen that the ionization front is seemingly optically thick ($\tau \geq 1$) at 12.2 GHz from point a to point b, such that the change in the free-free emission should be coming from the ionization front itself. Second, all these panels show that $\tau < 1$ along the lines of sight from the ionization front to point b. This indicates that the HII region from the ionization front to point b is optically thin at 12.2 GHz. Furthermore, from panels

(a)-(c) in Figure 3.17 (which is for the line of sight to the outside of the ionization front) the partially ionized gas outside of the ionization front is also optically thin at 12.2 GHz. However, note that the density is approximately an order of magnitude less than for a line of sight passing through the ionization front, and for practical purposes does not contribute to the averaged free-free emission very much. This strongly suggests that it is safe to use the time-dependent solution of n_e to represent the time-dependent free-free emission.

For this reason, the next section will firstly show the quasi-time-dependent ionization rates obtained from the equilibrium configurations of *Cloudy* for several parameter sets. Secondly, from these quasi-time-dependent ionization rates, the time-dependent solutions of n_e were acquired and the time-dependence of n_e^2 (the CWB model) will be shown and described.

3.6.2 Time-dependence of n_e

It was shown above that the HII region is optically thin from the ionization front towards the maser for radio free-free emission at 12.2 GHz. From the abovementioned discussion we can use the equilibrium states of *Cloudy* to solve for n_e time-dependently. In order to solve n_e time-dependently, the average electron density is obtained over the maser spot as described in Chapter 2. The average was determined from the equilibrium states of the ionization front for an entire orbit. Each of these average electron densities represents a phase in the orbit of the binary system. The phase is obtained by converting the equilibrium states (which were calculated for discrete separation distances) to time-dependent states. From these phase-dependent average electron densities, the quasi-time-dependent ionization rate can be calculated from Equation 2.63, given by

$$\Gamma_p(t) = \frac{n_e^2 \beta_2}{n_{H^0}}. \tag{3.3}$$

A cubic interpolation scheme was then used to construct the time-dependent ionization rate $\Gamma_p(t)$, and used in Equation 2.62 to solve for n_e time-dependently. As it was stated that the equilibrium solutions only give radially-dependent information but not time-dependent information, this time-dependent ionization rate is simply the initial condition to solve for the time-dependence of the electron density. Note that we use a period of 200 days for the binary orbit to show the behaviour of these solutions.

There are three parameters that control the time-dependent ionization rate (as constructed from the above description), namely, (1) the periastron distance used (which influences the binary orbit), (2) the neutral hydrogen density (see the explicit dependence in Equation 3.3), and (3) the position where the maser spot is projected on the ionization front. Several time-dependent ionization rates are shown in Figure 3.19, where periastron is set at 100 days. To show the effect

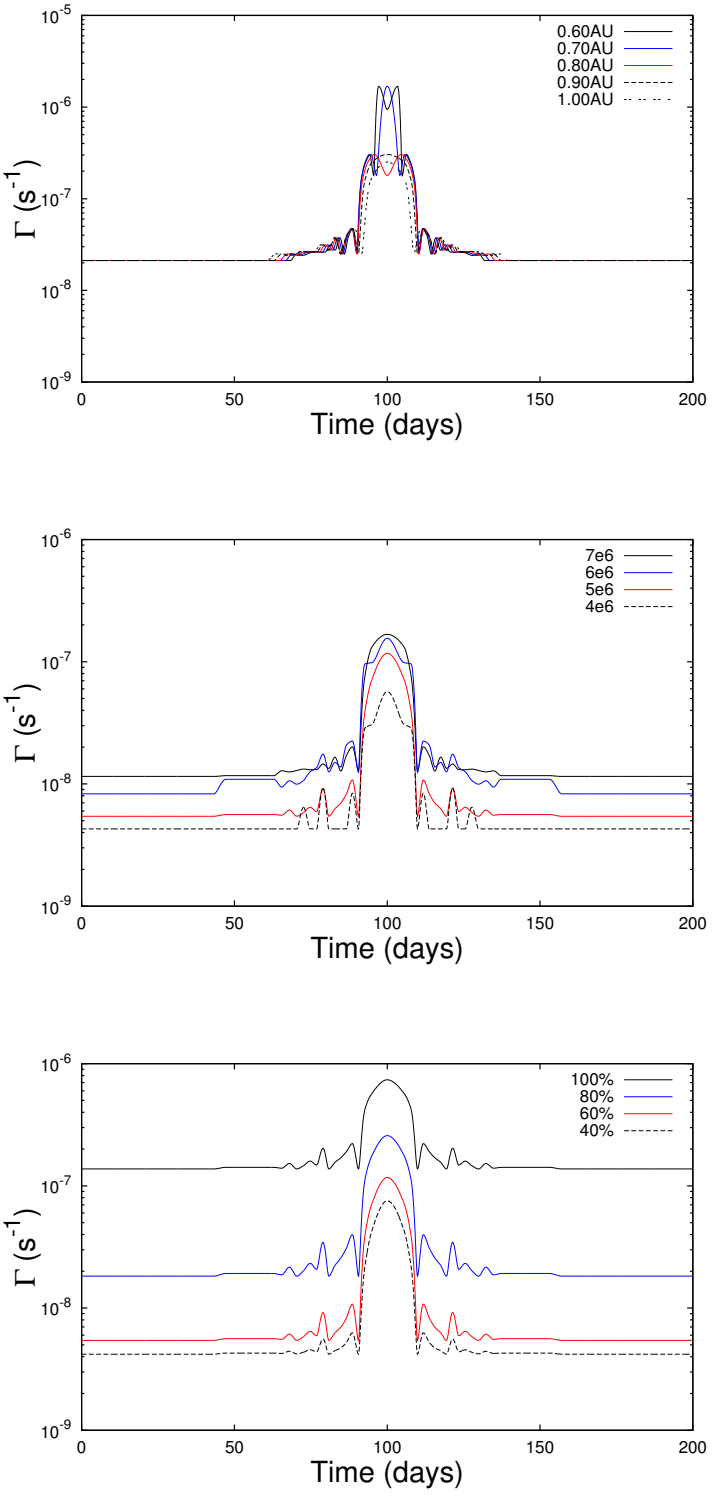

FIGURE 3.19: Top panel: the time-dependent ionization rates as function of time for various periastron distances. Middle panel: keeping the periastron distance the same and changing the neutral hydrogen density. Bottom panel: keeping both the periastron distance and the neutral hydrogen density the same and changing the projection of the maser on the ionization front.

of (1), the time-dependent ionization rate for several periastron distances for a neutral hydrogen density of 7×10^6 cm^{-3} is shown in the top panel. The different lines represent periastron distances of 0.6-1.0 AU with an interval of 0.1 AU. As can be seen, the time-dependent ionization rate is not "smooth". It was mentioned that with the averaging process we lose the structure of the ionization front, so that we do not know how it changes time-dependently. However, although this is a very simplified approach, it still provides an approximate description of the time-dependence of the ionization front. Note that the shocked gas behaves at least partly in a radiative manner for these periastron distances, and could also result in such variations. Furthermore, the time-dependent ionization rate only increases close to periastron, which is evident from the results obtained from Section 3.5.2, where it is only for separation distances close to periastron that the ionization front is considerably influenced.

In the middle panel of Figure 3.19, the effect of the neutral hydrogen density (2) on the time-dependent ionization rate is shown. These time-dependent ionization rates were obtained for a fixed periastron distance of 0.9 AU. From Equation 3.3, it can be seen that the time-dependent ionization rate will decrease when the neutral hydrogen density is decreased. Note that, from Figure 3.11 in Section 3.5.2, the influence on the ionization front for different neutral densities changes such that the time-dependent ionization rate also changes. For both (1) and (2), the time-dependent ionization rates were obtained where the position of the inner edge of the maser spot was projected such that the electron density is 60 % of the total neutral hydrogen density. However, as we do not know where exactly the maser spot is projected, the maser spot is

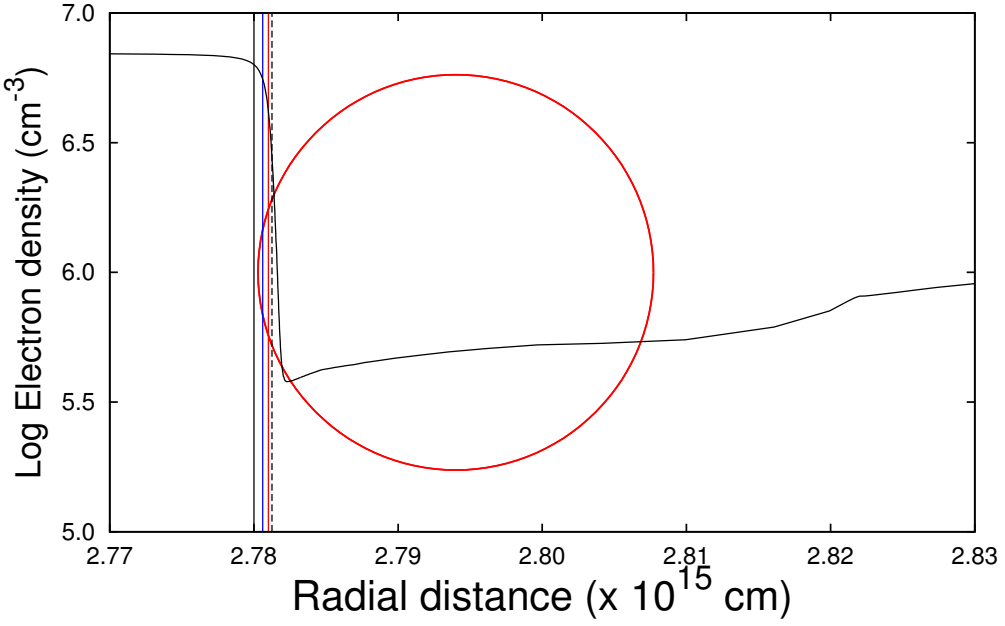

FIGURE 3.20: The projection of the maser spot on the ionization front. The vertical lines represent the projections of the maser spot, such that the electron density at the inner edge is at 90% (black line), 80% (blue line), 60%(red line), and 40% (dashed line) of the hydrogen density.

projected at several positions, to see what influence the position of the maser spot (3) will have on the time-dependent ionization rate. The maser spot was projected such that the electron density at the inner edge of the maser spot is 90 %, 80 %, 60 %, and 40 % of the maximum electron density due to hydrogen (hereafter the maximum electron density). This is shown in the bottom panel of Figure 3.19, where it shows that the time-dependent ionization rate decreases from the maximum (90 %) projection to the minimum (40 %) projection. This was also done for a periastron distance of 0.9 AU. The four positions where the maser spot was projected on the ionization front are shown in Figure 3.20, where the black vertical line represents the radial distance (from the central star) where the maser spot is projected at 90 % of the density. The other three vertical lines represent 80 % (blue line), 60 % (red line), and 40 % (the black dashed line). Now that we have shown how the time-dependent ionization rate behaves, let us see how the time-dependent solutions of n_e behave.

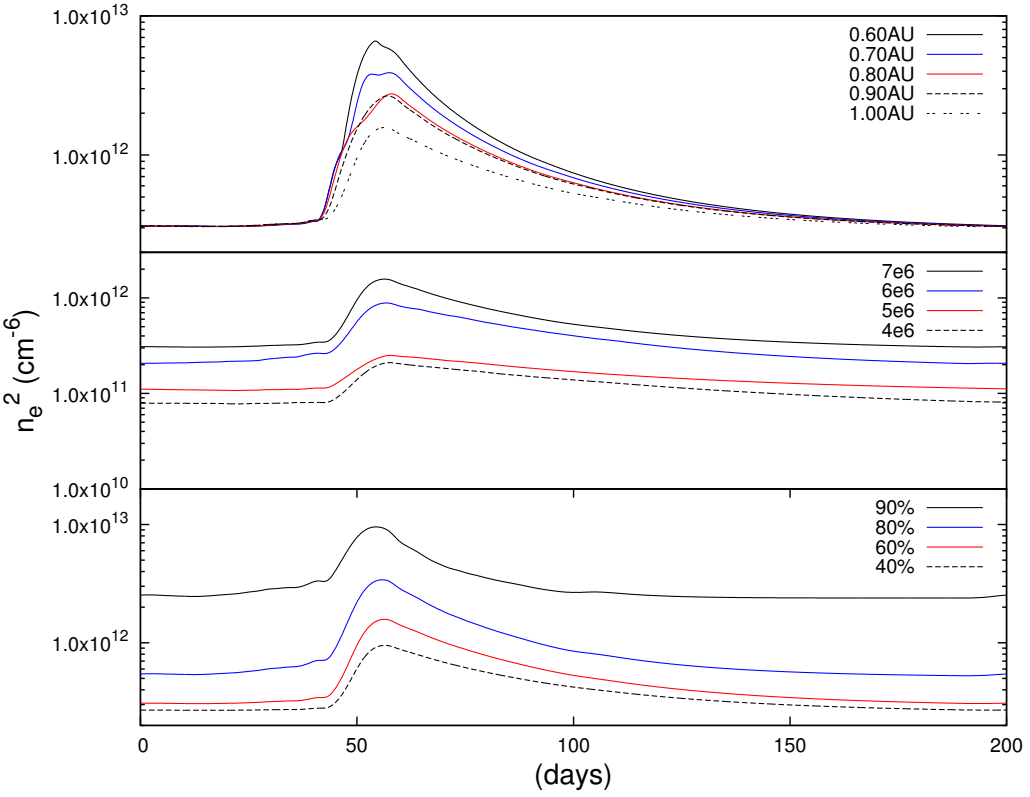

FIGURE 3.21: Time-dependent behaviour of n_e^2. Top panel: for several periastron distances. Middle panel: for different neutral hydrogen densities. Bottom panel: for four different projections of the maser spot on the ionization front.

From the time-dependent ionization rates obtained for different periastron distances, hydrogen densities, and four different maser spot projections the time-dependences of n_e^2 are shown in Figure 3.21. In the top panel, the same maser spot projection and the same neutral hydrogen density were used for five different periastron distances. This results in solutions for which the minimum (quiescent) electron densities are the same. As the influence on the ionization front is

the largest for a periastron distance of 0.6 AU, the electron density reaches the highest value for this periastron distance. The recombination time for the decay part of the profile is dependent on the maximum and minimum electron densities (see Equation 2.66), thus for the same quiescent electron density the recombination time for the highest maximum electron density will be the longest. This is seen in the top panel of Figure 3.21.

The middle panel of Figure 3.21 shows the time-dependence of n_e^2 for a periastron distance of 1.0 AU, with a maser spot projection at 60 % of the density, for four different neutral hydrogen densities. The black line in the middle panel is the same as the double dashed line in the top panel. The middle panel shows that as the neutral hydrogen density decreases, the time-dependence of n_e^2 decreases. This is simply because, for the same projection of the maser spot for different hydrogen densities, the electron density decreases as the neutral hydrogen density decreases. An important result from the the middle panel is that the lower the quiescent electron density, the longer the recombination time becomes, which can be shown from Equation 2.66. This has an important implication for the sources we investigate in this work. For these sources, with periods of $\simeq$ 179 days, $\simeq$ 196 days, $\simeq$ 237 days, and $\simeq$ 244 days, there should be a minimum quiescent electron density to which the quiescent states of each flare can recombine to. The reason for this is that, below a certain minimum electron density, the electron density will still be decreasing by the time the next flare starts. For all four sources investigated here a quiescent state is reached before the next flare starts, thus we expect a relatively high minimum electron density for the quiescent states of the flares. For example, the dashed line in the middle panel of Figure 3.21 shows a recombination time close to 200 days, and the minimum electron density to which the time-dependent n_e recombines to is $\simeq 3 \times 10^5$ cm^{-3}. This indicates that the minimum electron density associated with the quiescent state of all the sources investigated here should be larger than 10^5 cm^{-3}.

Furthermore, the bottom panel of Figure 3.21 shows how the quiescent electron density decreases as the projection of the maser spot is changed from 90 % to 40 % of the density. It shows that the recombination time increases as the electron density decreases. Additionally, the bottom panel of Figure 3.21 also shows that the recombination time to a high quiescent electron density is short (the black line) and it stays in the quiescent state longer, and as the quiescent electron density decreases, the recombination time increases.

We have described how the decay part of the flare profile will behave for different parameter sets, however, the relative amplitude of the flares also needs to be taken into account. The relative amplitude is defined as

$$R = \frac{F_{max} - F_{min}}{F_{min}} = \frac{n_{e,max}^2 - n_{e,min}^2}{n_{e,min}^2}. \tag{3.4}$$

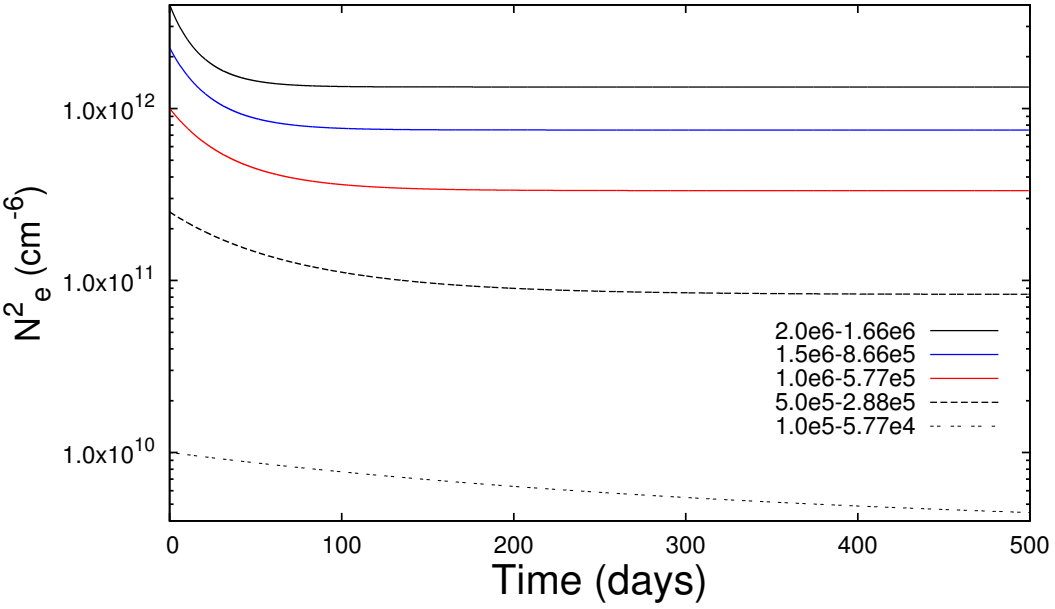

FIGURE 3.22: Time-dependent behaviour of n_e^2 from Equation 2.62. Five recombination curves with a constant relative amplitude of 2 for different maximum and minimum electron densities.

To describe the recombination where taking into account the relative amplitude, Figure 3.22 shows five recombination curves with a relative amplitude of 2 (obtained from one of the flares of the source G9.62+0.20E). The legends shows the peak and quiescent electron densities associated with each recombination curve. It shows that for high electron densities (with associated high quiescent electron densities), the recombination time is short and the quiescent electron density is quickly reached, with a recombination time shorter than the periods of the sources investigated here. It also shows that the lower the maximum electron density from where recombination commences, the longer the recombination time becomes and that for a certain value does not reach a quiescent state before the next flare starts again. From these results, (although the relative amplitudes of the flares are not constant) it is expected that the minimum electron density associated with the quiescent states of all of the sources investigated should be above 3 $\times$ 10^5 cm^{-3}.

3.7 Summary

From the hydrodynamical simulations, the shocked gas cools adiabatically for the largest part of the eccentric orbits, given the stellar and orbital parameters used. Only close to periastron is the shocked gas dominated by radiative cooling. The luminosity of the shocked gas cooling adiabatically follows the relation $L \propto D^{-1}$, whereas the luminosity from the shocked gas dominated by radiative cooling increases rapidly above the relation for adiabatic cooling gas. The

SEDs produced from the adiabatically cooling gas are seemingly identical, the only difference being the flux, where the flux increases/decreases if either the separation distance of the stars change or the mass-loss rate combination. For shocked gas dominated by radiative cooling on the other hand, the SED produced changes significantly, the main change being an increase in the flux at lower energies because the gas cools to lower temperatures.

For the adiabatic cooling gas, the SEDs produced do not influence the position of the ionization front very much, whereas the SEDs produced from gas dominated by radiative cooling influences the ionization front substantially with distance greater than 10^{12} cm. This were the results for a constant density of 7×10^6 cm^{-3}. These distances were also found to increase as the neutral hydrogen density is decreased. The reason is because the optical depth through the HII region decreases as the density decreases. It was also found that for stars earlier than a B0, the distance with which the ionization front is influenced increases. The reason here is that the optical depth for photons between the helium and hydrogen ionization front decreases, because the distance between these ionization fronts decreases, the earlier the stellar type. The geometrical dilution also contribute to the influence on the ionization front, and it is expected that at some distance the influence on the ionization front will start to decrease due to the geometrical dilution.

In order to justify the use of the time-dependent solution of n_e to represent the time-dependent free-free emission, it was shown that the HII region is optically thin from the ionization front towards the maser along the line of sight. It was also shown that for lines of sight passing through the ionization front, the ionization front is optically thick for the radio free-free emission propagating from the far-side of the ionization front towards the maser. This means that the maser only "sees" the free-free emission from the ionization front itself. From this result, the time-dependent ionization rate was constructed and used to solve for n_e time-dependently, and the behaviour of $n_e(t)$ was described for various system parameters. From the behaviour it was possible to determine, that the minimum electron density to which the flares of these sources recombine to (given their periods) should be higher than 3×10^5 cm^{-3}.

Chapter 4

The periodic sources

4.1 Introduction

As mentioned in Chapter 1, the decay part of the flare profile associated with the 12.2 GHz maser features in G9.62+0.20E (Goedhart et al., 2003) is proposed to be attributed to the recombination of a partially ionized hydrogen gas (van der Walt et al., 2009, van der Walt, 2011). If the decay part of the maser flare is caused by the recombination of a partially ionized gas, the question is, what background source could cause this behaviour? Here we assume the background source to be a HII region maintained by a high-mass star but which is time dependently influenced by some additional source of ionizing photons. The additional source of ionizing photons is assumed to be a CWB system. Since the discovery of the periodicity of the methanol masers in the HMSFR G9.62+0.20E, fifteen other HMSFRs with associated methanol maser emission have been discovered to also exhibit periodic variability. However, only a few of these HMFSRs show methanol maser emission which have flare profiles similar to G9.62+0.20E. Table 4.1 lists these HMSFRs and the periods of the methanol masers. Figure 4.1 shows the time series of the methanol maser flare profiles of the HMSFRs which resemble the flare profile of G9.62+0.20E. Besides the 12.2 GHz masers in G9.62+0.20E (Goedhart et al., 2003, 2004), the CWB model will be applied to the 6.7 GHz masers in G22.357+0.066, the 6.7 GHz masers in G45.473+0.134 (Szymczak et al., 2011, 2015) and the 6.7 GHz methanol and 4.8 GHz formaldehyde masers in G37.55+0.20 (Araya et al., 2010). First, where possible, Equation 2.66 will be used to analyse the decay of each individual flare. For the HMSFRs where this is impossible due to inadequate data sampling of the flare profiles, ephemeris folding is applied and Equation 2.66 is then applied to the folded data. This analysis provides us with the best fit quiescent and peak electron densities for each flare. Second, the CWB model (time dependent solution of Equation 2.62) as described in Chapter 2 is compared with the different maser profiles.

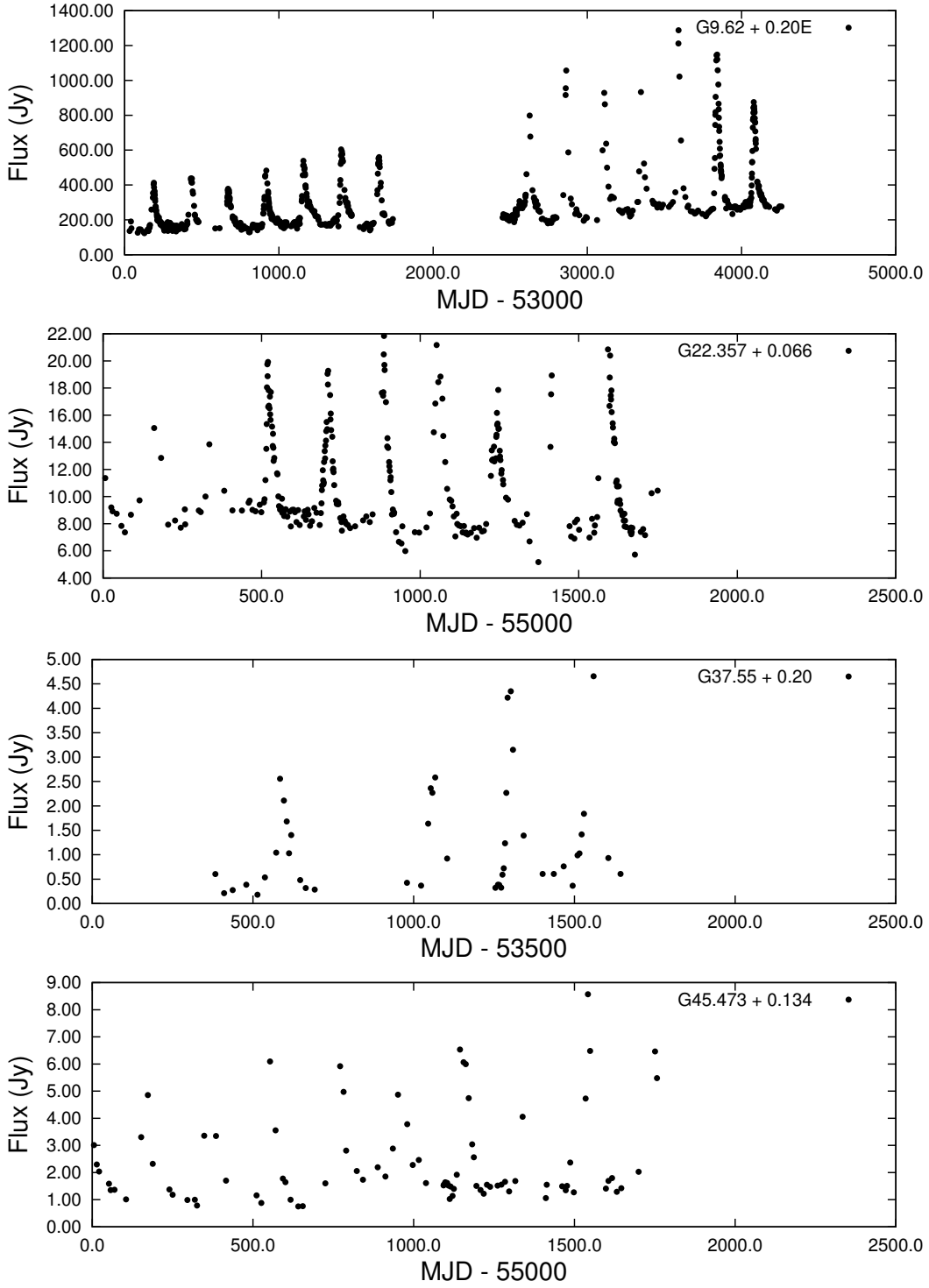

FIGURE 4.1: The time series of four periodic masers that show the same flare profile. The top panel show the flare profile of the 1.25 km s^{-1} feature of the 12.2 GHz methanol maser associated with the star forming region G9.62+0.20E. The second panel shows the 80.09 km s^{-1} feature of the 6.7 GHz methanol maser associated with the star forming region G22.357+0.066. The third panel shows the 79.5 km s^{-1} feature of the 6.7 GHz methanol maser associated with the star forming region G37.55+0.20, and the bottom panel the 59.60 km s^{-1} feature of the 6.7 GHz methanol maser associated with the star forming region G45.473+0.134.

4.2 About the periodic sources

4.2.1 G9.62+0.20E

The HMSFR G9.62+0.20 has been studied extensively in the past at radio and infrared wavelengths (see e.g. Garay et al., 1993, Kurtz et al., 1994, Hofner et al., 1994, 1996). Garay et al. (1993) did multi-frequency *Very Large Array* (VLA) radio continuum mapping at 1.5 GHz, 4.9 GHz and 15 GHz from which several individual peaks in the radio continuum were detected at this position, of which component E was one. Additionally, Kurtz et al. (1994) measured the 2 cm radio continuum emission and used the same nomenclature as Garay et al. (1993) to distinguish between the components. From the detections made for component E at 2 cm and 2.7 mm, Hofner et al. (1996) fitted a power-law to the spectrum with an index of 1.1 $\pm$ 0.3, and suggests that the origin of the spectrum is either a partially ionized stellar wind or a compact HII region with a radially dependent electron density with a spatial extent $\leq$ 2.5 mpc, and with excess dust emission with a temperature of $\simeq$ 100 K. Franco et al. (2000) also fitted a power-law to the spectrum with the additional 3.6 cm observations from Testi et al. (2000), and found a somewhat smaller gradient of 0.95 $\pm$ 0.06, however, still indicating the previously mentioned scenarios. Hofner et al. (1996) also found high molecular hydrogen densities $\simeq 10^7$ cm^{-3} associated with component E, and associated electron densities of the order of $\simeq 8 \times 10^5$ cm^{-3}. According to Hofner et al. (1996) the central stellar driving source is approximately of spectral type B0.

4.2.2 G22.357+0.066

This source was first reported as periodic by Szymczak et al. (2011) with a period of $\simeq$ 179 days, by applying ephemeris folding to the then available data of three flares. Recently Szymczak et al. (2015) reported on newly obtained observations and updated the time series. From Szymczak et al. (2011) the flaring occurs in several velocity features, of which we are going to use the 80.09 km s^{-1} feature for comparison with the CWB model, shown in Figure 4.1. No 5 GHz radio continuum has been detected for G22.357+0.066 (Szymczak et al., 2011), and according to its 3-colour composite IRAC image, Cyganowski et al. (2009) deemed it a *Massive Young Stellar Object* (MYSO) candidate. A recent study of outflows associated with sites of high-mass star formation was conducted by de Villiers et al. (2014) who found that G22.357+0.066 also has *high velocity* molecular outflows associated with it. Bartkiewicz et al. (2009) observed this source with the *European VLBI Network* (EVN) and concluded that the masers associated with it are distributed in a disk-like structure, which may indicate an accretion disk. From their Figure 4 and 5, which show the maser spot distribution and projection, the 80.09 km s^{-1} maser feature is projected at a distance of $\approx$ 200 - 400 AU from the central star. From the proposed evolutionary

sequence of HMSF given in Chapter 1, this source may still be in the HMC phase and an HCHII may be present. The HCHII region should thus be in an early stage of evolution and is expected to still be optically thick at 5 GHz. There is no information available for the stellar type.

4.2.3 G37.55+0.20

This source has been part of several studies at radio frequencies, millimeter molecular lines as well as molecular maser emission. Araya et al. (2004) observed it to be only the fourth 6 cm formaldehyde (H_2CO) maser to be discovered, due to H_2CO's tendency to be observed in absorption rather than emission. From Araya et al. (2004, 2005, and references therein), H_2CO changes from an absorber to an emitter at high densities ($N(H_2) \geq 10^5$ cm^{-3}). Beuther et al. (2002b) observed that this source has high density molecular gas with bipolar molecular outflows associated with it at 1.2 mm. It also has 22 GHz H_2O masers and 6.7 GHz methanol masers associated with it (see e.g. Beuther et al., 2002a). A disk-like structure is also proposed by Zhang et al. (2007), from their 4.5 μm dust emission survey. Araya et al. (2004) give its bolometric luminosity as $\simeq 6 \times 10^4$ L$_\odot$, which is assumed to be an O8 ZAMS star. This source is also known in the literature as *Infrared Astronomical Satellite* (IRAS) source 18566 + 0408.

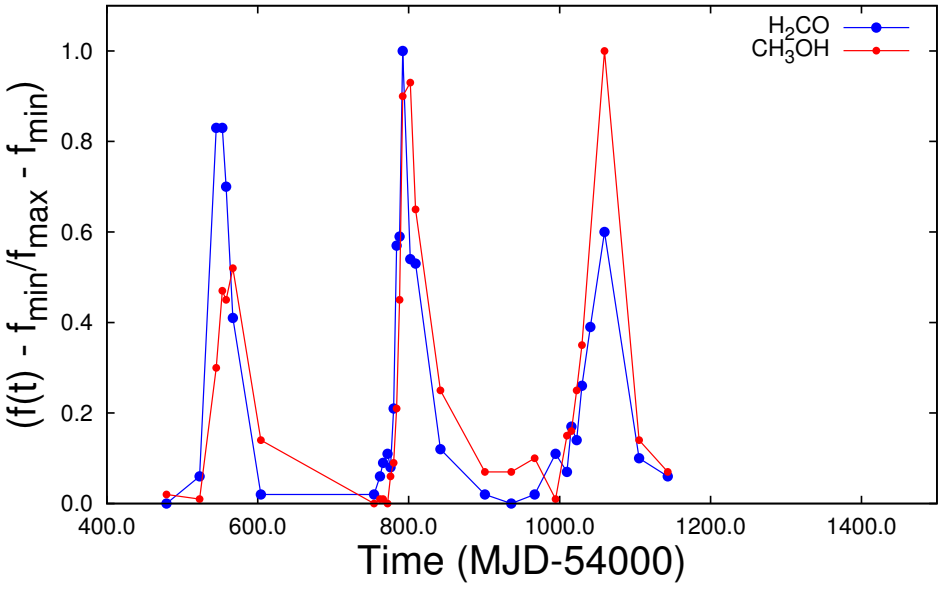

FIGURE 4.2: The normalized flare profiles of both the CH_3OH (red line) and H_2CO (blue line).

Radio emission was detected at 6 cm, 3.6 cm, 2 cm, 1.3 cm and 0.7 cm by Araya et al. (2005, 2007, and references therein), using the VLA. Araya et al. (2007) report that the radio free-free emission spectrum can be interpreted as a spherical HII region. However, they interpret it as ionized jets. All of these observations indicate an early phase of *High-Mass Star Formation*

(HMSF). Recently Araya et al. (2010) reported that G37.55+0.20 exhibits periodic variability of both its CH_3OH and H_2CO masers. The observations done by these authors show that the CH_3OH and H_2CO masers are separated by $\simeq$ 2000 AU, and they argue that the observed positions of the masers with respect to each other would make them difficult to interpret with the CWB model. The argument is based on the separation, which should result in time delays between the CH_3OH and H_2CO masers due to light travelling times. According to Araya et al. (2010) the central star is somewhere between the two masers, so it is possible that the masers are simply projected on opposite sides of the HII region equidistant from the central star. Figure 4.2 shows the normalized flare profiles of the two masers and they flare almost at the same time with every flare. The flare profiles of the two maser species show remarkable similarity. From the numerical calculations performed by van der Walt (2014) these two species are pumped by different mechanisms and it is unlikely that the changes are therefore due to variability in the pumping of the masers.

4.2.4 G45.473+0.134

This source was observed in the *Galactic Ring Survey* (GRS), the *Infrared Space Observatory* (ISO), IRAS and with the *Midcourse Space Experiment* (MSX). Testi et al. (1999) also observed it with their VLA longitude l=+45° field survey, and a 3.6 cm radio continuum was detected but no 6 cm continuum was detected. Testi et al. (1999) classify it as an extended source with an associated UCHII region according to the classification by Wood & Churchwell (1989). Kraemer et al. (2003) selected five star forming cores from the GRS of which G45.47 + 0.134 is one, and observed it at 12.5 and 20.6 μm. From a comparison between the radio continuum flux and the *Mid Infrared* (MIR) flux, Kraemer et al. (2003) inferred a stellar type of $\sim$ O6 from the model of Panagia (1973).

4.3 Flare analysis

We make the hypothesis that the flare profiles are described by increase and subsequent decrease of the electron density of a partially ionized gas. The decay part of the flare thus describes the recombination of the partially ionized gas to a lower state of ionization. After the pulse of ionizing radiation has passed, recombination will then commence and the partially ionized gas will return to its quiescent (the period between flares) level of ionization as set by the ionizing flux of the star. We fit Equation 2.66, given by

$$n_e^2(t) = n_{e,min}^2 \left(\frac{u_0 + \tanh(\alpha n_{e,min} t)}{1 + u_0 \tanh(\alpha n_{e,min} t)} \right)^2 , \tag{4.1}$$

to the decay of the flares to obtain estimates of the peak and quiescent electron densities associated with each flare. Each flare of the four sources shown in Figure 4.1 were analysed in this way by using Equation 4.1. If this is not possible (cf. scarce data sampling) ephemeris folding was used to fit the general form of the folded data. Additionally, we can obtain the relative amplitude from each flare profile, where the relative amplitude was defined by Goedhart et al. (2003) as

$$R = \frac{F_{max} - F_{min}}{F_{min}} = \frac{n^2_{e,max} - n^2_{e,min}}{n^2_{e,min}}, \tag{4.2}$$

where F_{max} and F_{min} are the maximum and minimum observed flux densities respectively, and for optically thin conditions the same holds for $n^2_{e,max}$ and $n^2_{e,min}$.

4.3.1 G9.62+0.20E

Figure 4.3 shows the fits of Equation 4.1 to four of the flares shown in the time series of G9.62+0.20E. The four flares are the 1st, 6th, 10th and 13th flares given in Table 4.1. It is seen that the recombination curve fits remarkably well to the observed decay of the maser flare profiles. The fitting of the recombination curve to the maser flare profiles was done for all available flares in the time span from MJD 53000 - MJD 57000.

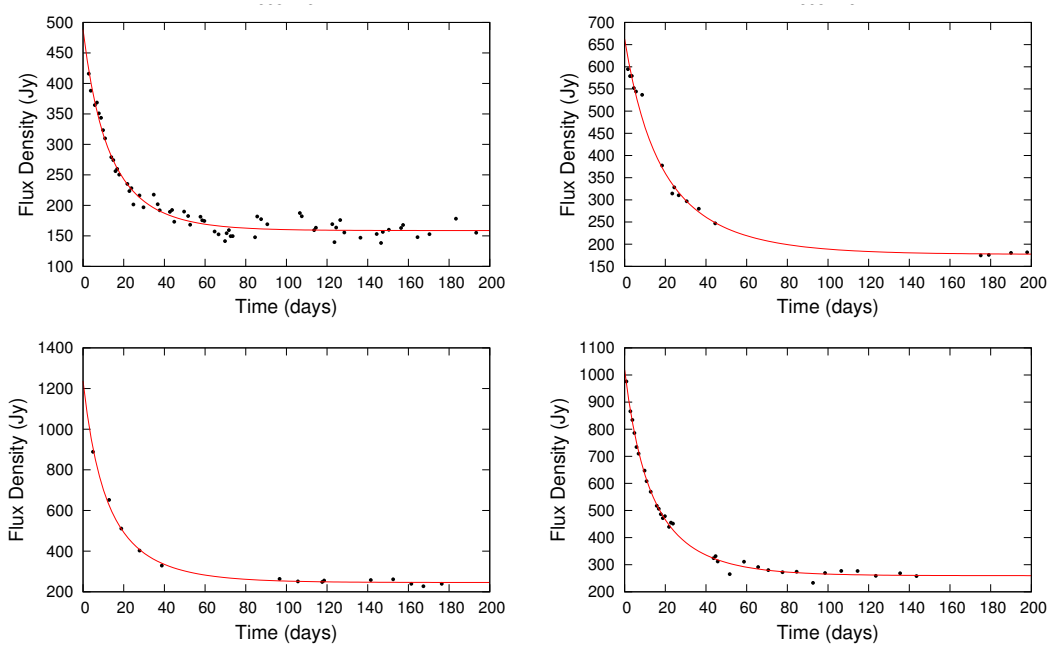

FIGURE 4.3: The panels show the fit of Equation 4.1 to four individual flares of the 12.2 GHz methanol maser 1.25 km s^{-1} velocity feature.

The values of $n^2_{e,min}$ and $n^2_{e,max}$ as obtained from each of these fits are plotted as function of time in the top panel of Figure 4.4, where the red points represent the $n^2_{e,min}$ and the black points the corresponding $n^2_{e,max}$ values. Note from the top panel that the $n^2_{e,min}$ values are plotted 200 days after the $n^2_{e,max}$ values, this is because the recombination fits were applied to the data over an period of 200 days as seen in Figure 4.3. Taken over all the flares, the electron density in the quiescent state of the maser lies in the range $\simeq$ 4-7 $\times$ 10^5 cm^{-3}, and the peak electron density between $\simeq$ 0.9 - 1.5 $\times$ 10^6 cm^{-3}. The individual values for each flare for both the quiescent and peak electron densities are summarized in Table 4.1 on page 96.

Closer inspection of the top panel of Figure 4.4 suggests that both $n^2_{e,min}$ and $n^2_{e,max}$ are increasing with time. We assume that the increase with time is linear, and the expressions for the best linear regression fits are

$$n^2_{e,min} = (3.30 \pm 2.54) \times 10^7 t + (1.78 \pm 0.47) \times 10^{11} \quad (4.3)$$

$$n^2_{e,max} = (2.52 \pm 1.22) \times 10^8 t + (5.44 \pm 1.96) \times 10^{11}, \quad (4.4)$$

where the units of t is days. Note that the n^2_e's are plotted on a logarithmic scale. From the expressions for $n^2_{e,min}$ and $n^2_{e,max}$, the gradients are positive within the errors. If we assume that the radio free-free emission is optically thin at 12.2 GHz between the ionization front of the HII region and the maser (discussed in Chapter 3), the quiescent flux density and $n^2_{e,min}$ can be compared.

Inspection of the top panel of Figure 4.1 shows that there is a steady rise with time in the quiescent state flux density. To quantify this rise, the flares were removed and a linear regression was applied to the quiescent state flux densities. This showed that the quiescent state flux density increased at a rate of 0.027 $\pm$ 0.001 Jy day^{-1}. The question that obviously follows is whether the increase in the quiescent state flux density is related to a possible increase in the quiescent state electron density of that part of the HII region against which the maser spot is projected. In this regard it has to be noted that in the optically thin case the free-free emission is proportional to n^2_e as was already discussed in Chapter 2. To compare the quiescent flux density with $n^2_{e,min}$, the quantity $n^2_{e,min}$ needs to be scaled to the observed quiescent state flux density. This was done at MJD 55000 shown by the "x" in the bottom panel of Figure 4.4, by determining the quiescent state flux density at "x" from the best fit to the quiescent state flux density, and then dividing the expression for $n^2_{e,min}$ by the scaling factor. This results in that the scaled $n^2_{e,min}$ value is equal to the quiescent flux density at that time, and leads to the gradient of $n^2_{e,min}$ to be in units of Jy day^{-1}. The gradient for $n^2_{e,min}$ is 0.026 $\pm$ 0.020 Jy day^{-1}, which is remarkably similar to the rate at which the quiescent flux density increases. The result of the

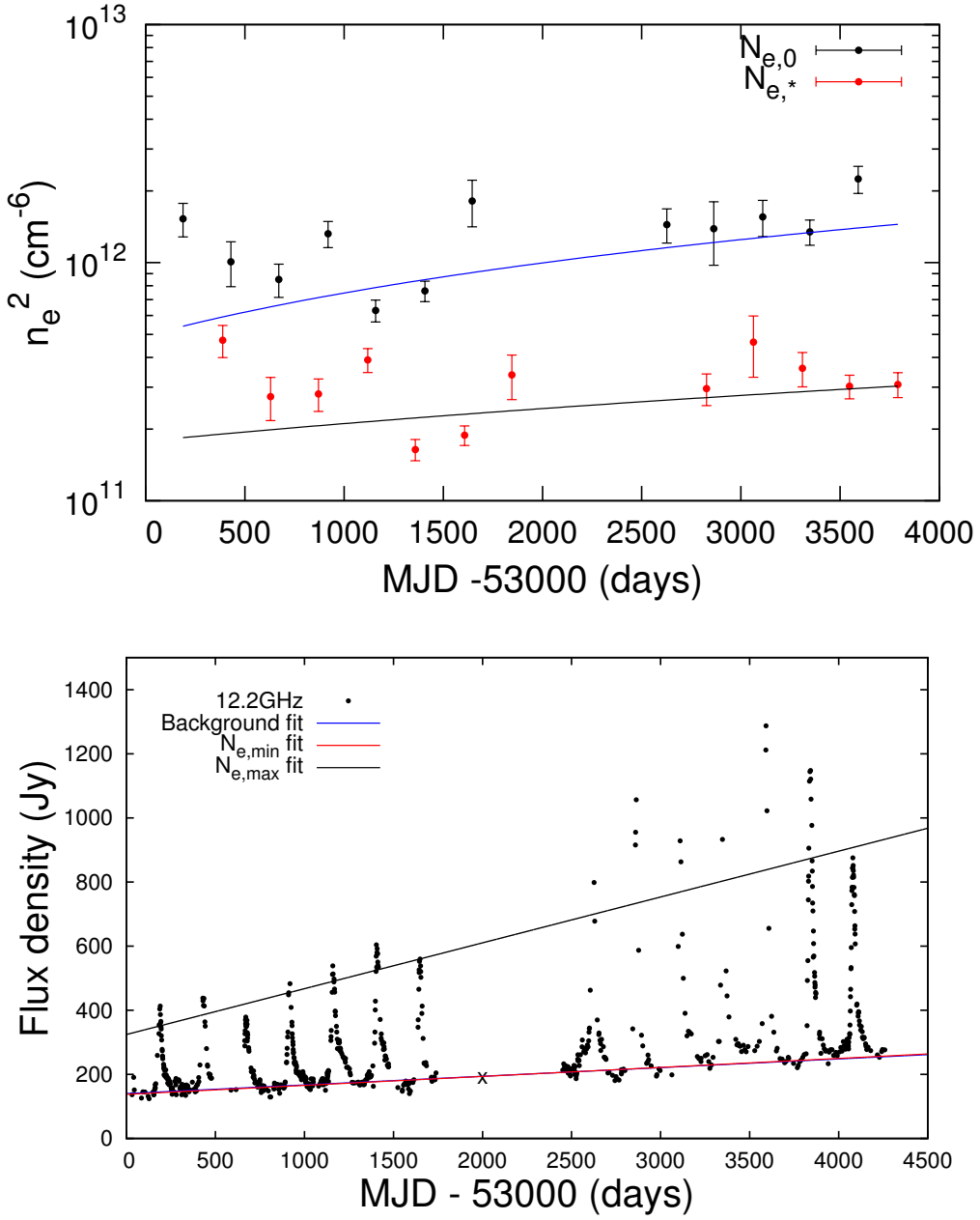

FIGURE 4.4: Top panel: here the quiescent and peak electron densities as function of time is shown as determined by the recombination fits shown in Figure 4.3. Bottom panel: the best linear regression fit (blue line) to the quiescent flux density of the maser overlaid with the normalized best linear regression fit to the time-dependent $n^2_{e,min}$ values (red line), as well as a normalized fit to the $n^2_{e,max}$ values with relative amplitude of $\simeq 2.2$ (black line). Note that the n_e^2's is on a logarithmic scale.

normalized time-dependent $n^2_{e,min}$ is shown by the red line in the bottom panel of Figure 4.4. As seen from Figure 4.4, the fit to the quiescent flux density (blue line) is practically identical to the fit of $n^2_{e,min}$ (red line). The implication of this result is that it seems as if the slow rise in the quiescent state flux density can be ascribed to a slow increase in the electron density in that part of the HII region against which the maser is projected. It also suggests that the part

of the HII region against which the maser is projected, is optically thin at 12.2 GHz.

The bottom panel of Figure 4.4 also shows a fit to the peak flux density. The fit is made on the premise that at MJD 55000 ("x") the relative amplitude (Goedhart et al., 2003, van der Walt, 2011) of the flare is ± 2.2. This fit also shows a remarkable resemblance to the increase in the peak flux density with time. Additionally, the relative amplitudes obtained from the observed flux densities (as defined above) range between 1.10-4.11, and the relative amplitudes from the fitted quiescent and peak electron densities range between 1.99-6.29. The relative amplitudes of the observed flux densities are given in Table 4.1, as well as those obtained from the fitted electron densities with their error margins given in brackets. However, two things have to be noted: (1) the relative amplitude values for the recombination fits do not take into account the errors associated with the fits, and (2) not all of the flares have well sampled data at the peak of the flare, thus there is a uncertainty as to where the peak of the flare is chosen. In spite of the uncertainty in the exact position of the peak of the flare, it is safe to conclude that the increasing trend in n_e^2 and the flux density as well as the range of relative amplitudes obtained from the recombination curve fits agree with that seen in the data.

The results from this analysis gives strong support for the maser being projected against a partially ionized background source changing its ionization state time-dependently. The analysis also indicate that the increase of the quiescent state flux density of the maser follows the same linear increase as derived for the quiescent electron density. This result strongly suggests that the partially ionized gas against which the maser is projected is optically thin at 12.2 GHz. The increase in the quiescent electron density as found from the analysis will be artificially incorporated into the CWB model, the reason for which will be explained in the next section.

4.3.2 G22.357+0.066

The results from the application of Equation 2.66 to four of the flares associated with G22.357+0.066 are shown in Figure 4.5. The four flares are the 1st, 2nd, 3rd and 6th flare in Table 4.1, and the respective electron densities for the individual flares are also given in Table 4.1. The recombination curve fits the observations well, but the uncertainty seems to be higher than for G9.62 + 0.20E. However, as in the case of G9.62+0.20E, these results still suggest the presence of a recombining partially ionized gas. The electron densities obtained from the recombination fits are between $\simeq$ 8.2-5.3 $\times$ 10^5 cm^{-3}, for the quiescent state electron density, whereas the peak electron density varies between $\simeq$ 1.28-0.91 $\times$ 10^6 cm^{-3}.

Following the analysis as for G9.62+0.20E, a linear regression fit was also applied to the quiescent flux density of the time series, and the gradient was found to be -0.0010 ± 0.0002 Jy day^{-1}. The decrease in the flux density for G22.357+0.066 from visual inspection is not as prominent as for the increase in G9.62+0.20E, but nonetheless there is a decrease. To compare the flux densities

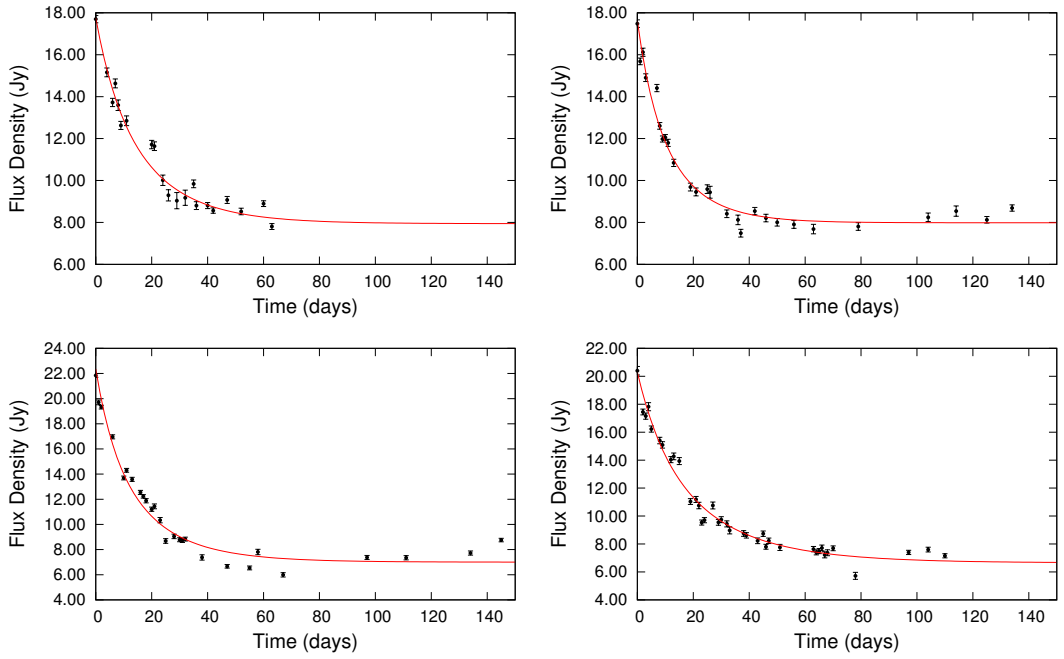

FIGURE 4.5: The panels show the fit of equation 2.66 to four individual flares of the 12.2 GHz methanol maser feature 80.09 km s^{-1}. Note that the n_e^2 is on a logarithmic scale.

with n_e^2, a linear regression was also applied to the $n_{e,min}^2$ and $n_{e,max}^2$ values of G22.357+0.066 exactly like for G9.62+0.20E, shown in the top panel of Figure 4.6. The expressions for the linear regression fits to the $n_{e,min}^2$ and $n_{e,max}^2$ values are given by

$$n_{e,min}^2 = (-3.18 \pm 0.67) \times 10^8 t + (7.67 \pm 0.83) \times 10^{11} \quad (4.5)$$

$$n_{e,max}^2 = (-6.59 \pm 1.80) \times 10^8 t + (1.82 \pm 0.29) \times 10^{12}. \quad (4.6)$$

Using the same approach to scale $n_{e,min}^2$ to the quiescent state flux density as done for G9.62+0.20E, $n_{e,min}^2$ is scaled to the quiescent state flux density at MJD 55600, where the blue and red lines intersect in the bottom panel of Figure 4.6. The gradient obtained for $n_{e,min}^2$ is -0.0030 $\pm$ 0.0015 Jy day^{-1}.

From the expression for the linear regression applied to $n_{e,min}^2$ for G22.357+0.066, it shows that the gradient is negative. The gradients of the quiescent state flux density and the quiescent values of $n_{e,min}^2$ are not the same. However, as mentioned there is a larger uncertainty for the fits to the flares of G22.357+0.066, this may be the cause of the discrepancy. Although the gradients of $n_{e,min}^2$ and the quiescent state flux density are found not to be exactly the same, it should be noted that the smallest gradient of $n_{e,min}^2$ if the errors is taken into account lies just outside the gradient of the quiescent state flux density. The gradient of the linear regression to

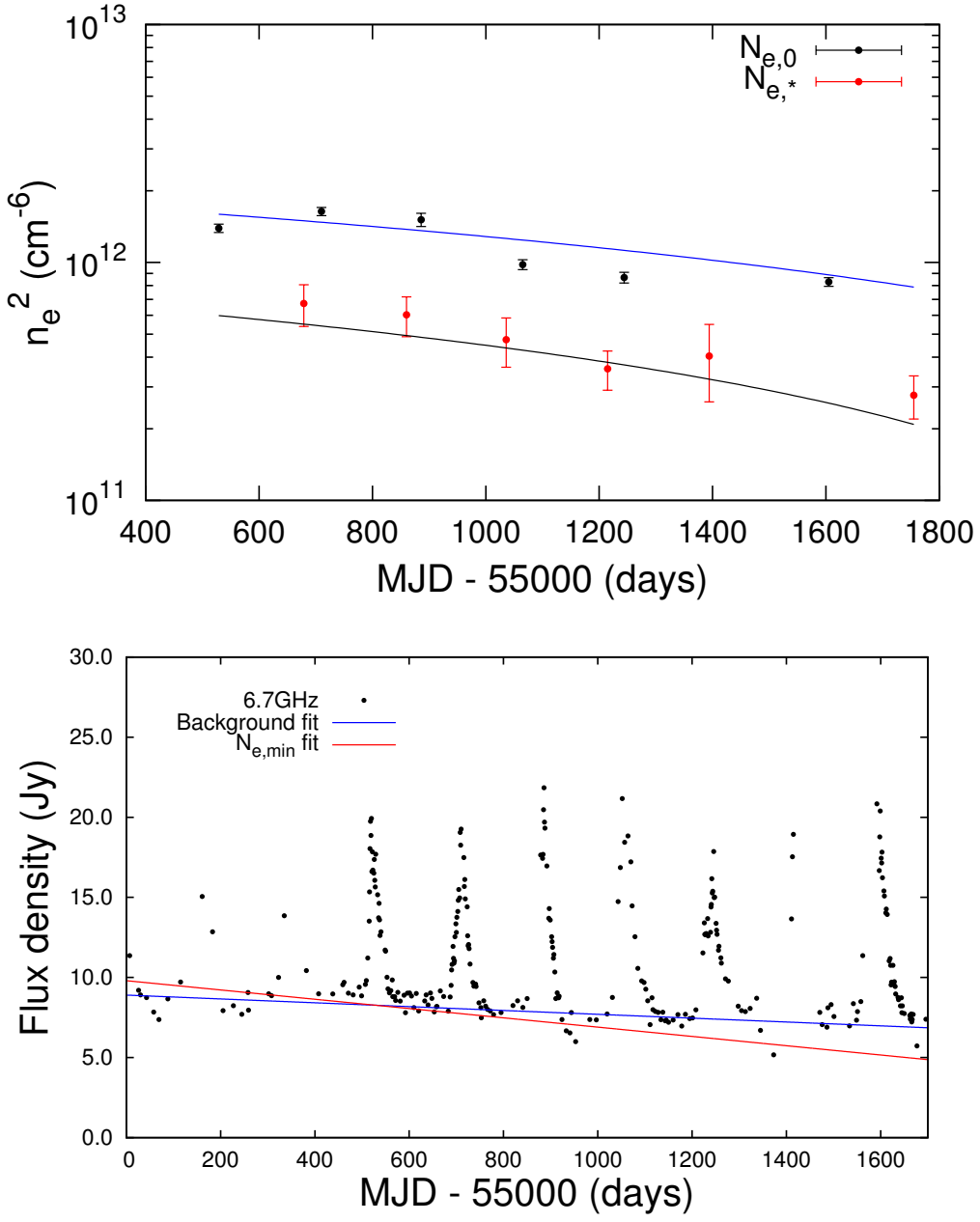

FIGURE 4.6: The fitted gradient of the regression fit to the quiescent flux density of the time series (blue line), as well as the fitted gradient of the $n^2_{e,min}$ quiescent values. Note that the n_e^2's is on a logarithmic scale.

the quiescent flux density is shown by the blue line in Figure 4.6, and the normalized fit of $n^2_{e,min}$ is shown by the red line. Although the gradients of the quiescent flux density and n_e^2 are not the same, the decay of the flares still suggests the presence of a recombining partially ionized gas. As for G9.62+0.20E, the relative amplitudes determined from the observed flux density range from 1.0 - 1.7, whereas the relative amplitudes obtained from the $n^2_{e,min}$ and $n^2_{e,max}$ values range from 1.1 - 2.0. These values compare well and are the same within the error margins.

4.3.3 G37.55+0.20

Unfortunately the time series of both the CH_3OH and H_2CO masers is very poorly sampled for this source, making it impossible to apply the recombination curve to individual flares. However, ephemeris folding with a period of 237 days is applied to the data to construct a flare profile, after which the recombination curve is fitted to the folded data. Figure 4.7 shows the fits. Although the fits follow the general behaviour, it is evident that they have large uncertainties. The quiescent and peak electron densities from the fit to the CH_3OH time series are $\simeq$ (3.8 $\pm$ 1.4) $\times$ 10^5 cm^{-3}, and $\simeq$ (1.13 $\pm$ 0.26) $\times$ 10^6 cm^{-3}, and the quiescent and peak electron densities for the fit to the H_2CO time series are $\simeq$ (4.1 $\pm$ 1.6) $\times$ 10^5 cm^{-3}, and $\simeq$ (1.08 $\pm$ 0.17) $\times$ 10^6 cm^{-3}. The relative amplitudes from the observed flux densities for CH_3OH and H_2CO are between $\simeq$ 7-10 and $\simeq$ 4-7, respectively. As for the $n^2_{e,min}$ and $n^2_{e,max}$ values the relative amplitudes were determined to be 7.8 $\pm$ 7.1 for CH_3OH and 5.9 $\pm$ 5.0 for H_2CO, respectively. These large uncertainties are due to the large uncertainties in the obtained electron densities. However, they are still of the same order as the values from the observed flux densities.

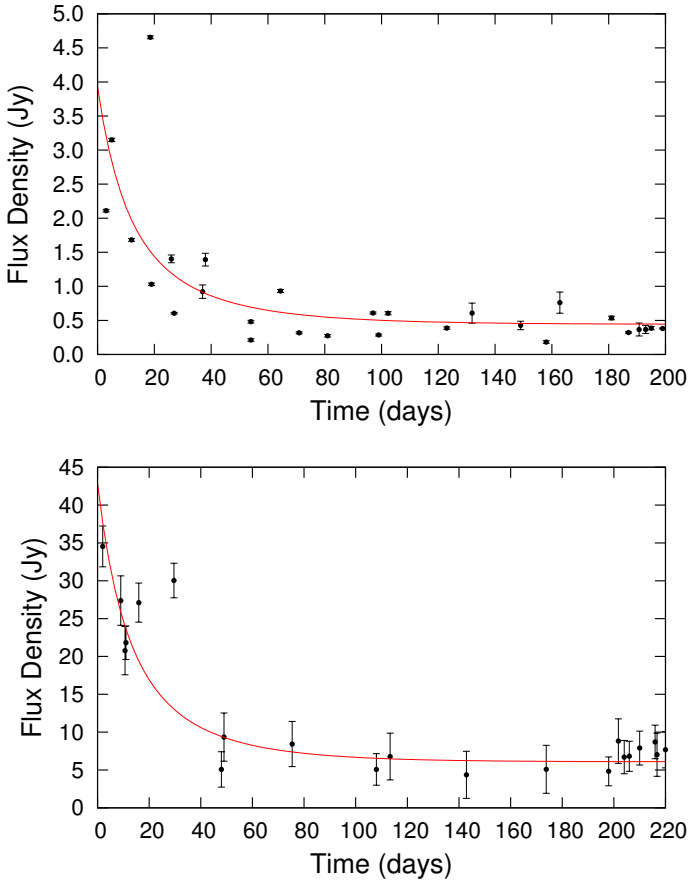

FIGURE 4.7: Here the fit of Equation 2.66 to the folded data is shown. Left panel: for the 87.8 km s^{-1} 6.7 GHz methanol maser velocity feature. Right panel: for the 79.5 km s^{-1} 4.8 GHz formaldehyde maser velocity feature.

4.3.4 G45.473+0.134

Although this source is somewhat better sampled than G37.55+0.20, the sampling is still inadequate to fit the recombination curve to any of the individual flares. As was done for G37.55+0.20, ephemeris folding of the data with a period of 196 days was done to construct a complete flare and fit the recombination curve. The best fit is shown by the red line in Figure 4.8. As for the case of G37.55+0.20, G45.473+0.134 also shows a flare, but the differences in the flux densities of consecutive flares are such that the errors on the fit are quite large. The best fit quiescent and peak electron density values to the folded data are $\simeq (4.6 \pm 0.8) \times 10^5$ cm^{-3}, and $\simeq (1.22 \pm 0.11) \times 10^6$ cm^{-3}, respectively. As to the relative amplitudes of G37.55+0.20, the uncertainties in the electron densities also lead to a large uncertainty in the relative amplitude for G45.473+0.134, where the values for the observed flux density range from 4-6. The value obtained from the electron densities is 5.79 ± 2.37. These values also compare well.

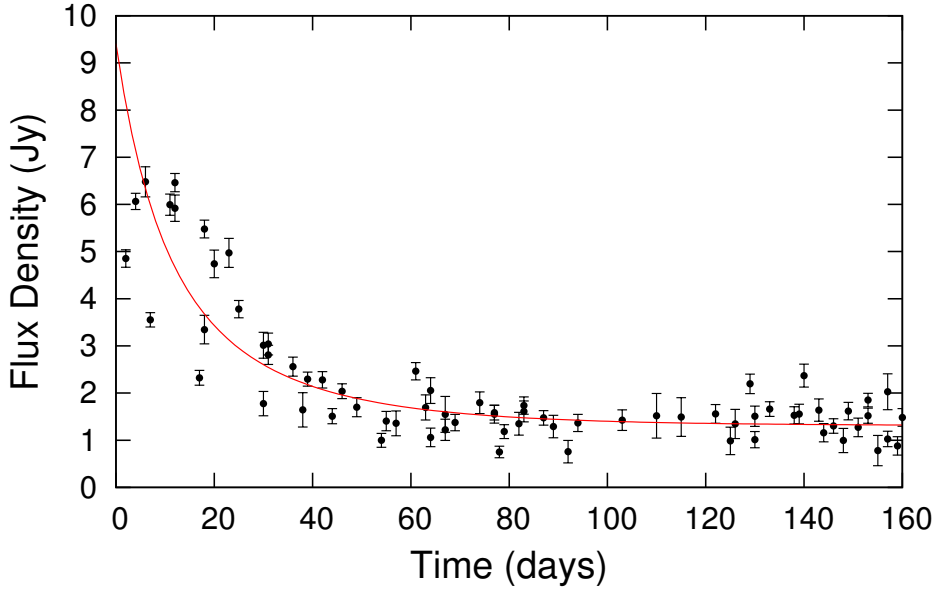

FIGURE 4.8: The Figure shows the fit of Equation 2.66 to the folded data of the 59.6 km s^{-1} 6.7 GHz maser velocity feature.

4.3.5 Summary of the flare fits

The electron densities obtained from the recombination curve fits for all four sources show remarkable similarity, as given in Table 4.1. The average peak electron densities for the four sources are: (1.13 ± 0.20) ×10^6 cm^{-3} (G9.62+0.20E), (1.08 ± 0.16) ×10^6 cm^{-3} (G22.357+0.066), (1.11 ± 0.22) ×10^6 cm^{-3} (G37.55+0.20), and (1.22 ± 0.11) ×10^6 cm^{-3} (G45.473+0.134), respectively. For the quiescent electron densities the averages are (5.6 ± 0.8) ×10^5 cm^{-3}, (6.7 ± 1.1) ×10^5 cm^{-3}, (4.0 ± 1.5) ×10^5 cm^{-3}, and (4.6 ± 0.8) ×10^5 cm^{-3}, respectively. The averages of the

peak values of the sources are the same within the error margins, as well as for the quiescent values as shown in Figure 4.9. The relative amplitudes from both the observed flux density and the fitted $n^2_{e,min}$ and $n^2_{e,max}$ values are also shown to be in good agreement. As shown in Section 3.6.2, the *shape* of the recombination curve depends on the peak and quiescent electron densities. This is most probably the reason why the flare profiles of these four sources are so similar, if the flares are indeed caused by the change in electron density in the partially ionized gas of the ionization front of the HII region.

Flare (MJD)	P n_e ($\times$ 10^6 cm^{-3})	Q n_e ($\times$ 10^5 cm^{-3})	$R_{observed}$ (R_{fitted})
G9.62+0.20E (244)			
53187	1.24 ± 0.10	6.9 ± 0.5	1.84 (2.24 ± 0.51)
53429	1.00 ± 0.11	5.2 ± 0.5	1.99 (2.69 ± 0.81)
53670	0.92 ± 0.07	5.3 ± 0.4	1.10 (2.03 ± 0.46)
53919	1.15 ± 0.07	6.3 ± 0.4	2.10 (2.39 ± 0.42)
54159	0.79 ± 0.04	4.1 ± 0.2	2.38 (2.84 ± 0.42)
54407	0.87 ± 0.04	4.3 ± 0.2	2.71 (3.04 ± 0.42)
54645	1.34 ± 0.15	5.8 ± 0.6	2.38 (4.38 ± 1.35)
55627	1.20 ± 0.09	5.4 ± 0.4	3.81 (3.88 ± 0.88)
55863	1.17 ± 0.18	6.8 ± 0.9	4.11 (1.99 ± 0.85)
56109	1.25 ± 0.11	6.0 ± 0.5	3.52 (3.33 ± 0.80)
56347	1.16 ± 0.07	5.5 ± 0.3	2.45 (3.45 ± 0.58)
56591	1.49 ± 0.10	5.6 ± 0.3	4.11 (6.29 ± 1.12)
56835	1.20 ± 0.09	5.7 ± 0.3	3.31 (3.43 ± 0.36)
G22.357+0.066 (179)			
55529	1.18 ± 0.02	8.2 ± 0.8	1.04 (1.07 ± 0.24)
55718	1.28 ± 0.03	7.7 ± 0.7	1.35 (1.72 ± 0.36)
55886	1.23 ± 0.04	6.9 ± 0.8	1.73 (2.20 ± 0.56)
56060	0.99 ± 0.02	6.0 ± 0.6	1.50 (1.74 ± 0.36)
56244	0.93 ± 0.02	6.4 ± 1.1	1.55 (1.14 ± 0.45)
56603	0.91 ± 0.02	5.3 ± 0.5	1.47 (1.99 ± 0.44)
G37.55+0.20 (237)			
CH_3OH	1.13 ± 0.26	3.8 ± 1.4	7-10 (7.8 ± 7.13)
H_2CO	1.08 ± 0.17	4.1 ± 1.6	4-7 (5.94 ± 5.03)
G45.473+0.134 (196)			
CH_3OH	1.22 ± 0.11	4.6 ± 0.8	4-6 (5.79 ± 2.37)

TABLE 4.1: The individual periodic maser sources with their associated periods, given in brackets. For each source, each flare is given as its associated time at the peak of the flare, using MJD convention, together with the corresponding quiescent and peak electron density from the recombination curve fits. The periods are obtained from e.g. Goedhart et al. (2003), Araya et al. (2010), Szymczak et al. (2011, 2015).

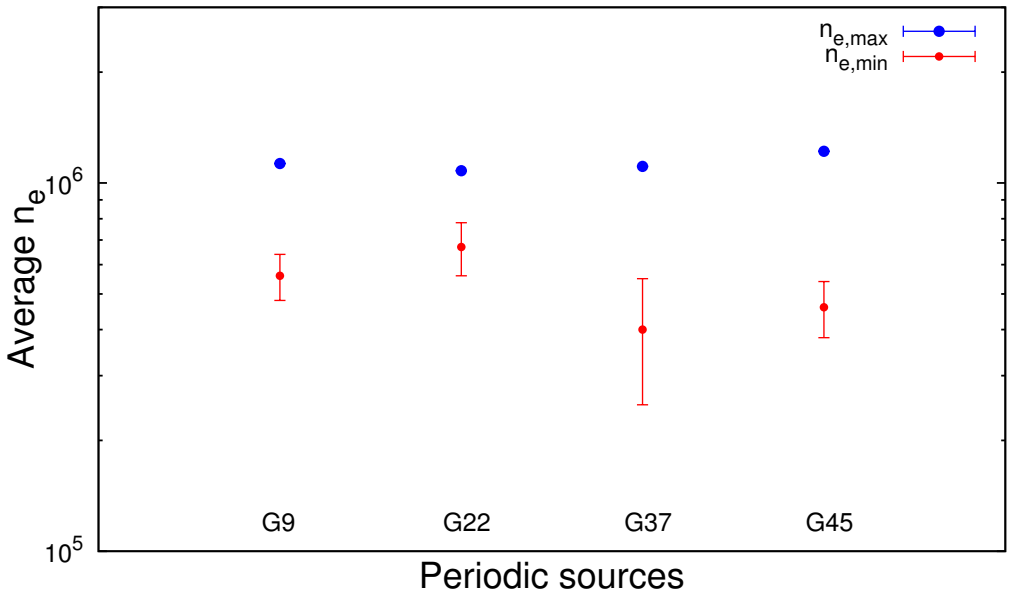

FIGURE 4.9: The average peak and quiescent electron densities with their error margins as derived from the recombination fits.

4.4 CWB model application and comparison

In this section the full CWB model will be used to calculate light-curves which can be compared with the observed flares of the four sources. In principle, to obtain the best "fit" of the CWB model to the observed maser light-curves, a minimal χ^2 analysis would have to be applied. However, as the CWB model is a complex four component and multi-parameter problem, several parameters which include the mass-loss rates of the stars, the stellar wind speeds, the eccentricity of the binary system for several periastron distances, stellar type, the density of the molecular cloud, and the position of the projection of the maser on the ionization front would have to be taken into account to find the best χ^2 fit. It was therefore decided to choose discrete points from the multi-dimensional parameter space and apply the modeling only for these sets of parameters. Additionally, as the CWB model has to be scaled to the maser light curves before comparison, applying a "χ^2" analysis would not necessarily be appropiate, and it was decided not to apply it.

First, the shocked gas of the colliding winds are simulated at discrete stellar separation distances with 0.1 AU intervals. These simulations were done for the combination of mass-loss rates and stellar wind speeds as given in Chapter 3. Second, from the initial consideration of van der Walt (2011) that the eccentricity of the binary system should be high, in order to obtain a "pulse" of ionizing photons around periastron, we considered five different orbits with periastron distances ranging from 0.6 - 1.0 AU with 0.1 AU intervals. Third, as we are uncertain of the densities

associated with these star forming regions, several constant densities for the *Molecular Cloud* (MC) in which the HII region evolves, were used as shown in Chapter 3. Additionally, the masers can be projected at different positions on the ionization front of the HII region. Thus, here four positions were chosen, where the edge of the maser (represented as a circle as shown in the top panel of Figure 2.12) closest to the star is projected at a density 90%, 80%, 60%, and 40% of the used density. Last, from the information obtained for the sources, five stellar types B0-O8 were chosen to obtain different sizes of the HII regions. The solutions from these calculations will then be compared to the observed light-curves.

Since only a very small subset of the total parameter space were used, it might result in solutions close to but not the same as found from the recombination fits. Additionally, the recombination fits for G9.62+0.20E and G22.357+0.066 show that each flare has its own associated quiescent and peak electron densities, and thus its own relative amplitude. A single CWB model which has a fixed set of parameters gives only a single solution (i.e. a constant relative amplitude and the same electron densities), and therefore cannot be compared with every single flare except if the associated electron densities are the same. Additionally, the increase in the electron density as discussed in Section 4.3.1 is artificially added to the solution using the gradient of $n^2_{e,min}$. If we assume that the decay of the flare profiles is described by a recombining partially ionized gas, to compare the CWB solution with the flare profile the quiescent and peak electron densities of the CWB model should be the same as the quiescent and peak electron densities obtained from the recombination fits.

From our hypothesis, we assume that the masers are projected against the partially ionized gas of the HII region at the position of the ionization front, i.e. as shown by the top panel of Figure 2.12, and we assume that the observed size of the HII region coincides with the position of the ionization front. Thus, we can match the simulated sizes of the HII regions for different densities and stellar types as closely as possible with the observed size of the HII regions, for those sources for which we have known sizes for the HII region. Additionally, if maser positions relative to the peak radio continuum are known, this can be used as an estimate to the position of the ionization front of the HII region. However, as mentioned throughout this thesis, the simulated HII regions only give the static equilibrium solution in which case the ionization front is located at the Strömgren radius. From Equations 2.36 and 2.39 the density and radius at which the HII region reaches pressure equilibrium is $\simeq 0.005$ and $\simeq 34$ times the initial values, respectively. To assume that we see these HII regions at the stage where they have just reached the initial Strömgren radius is perhaps an oversimplification. On the other hand, the assumption of the opposite, that the observed HII region is in pressure equilibrium with its surroundings, may also perhaps be an oversimplification. This is because, if the densities associated with these HII regions were initially $\geq 10^6$ cm^{-3}, this would mean (from Equation 2.36) that the electron density at pressure equilibrium should be $\geq 5 \times 10^3$ cm^{-3}, which is two orders of magnitude

below the fitted quiescent electron densities. Thus, to a large extent it can be assumed that if the initial Strömgren radius has been reached the HII region is still expanding towards pressure equilibrium.

The CWB model will first be compared to take into account the fitted quiescent electron density, the fitted peak electron density, and the size of the HII region. If there is no solution which can be compared with the flare profile by taking into account the size of the HII region, a CWB model with the closest values for the quiescent and peak electron densities is compared to the observed data, to show that it still describes the flare profile. In order to compare the CWB model to the observed flux density for the four sources, the solution, which is of the form n_e^2, is scaled to the observed flux density with the scaling factor as described in e.g. Section 4.3.1 where possible.

4.4.1 G9.62+0.20E

As seen in the time series of the 1.25 km s^{-1} velocity feature of the 12.2 GHz methanol maser shown in Figure 4.4, there is a gap of roughly two years without any observations. It is also apparent that the peak flux densities of the flares have significantly increased after the "gap" compared to those before the "gap". For this reason it was necessary that separate CWB models are compared with the data before and after the "gap".

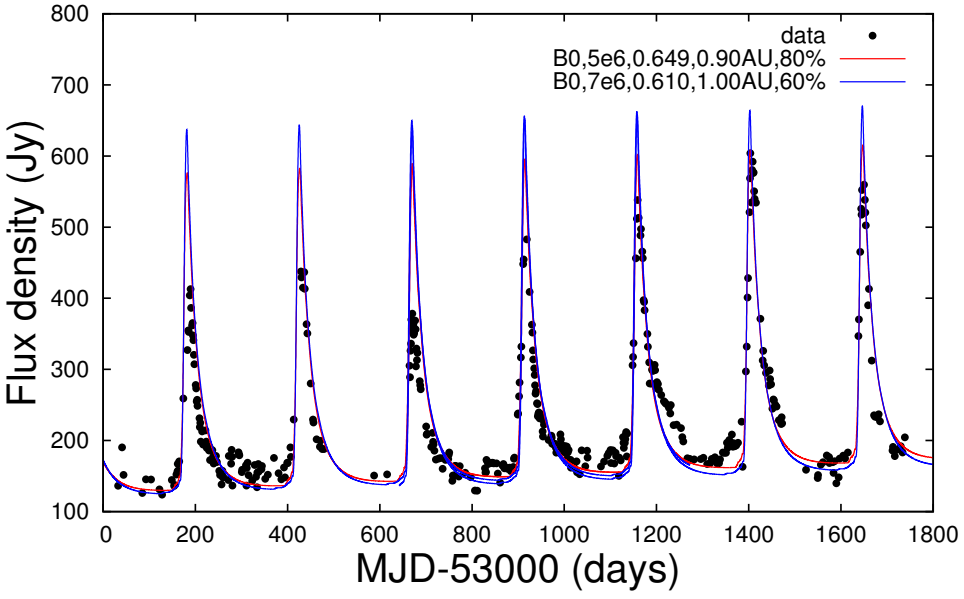

FIGURE 4.10: For the data before the "gap", the two comparisons shown by the blue and red line are obtained with different parameters, i.e. different molecular cloud densities, periastron distances and thus eccentricities, and projections of the maser on the ionization front. The red line has the parameters 5×10^6 cm^{-3}, 0.9 AU with $\epsilon = 0.65$, and projected at 80 % of the maximum electron density, whereas the blue line has the parameters, 7×10^6 cm^{-3}, 1.0 AU with $\epsilon = 0.61$, and projected at 60 % of the maximum electron density. Both were obtained using a B0 star as the central source.

Figure 4.10 shows a comparison of two CWB models to the data before the "gap". The red line was obtained by using the stellar parameter set CWB1 as given in Chapter 3, with a periastron distance of 0.9 AU, which from Equation 2.8 gives an eccentricity of $\simeq 0.65$. A constant neutral hydrogen density of 5×10^6 cm^{-3} with a B0 star were used for the HII region. The maser spot with a size of 2 AU was projected at 80% of the maximum electron density. The peak and quiescent electron densities for the red line are 1.21×10^6 cm^{-3} and 5.6×10^5 cm^{-3}, respectively. This compares well with the values obtained from the recombination curve fits. The luminosity of the shocked gas for a periastron distance of 0.9 AU is $\log L = 35.31$. The density and the stellar type used here resulted in an HII region with a radius of $\simeq 230$ AU, which is in good agreement with the linear sizes of ($\simeq 250 \pm 30$ AU) (Hofner et al., 1996), and ($\simeq 280 \pm 30$ AU) (Sanna et al., 2009, 2015) deduced for G9.62+0.20E for the distance of 5.2 ± 0.6 kpc. Additionally, as mentioned, we only use a small subset of the parameter space and want the size of the simulated HII region to compare as closely as possible to the observed size. However, it is also possible to compare CWB models with electron densities close to the values obtained, but for the parameters used (i.e. different density) the simulated HII region does not have the same size. For example, the blue line in Figure 4.10 was obtained with a periastron distance of 1.0 AU, eccentricity 0.61, neutral hydrogen density of 7×10^6 cm^{-3} (a HII region of size $\simeq 185$ AU), and the maser spot was projected at 60% of the maximum electron density. The luminosity of the shocked gas for a periastron distance of 1.0 AU is $\log L = 35.29$. The peak and quiescent electron densities for the blue line are 1.25×10^6 cm^{-3} and 5.4×10^5 cm^{-3}, respectively. These values also compare well with the recombination fit values. For the values given here the relative amplitude of the red line is 3.7, and the relative amplitude of the blue is 4.4. These values are somewhat higher than obtained from the recombination fits, but still compare relatively well. This is also seen from Table 4.1, as the relative amplitudes obtained from the recombination fits range between 2.0-4.4 (first seven flares).

A comparison of two CWB models to the data after the "gap" is shown in Figure 4.11. The parameters for the red line were for a periastron distance of 0.7 AU, eccentricity of 0.73, hydrogen density of 5×10^6 cm^{-3}, and a B0 star with the projection of the maser spot at 80% of the maximum electron density. The electron densities obtained from this comparison are 1.4×10^6 cm^{-3} and 5.6×10^5 cm^{-3} for the peak and quiescent electron density, respectively. The luminosity of the shocked gas for a periastron distance of 0.7 AU is $\log L = 35.42$ These values compare well with the fitted values. The blue line was obtained for a periastron distance of 0.9 AU, eccentricity 0.65, neutral hydrogen density of 7×10^6 cm^{-3}, a B0 star, and the projection of the maser spot was at 60% of the maximum electron density. The electron densities obtained from this comparison are 1.6×10^6 cm^{-3} and 5.4×10^5 cm^{-3} for the peak and quiescent electron density, respectively. The second comparison is again for a CWB model for which the simulated HII region does not match the derived size, but where the quiescent and peak electron densities still compare well with the values derived from the recombination fits. For the values obtained

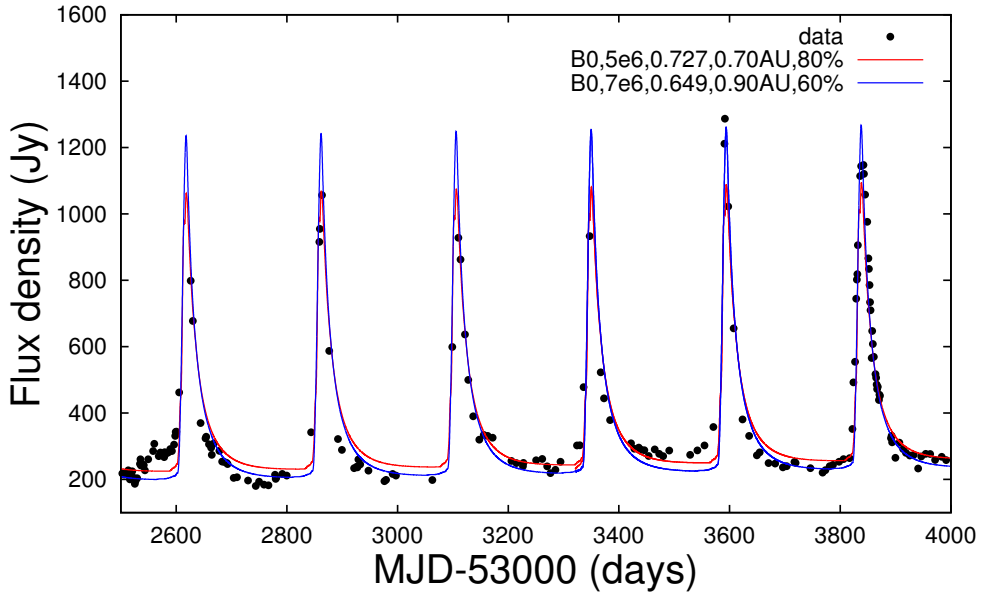

FIGURE 4.11: For the data after the "gap", the red line has the parameters 5×10^6 cm^{-3}, 0.7 AU with $\epsilon = 0.73$, and projection at 80 % of the maximum electron density, whereas the blue line has the parameters 7×10^6 cm^{-3}, 0.9 AU with $\epsilon = 0.65$, and projected at 60 % of the maximum electron density. Both were obtained using a B0 star as the central source.

for these flares, the relative amplitude of the red line is 5.3, and 7.8 for the blue line. Both these values are higher than the values (ranging between 2.0-6.3) obtained using the quiescent and peak electron densities from the recombination curve fits. However, it should be kept in mind that the uncertainty of where the peak of the flares begins could be a contributing factor to the discrepancy.

As mentioned earlier, the CWB model solutions have a fixed quiescent and peak electron density, i.e. a fixed relative amplitude. Thus, in order to incorporate the increase in the quiescent electron density, as found from the gradient of the linear regression fit applied to the quiescent flux density, this is included artificially to the CWB model solution. This is because, with the approach followed in this work, the time-dependent increase in the electron density can not be accounted for in the solution of the CWB model. With this approach, $n^2_{e,min}$ essentially follows the obtained gradient. However, as seen in Figure 4.4, the values obtained from the recombination fits do not correspond exactly with this trend, and we expect the CWB model comparison to at least show small a difference with the observed flux density.

4.4.1.1 A simple expansion model

It was mentioned earlier that it is possible that the HII region in G9.62+0.20E might still be expanding towards pressure equilibrium. From this perspective, the increase in the flux density can be explained if we assume the maser as stationary, as the observations of Minier et al. (2002),

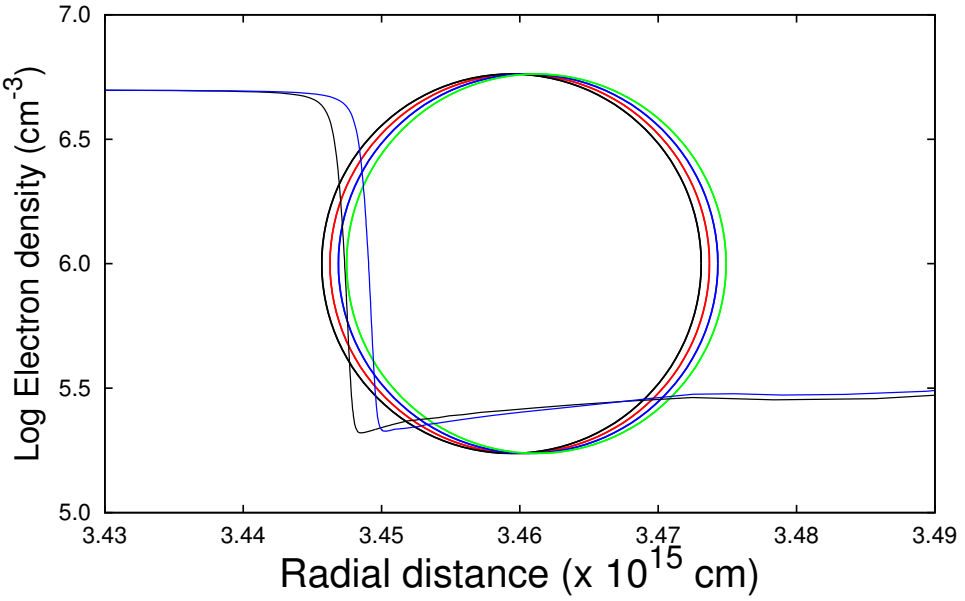

FIGURE 4.12: The projection of the maser spot on the ionization front of the background HII region. The four circles represent the projection of the maser spot on the ionization front (behind the maser) at four different times. The blue circle represents the projection of the maser spot relative to the ionization front at MJD 54000, and the red circle at MJD 56000. The black circle represents a time in the future and the green line a time in the past.

Goedhart et al. (2005) suggest, and for the ionization front of the HII region to expand across the line of sight of the maser spot. The time-dependent increase of the flux density (i.e. $\propto n_e^2$) can be explained within the framework of the expanding ionization front across the line of sight of the maser spot. To visualize this concept, Figure 4.12 shows four maser spots projected on the ionization front of the HII region. The four maser spots represents the relative position of the ionization front behind the maser spot at four different times. The blue circle represents the projection of the maser spot relative to the ionization front at MJD 54000, and the red circle at MJD 56000. On the other hand, the black circle represents a time in the future and the green line a time in the past. The HII region was obtained for a constant neutral hydrogen density of 5×10^6 cm^{-3} and a B0 star as used for the above comparisons.

Consider a simple model of the time-dependence of n_e^2 over the maser spot. By using the best fit expression (Equation 4.4) for the increase in $n_{e,min}^2$, the quiescent electron density can be obtained at two instances in the time series, at MJD 54000 and MJD 56000 as mentioned above. This can be written from Equation 4.4 as

$$n_e^2(1000) = 3.30 \times 10^7 t(1000) + 1.78e11 \quad (4.7)$$

$$n_e^2(3000) = 3.30 \times 10^7 t(3000) + 1.78e11. \quad (4.8)$$

After subtracting the first from the second and simplifying, we obtain

$$n_e^2(3000) - n_e^2(1000) = 3.30 \times 10^7 (t(3000) - t(1000)) \quad (4.9)$$

$$\rightarrow t(3000) - t(1000) = \frac{n_e^2(3000) - n_e^2(1000)}{3.30 \times 10^7}. \quad (4.10)$$

If we now define the velocity of the ionization front as $v_{IF} = (\Delta x/\Delta t)$, we obtain the following from Equation 4.10:

$$v_{IF} = \frac{\Delta x}{\Delta t} = \frac{\Delta x \cdot 3.30 \times 10^7}{n_e^2(3000) - n_e^2(1000)}, \quad (4.11)$$

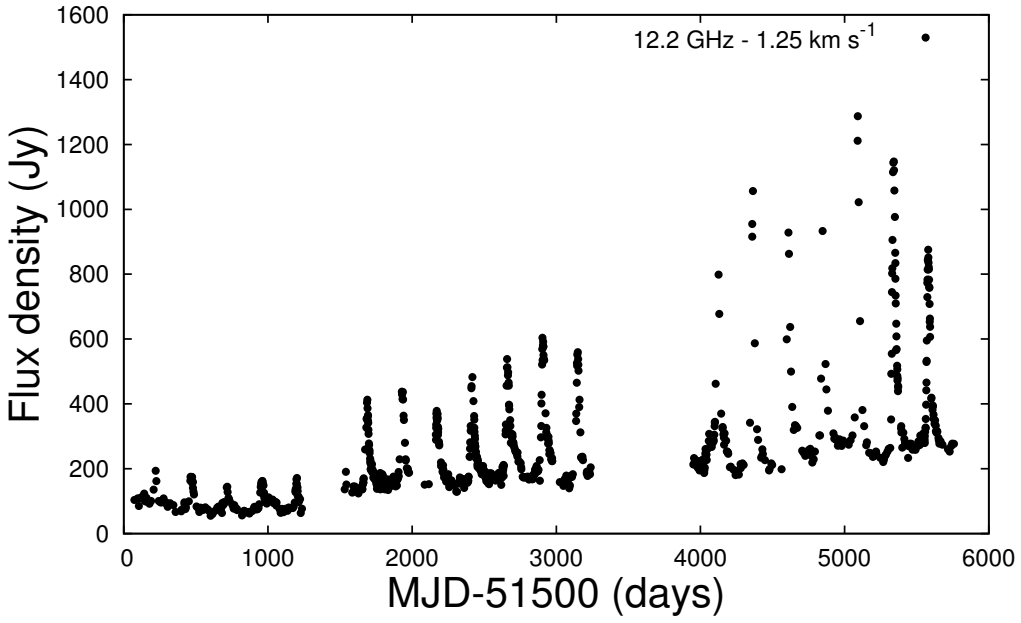

FIGURE 4.13: The time series of the 1.25 km s^{-1} velocity feature of G9.62+0.20E from MJD 51500 to MJD 57500.

Substituting the relevant n_e^2 values into Equation 4.4 and $\Delta x = 6.0 \times 10^9$ m, we obtain a velocity for the ionization front of $v_{IF} \approx 50$ m s^{-1}. We obtained the two electron densities at MJD 54000 and MJD 56000 for two separate projections of the maser spot on the ionization front, where the average electron density over the maser spot is the electron density obtained from the expression at those times. The difference in distance between these two projections is then simply Δx, which represents the distance the ionization front had to move across the line of sight of the maser spot during that time to result in the increase in the electron density. For the assumed size of the maser spot (2 AU), the ionization front (maintained by the ionizing flux of the star alone) will keep on expanding and reach a point where the projection of the maser spot will be inside the

ionization front (to the left of the ionization front in Figure 4.13). At that time the maser spot will only "see" the fully ionized gas, and the variability will completely disappear. During the time the maser spot "sees" the ionization front, not only will the quiescent electron density (i.e. the quiescent flux density) increase with time but, the peak electron density (represented by the additional influence on the ionization front) will also increase. This is seen in Figure 4.13, where the peak flux density has considerably increased over time.

Additionally, it is also expected from the expansion model that at a certain time the ionization front will reach the middle of the maser spot, up to that time the relative amplitude of the flares should keep on increasing. From that point in time onward, the relative amplitude will start to decrease, because the relative increase in the electron density at the peak will have become smaller. Lastly, if we look at earlier observations shown in Figure 4.13 at $\simeq$ MJD 53000, the quiescent flux density suddenly increases by $\simeq$ 50 Jy. Within the expansion scenario, this can be explained by the maser spot starting to "see" the ionization front of the HII region, i.e. at an earlier point in time the maser spot was only "seeing" the partially ionized gas outside of the ionization front. This can also explain why the amplitude of the flares during that early time is so small, because the maser spot only "saw" the ionization front when it was influenced by the additional flux of ionizing photons.

In light of this possibility, there are important implications to take note of: (1) if the ionization fronts of UCHII regions slow down to such low velocities after the initial Strömgren radius has been reached, it may explain the lifetime problem for UCHII regions found from observations (Wood & Churchwell, 1989, Churchwell, 2002, de Pree et al., 1995). The lifetime problem for UCHII regions is that there are more UCHII regions observed than the star formation rate and the IMF predicts. The expected number of UCHII regions was derived for a constant ionization front velocity of $\simeq$ 10 km s^{-1}, which is the sound speed in the ionized gas as the HII region reaches the Strömgren radius. Akeson & Carlstrom (1996) performed numerical calculations, that showed that the ionization front velocity slows down to $\simeq$ 1 km $^{-1}$ after a few tens of thousands of years after the initial Strömgren radius has been reached. (2) This velocity obtained for the speed at which the ionization front may possibly be expanding can also explain why the variability of the maser flares has been so stable. For the case where the ionization front expands with the speed of sound in the ionized gas, the variability of the masers (for a maser spot size of 2 AU) would have lasted for only $\simeq$ 1 yr. For the ionization front expanding at such lower velocities than the sound speed in the ionized gas, a velocity such as $\simeq$ 50 m s^{-1}, it is predicted that the variability will persist for $\simeq$ 200 yrs for a maser spot with a size of 2 AU. Keep in mind that even though the maser is assumed to be stationary, and the size of the maser used here may be idealistic, that the long term stability of the flaring may suggest a situation similar to this idealized case.

4.4.2 G22.357+0.066

The CWB models used to compare with the data shown in Figure 4.14 were obtained with a neutral hydrogen density of 7×10^6 cm^{-3}. The parameters for the blue line were: a periastron distance of 1.0 AU, an eccentricity of 0.52, a O9 star, and the projection of the maser spot at 60% of the maximum electron density. The quiescent and peak electron densities for the comparison of the blue line are $\simeq 6.41 \times 10^5$ cm^{-3} and $\simeq 1.05 \times 10^6$ cm^{-3}, respectively. The relative amplitude of this CWB model comparison is 1.68, which is within the range 1.0-1.7 obtained from the recombination fits. The parameters for the red line in Figure 4.14 were for a periastron distance of 0.9 AU, an eccentricity of 0.57, a O9 star, and the projection of the maser spot at 60% of the maximum electron density. The quiescent and peak electron densities are $\simeq 6.42 \times 10^5$ cm^{-3} and $\simeq 1.25 \times 10^6$ cm^{-3}, respectively. For this comparison, the relative amplitude is 2.8, which is larger than the obtained values from the recombination fits. This is seen in Figure 4.14, the quiescent electron density is scaled to the data and results in the peak of the CWB model comparison (the red line) to be higher than the data. Both of these CWB model comparisons seem to describe the flare profiles well.

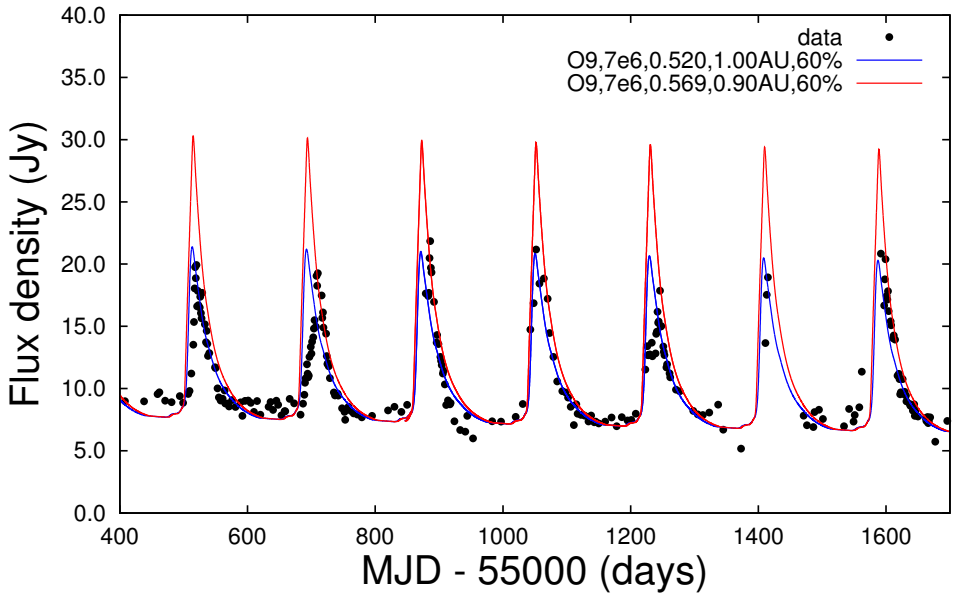

FIGURE 4.14: As for G9.62+0.20E, a comparison of two CWB models with the observed data of G22.357+0.066 is shown. The red line has the parameters 7×10^6 cm^{-3}, 0.9 AU with $\epsilon = 0.57$, and projected at 60 % of the maximum electron density, whereas the blue line has the parameters, 7×10^6 cm^{-3}, 1.0 AU with $\epsilon = 0.52$, and projected at 60 % of the maximum electron density. Both were obtained using a O9 star as the central source.

It was mentioned that it seems that the flux density of G22.357+0.066 is slowly decreasing with time. In Section 4.3.2 it was shown that with the error the gradient is smaller than 0. This is the opposite of that which was derived for G9.62+0.20E. For G9.62+0.20E, a possible explanation for the increase of the electron density with time was proposed as the ionization front expanding

across the line of sight of the maser spot. In the case of G22.357+0.066, there is not enough information available to make similar claims. However, a possibility might be that the maser spot and the ionization front might be moving relative to one another so as to result in a decrease in the electron density the maser spot "sees".

4.4.3 G37.55+0.20

For G37.55+0.20, it was mentioned that the CH_3OH and H_2CO masers are separated by $\simeq$ 2000 AU. It was also noted that these two maser species may be situated on opposite sides of an HII region. We want to match the size of the simulated HII region as closely as possible with the observed size ($\simeq$ 1000 AU, radius) by using a O8 spectral type star from Araya et al. (2004). The neutral hydrogen density which was necessary to obtain the size is $\simeq 10^6$ cm^{-3}. In this case there is something important to consider: in the ideal case of constant neutral hydrogen density, the minimum neutral hydrogen density has to be equal to or greater than the maximum electron density derived from the recombination fits. The average maximum electron density obtained is $\simeq 1.1 \times 10^6$ cm^{-3}, from which the neutral hydrogen density was taken as 1.5×10^6 cm^{-3}. The CWB model was calculated for several periastron distances, but for the used mass-loss rate combinations no CWB model solutions were obtained that could be compared to the maser light curve.

Two CWB models with quiescent and peak electron densities similar to the recombination fit values were compared to both the folded data and the time series of G37.55+0.20, shown in Figure 4.15. The blue line has quiescent and peak electron densities of $\simeq 4.37 \times 10^5$ cm^{-3} and $\simeq 1.38 \times 10^6$ cm^{-3}, respectively. The parameters used were a neutral hydrogen density of 6×10^6 cm^{-3}, a periastron distance of 0.8 AU, an eccentricity of 0.64, and the projection of the maser spot at 60 % of the maximum electron density. The red line has quiescent and peak values of $\simeq 4.38 \times 10^5$ cm^{-3} and $\simeq 1.30 \times 10^6$ cm^{-3}, respectively. The parameters used for this model were a neutral hydrogen density of 7×10^6 cm^{-3}, a periastron distance of 0.9 AU, an eccentricity of 0.56, and the projection of the maser spot at 60 % of the maximum electron density. Figure 4.15 shows the comparison of these two CWB models with the observed data (top panels) and folded data (bottom panels), for both the methanol (left panels) and formaldehyde (right panels) masers. As seen from Figure 4.15, there are differences between the CWB model and the flare profiles. However, Figure 4.15 still indicates that the data follows the time-dependent change of the electron density of a partially ionized gas changing its ionization state time-dependently. The model describes the flare profiles and the general form of the folded data well, even though the data sampling is so sparse.

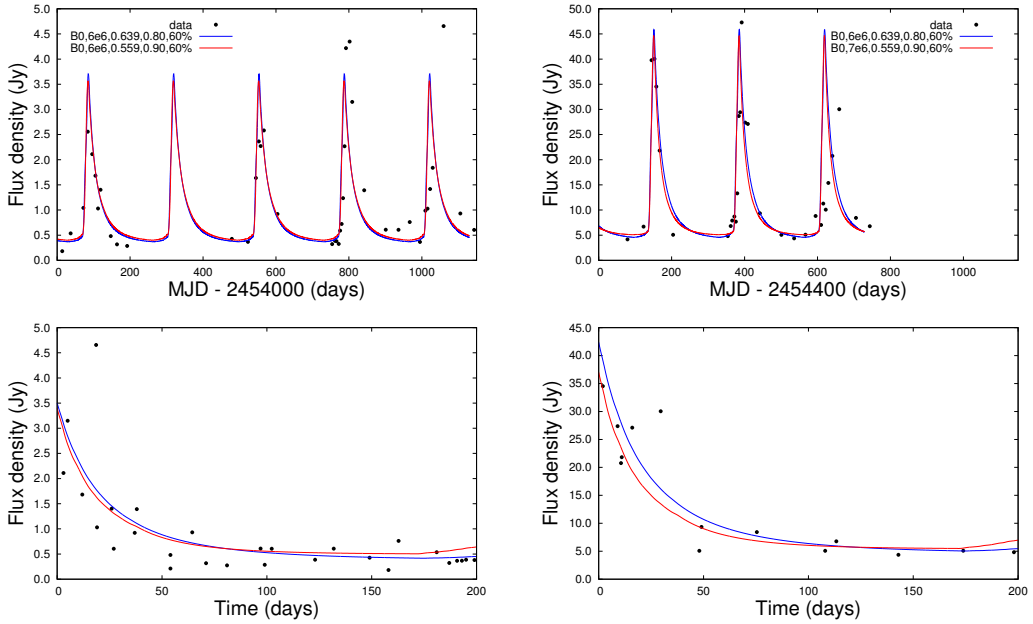

FIGURE 4.15: Left panels: two comparisons of the CWB models with the methanol (CH_3OH) maser time series and folded data. Right panels: two comparison of the CWB models with the formaldehyde (H_2CO) maser time series and folded data. The blue line is for a neutral hydrogen density of 6×10^6 cm^{-3}, a periastron distance of 0.8 AU, an eccentricity of 0.64, and the maser projection at 60 % of the maximum electron density. The red line is for a neutral hydrogen density of 7×10^6 cm^{-3}, a periastron distance of 0.9 AU, an eccentricity of 0.56, and the maser projected at 60 % of the maximum electron density.

4.4.4 G45.473+0.134

As described earlier, we want to compare the CWB model with the flare profile, where the parameters should be as close to the corresponding observed parameters as possible. In the case of G45.473+0.134, the star is approximately an O6 star (Kraemer et al., 2003), but there is no information as to the density or whether there is an HII region or not. This makes it almost impossible to match the model parameters with observed parameters. Thus, two CWB models with quiescent and peak electron densities similar to the values obtained from the recombination fits were compared to the folded data (top panel of Figure 4.16) and the time series (bottom panel of Figure 4.16). The two comparisons of the CWB models to the observed data shown in Figure 4.16 have the following parameters. The blue line is for a neutral hydrogen density of 7 $\times$ 10^6 cm^{-3}, a periastron distance of 1.0 AU, an eccentricity of 0.55, and the projection of the maser spot at 60 % of the maximum electron density. The resulting quiescent and peak electron densities for this fit are $\simeq$ 5.57 $\times$ 10^5 cm^{-3}, and $\simeq$ 1.26 $\times$ 10^6 cm^{-3}, respectively. The red line is for a neutral hydrogen density of 6 $\times$ 10^6 cm^{-3}, periastron distance of 0.9 AU, eccentricity of 0.59, and the projection of the maser spot at 60 % of the maximum electron density. The corresponding quiescent and peak electron densities are $\simeq$ 4.6 $\times$ 10^5 cm^{-3} and $\simeq$ 1.32 $\times$ 10^6 cm^{-3}, respectively. Both of the CWB model comparisons have values which overlap with the

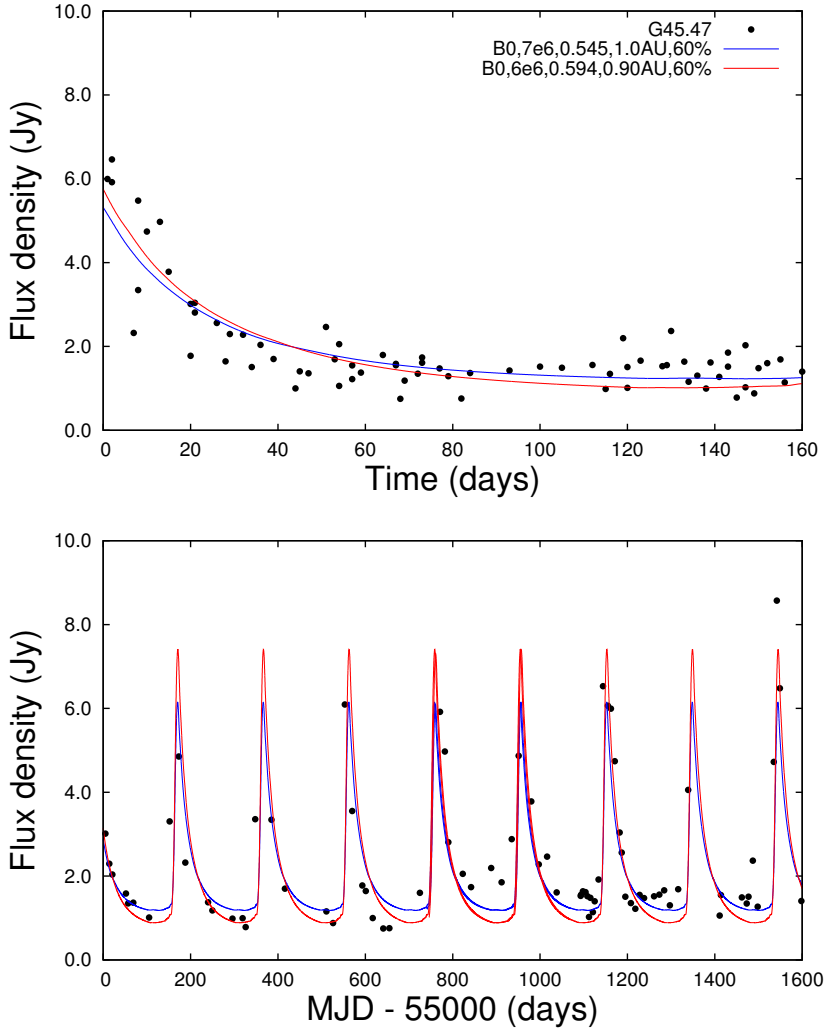

FIGURE 4.16: Top panel: the comparisons of two CWB models to the folded data of G45.473+0.134. Bottom panel: the comparisons of two CWB models to the time series of G45.473+0.134. The blue line is for a neutral hydrogen density of 7×10^6 cm^{-3}, a periastron distance of 1.0 AU, an eccentricity of 0.55, and the maser projection at 60 % of the maximum electron density. The red line is for a neutral hydrogen density of 6×10^6 cm^{-3}, a periastron distance of 0.9 AU, an eccentricity of 0.59, and the maser projected at 60 % of the maximum electron density.

values obtained from the recombination fits. The CWB models compare well with the folded data and the time series.

4.5 Summary and Conclusions

Flare (MJD)	Peak n_e ($\times 10^6$ cm^{-3})	Quiescent n_e ($\times 10^5$ cm^{-3})
G9.62+0.20E (244)		
Before gap	1.21	5.6
	1.25	5.4
After gap	1.40	5.6
	1.60	5.4
G22.357+0.066 (179)		
CH_3OH,H_2CO	1.05	6.4
	1.25	6.4
G37.55+0.20 (237)		
1	1.30	4.4
2	1.38	4.4
G45.473+0.134 (196)		
1	1.26	5.57
2	1.32	4.6

TABLE 4.2: Summary of the quiescent and peak electron densities for the individual CWB models compared to the observed flare profiles of the four sources.

The quiescent and peak electron densities associated for each comparison of the CWB model results with the four sources are summarized in Table 4.2. The CWB models with these values for G9.62+0.20E and G22.357+0.066 compare remarkably well with the values obtained from the recombination fits, which are summarized in Table 4.1. Additionally, although the data sampling is sparse for G37.55+0.20 and G45.473+0.134, the quiescent and peak electron densities obtained from the CWB models also compares well with the recombination curve fit values. All of these CWB models compare well with the observed flare profiles. Thus, the CWB model which describes the time-dependence of n_e, strongly suggests that the flare profiles can be explained within the CWB model framework as a partially ionized gas changing its ionization state time-dependently, initially increasing the electron density after which it recombines to a quiescent state before starting the next flare.

Chapter 5

Possible X-ray detection from embedded high-mass stars

5.1 Introduction

As discussed in Section 3.6.1, detecting changes in the radio free-free emission at such small scales at the transition of the ionization front of the HII region with conventional methods is almost impossible. However, the detection of X-rays from these HMSFRs may shed some light on the presence of such early binary systems. Here, we will attempt to resolve whether this is so.

Early-type massive stars of spectral type O and B, with their strong winds and high mass-loss rates, have been known to be X-ray emitters since the 1970's (Cooke et al., 1978). The X-ray emission from single O and B stars approximately scales as $L_x \sim 10^{-7} L_{bol}$ (Berghoefer et al., 1997), where L_x and L_{bol} are the X-ray and bolometric luminosities respectively, of which the thermal spectrum is predominantly soft ($kT \sim 0.2 - 1.0$ keV) (Sana et al., 2004). The X-ray emission in the winds of single stars is believed to be associated with shocks in the winds. It has also been established that massive star binaries, when their constituents are of the same luminosity class, show additional X-ray luminosity (Chlebowski & Garmany, 1991). EXOSAT observations of the source WR140 (Wolf Rayet star + O star) in the 1980's provided the best early case of colliding wind emission from a massive binary, where the observations revealed that $L_x/L_{bol} \simeq 10^{-5}$ (Williams et al., 1990). This over-luminosity is attributed to the hydrodynamical collision of the two stellar winds. Another possible mechanism that may produce additional X-ray emission is non-thermal synchrotron emission in the presence of strong magnetic fields. The production of synchrotron X-rays was numerically investigated by e.g. Pittard (2010a,b) and

Volpi (2011). However, here we neglect the contribution of non-thermal emission as a source of X-rays.

As discussed in Section 2.3.1, the Rankine-Hugoniot jump conditions dictate the physical state of the gas behind the shock. The temperature of the shocked gas is very high, and is approximately determined as $T_s \simeq 1 \times 10^7 v_8^2$ K, with v_8 in units of 1000 km s^{-1}. Thus, for highly supersonic winds ($v_8 > 1$) the temperature will be greater than 10^7 K, in which case X-rays are produced (Cooke et al., 1978). For adiabatic conditions these high temperatures of the shocked gas at the line of centers decrease as the gas flows away from the line of centers (Pittard, 1998). Therefore the shocked gas constitutes a multi-temperature gas that radiates at a wide range of energies as already described in Section 2.4.2.

Previously, in the calculations of the emission SED from the hot shocked gas, it was assumed that the effect of absorption is negligible in the stellar winds (Garcia-Segura & Franco, 1996). This effect was included in the simulations of the HII region in *Cloudy*. Although the HII region seems to be fully ionized by the stellar ionizing radiation (see Figure 3.8), the neutral hydrogen density increases gradually as function of radial distance as the ionization front is approached. Thus, the additional ionizing radiation from the shocked gas encounters an increasing neutral density as it propagates towards the ionization front. Figure 2.7 shows how the photo-ionization cross-section decreases with the increasing photon frequency in question. Thus the low energy photons ($\approx$ 13.6 eV) will be absorbed at the ionization front, leading to the change in the position of the ionization front as discussed in Chapter 3. However, at higher photon energies the cross-section becomes considerably smaller and these photons are able to travel large distances before being absorbed. The high temperature gas produced in the colliding winds may produce a significant flux of high energy X-rays, even though these sources are still deeply embedded in their parental clouds.

Since the early case of WR140, numerous sources have been found to behave as CWBs. A recent survey of CWBs done by Gagné et al. (2012) lists a number of O + O star binaries, as well as a number of WR + O binaries and WR + WR binaries. The X-ray luminosity of the O + O binaries range between $30.87 < \log L_x < 33.73$ (Gagné et al., 2012), whereas for the other two classes of binaries the luminosity ranges between $30.88 < \log L_x < 35.39$ (Gagné et al., 2012). These luminosities are for the energy range of $0.5 - 8$ keV, and their periods range from less than 2 days to several years. For instance, WR140 has an X-ray luminosity of $\log L_x \sim 34.68$, and $\log(L_x/L_{bol}) \simeq -4.75$, with a period of $\simeq 7.9$ yrs. A study done towards the 30 Doradus region in the Large Magellanic Clouds by Portegies Zwart et al. (2002) also reports a number of X-ray sources with luminosities of $\log L_x \simeq 32 - 35$. Additionally, the X-ray sources observed in the *Omega* nebula (M17) also follow the often-reported relation $L_x \simeq 10^{-7} L_{bol}$ (Broos et al., 2007). Broos et al. (2007) report of several possible colliding wind binary candidates based on

their hard X-ray spectrum ($\sim$ 4 keV). The range of unabsorbed X-ray luminosities in M17 is $29.8 < \log\ L_x < 33.3$ for 0.5 - 8 keV.

From the observation of several of these sources, some unexpected results were found. From the $L_x \propto 1/D_{sep}$ dependence of adiabatically shocked gas, the luminosity is expected to increase towards periastron in an eccentric system. Several studies (e.g. Corcoran, 2003, Fauchez et al., 2011, Sana et al., 2004), however, found a minimum in the luminosity around periastron in some of these sources. This behaviour was explained by the occultation of the shocked gas by the opaque wind from a WR star around periastron. This is normally the case in a WR + O star binary where the WR wind is opaque and absorbs the X-rays when the wind of the WR star is between the O star and the Earth. Pittard & Parkin (2010) and Parkin et al. (2011) have done 3D colliding wind binary simulations for η Carina and various other sources, and were able to reproduce the observed X-ray light curves with their simulations. Here, we want to calculate and predict the X-ray flux and light curve for possible CWBs still deeply embedded in their natal molecular clouds. In this case both stars are probably still young and of luminosity class V (see e.g. Panagia, 1973, Sternberg et al., 2003, for classification). From the abovementioned, for embedded stars the most probable case is that the early type winds of these stars are fully ionized, and occultation is probably negligible. The only source of absorption to be taken into account then is the interstellar gas between the sources and the Earth.

5.2 Attenuation of X-rays

Making use of the equation of radiative transfer, while assuming no emission along the line of sight to Earth ($\epsilon_\nu = 0$), equation 2.53 reduces to

$$I_\nu(l) = I_\nu(0)e^{-\tau_\nu(l)}, \tag{5.1}$$

where $I_\nu(0)$ is the intrinsic shocked gas flux, and $I_\nu(l)$ is the remaining flux after a distance l has been travelled. The optical depth of the intervening medium between the star forming region and Earth can be calculated from

$$\tau_\nu(l) = \sigma_\nu n_o l, \tag{5.2}$$

where τ_ν is the frequency-dependent optical depth, σ_ν the frequency-dependent photo-ionization cross section, and $n_o l$ the column density. The quantity n_o is the average neutral hydrogen density between the star forming region and Earth and l is the distance from the source to the Earth. In order to obtain the optical depth towards the sources of interest, we consulted

observations from literature. After obtaining the necessary column density, the calculations are done with the emission code developed by Dougherty et al. (2003) and Pittard & Dougherty (2006).

In order to obtain column densities towards the sources studied here, we are going to use three different ways, (1) from X-ray observations towards galactic center GMCs which, by the use of Gaussian spectral fitting, obtain the column density, (2) use of molecular line transitions of various molecules and the appropriate relations between these molecules and hydrogen, and (3) by use of the column density to visual extinction relation of Güver & Özel (2009). For the first method, from Sidoli et al. (2001) and Sidoli et al. (2006), the Gaussian spectral fitting applied to the observed SEDs of sources in the Galactic center obtains column densities in the order of 1 - 9 $\times 10^{23}$ cm^{-2}. On the other hand Nebot Gómez-Morán et al. (2013) have done an XXM-Newton survey of the Galactic plane and their results are summarized in their Table 1. From this table, there is a trend that the column density is higher towards the Galactic plane (all of which are above 10^{23} cm^{-2}, see Figure 5.1 which shows the column density as function of galactic latitude). All of the sources we investigate here lie between 0-0.2° in Galactic latitude, thus it is reasonable to assume that these sources have column densities in this range.

For the second method, the observation of molecular line transitions of molecules such as CO, ^{13}CO, CS, and NH_3, amongst others are considered. For example, there are observations available for G9.62+0.20E for the (3,3) transition of ammonia (NH_3) (see e.g. Garay & Lizano, 1999). The total hydrogen column density can then be obtained if the abundance of ammonia relative to molecular hydrogen (H_2) is known. Ungerechts et al. (1980), Genzel et al. (1982), and Henkel et al. (1987) amongst others have estimated the abundance of ammonia relative to molecular hydrogen to be of the order of 10^{-5} - 10^{-7} towards sites of massive star formation. The abundances of molecules are enhanced at sites of increased dust temperature due to the photo-evaporation of ice mantles (Garay & Lizano, 1999). From Garay & Lizano (1999), the ammonia column density for G9.62+0.20E is $\simeq 1 \times 10^{18}$ cm^{-2}, which implies an approximate total hydrogen column density of $\simeq 10^{24}$ cm^{-2}, if we assume a relative abundance of 10^{-6} for

Source	Distance (kpc)	N_{H_2} (cm^{-3})	Reference
G9.62 + 0.20E	5.2	10^{24}	1,2
		2×10^{23}	3,4,6
G22.357 + 0.066	4.7	3×10^{23}	5
		2×10^{23}	3,4,6
G37.55 + 0.20	6.7	3×10^{23}	5
		1.4×10^{23}	3,4,6
G45.473 + 0.134	6.0	3.2×10^{23}	3,4,6

TABLE 5.1: A summary of the column densities obtained as discussed, and the references used to obtain the column densities. The respective distances to the respective HMSFRs with the associated periodic methanol masers are also given. (1) Liu et al. (2011), (2) Anderson et al. (2009), (3) Schlafly & Finkbeiner (2011) (4) Nasa Extragalactic Database (NED), (5) Beuther et al. (2002a), (6) Güver & Özel (2009).

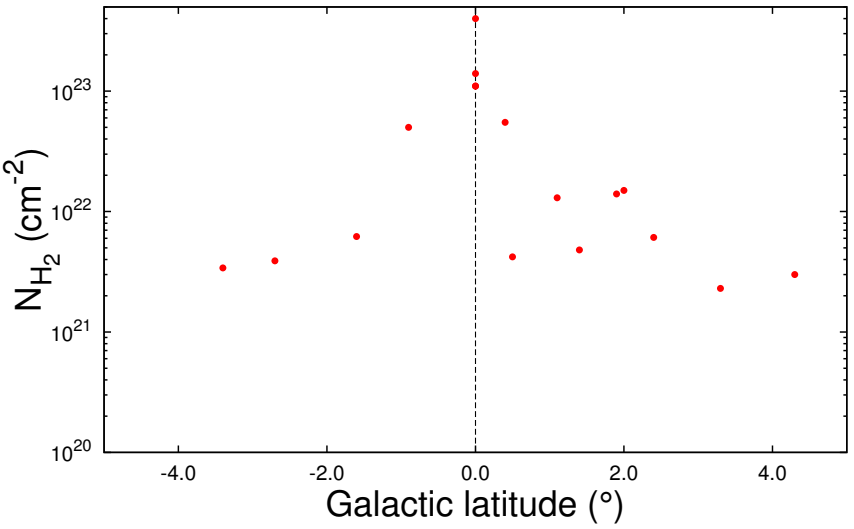

FIGURE 5.1: The column densities for the sources from the XMM-Newton survey of Nebot Gómez-Morán et al. (2013) as function of galactic latitude between -5° and 5°. The dashed line represent the galactic plane.

ammonia. On the other hand, for the third method using a more crude estimate, the hydrogen column density to visual extinction relation from Güver & Özel (2009) is used with the visual extinction values obtained from the *Nasa Extragalactic Database* (NED) (Schlafly & Finkbeiner, 2011) with the result, $\simeq 2 \times 10^{23}$ cm^{-2}.

Conversely, using the visual extinction relation from Güver & Özel (2009) as described above, the total hydrogen column densities for G22.357+0.066, G37.55+0.20, and G45.473+0.134 are found to be $\simeq 2 \times 10^{23}$ cm^{-2}, $\simeq 1.4 \times 10^{23}$ cm^{-2} and $\simeq 3.2 \times 10^{23}$ cm^{-2}, respectively. Beuther et al. (2002a) determined the total hydrogen column density towards G22.357+0.066 and G37.55+0.20 as $\simeq 3 \times 10^{23}$ cm^{-2}, using CS and C^{34}S observations. Lastly, Anderson et al. (2009) performed a ^{13}CO column density analysis towards various galactic HII regions, which was divided into several subsets. Assuming that all of these sources are in a relatively early stage of evolution, we use the *ultra compact* subset. By using the ^{13}CO column density (with the error margin) and the scaling relation $N(^{13}CO) = N(H_2) \cdot 8 \times 10^{-5}$ of Anderson et al. (2009), the hydrogen column density obtained in this way is in good agreement with the other values obtained. The respective distances to G22.357+0.066, G37.55+0.20 and G45.473+0.134 are 4.7 kpc, (Szymczak et al., 2011), 6.7 kpc, (Araya et al., 2004), and 6.0 kpc (Kraemer et al., 2003), respectively.

To put these values in perspective a well studied HMSFR, the *Omega* nebula (M17) has been extensively studied in the X-ray using *Chandra*. Broos et al. (2007, and references therein) obtained an interstellar extinction of $A_v \simeq 3$ towards M17. This translates into a column density of $\simeq 6 \times 10^{21}$ cm^{-2} from the Güver & Özel (2009) relation ($A_v \simeq 2 \times 10^{21}$ cm^{-2}). The average column density towards M17 is, however, $\log N(H_2) \simeq 23.1 \pm 0.6 \times 10^{23}$ cm^{-2} (Broos et al., 2007, Townsley et al., 2003), implying that the majority of material is located at the

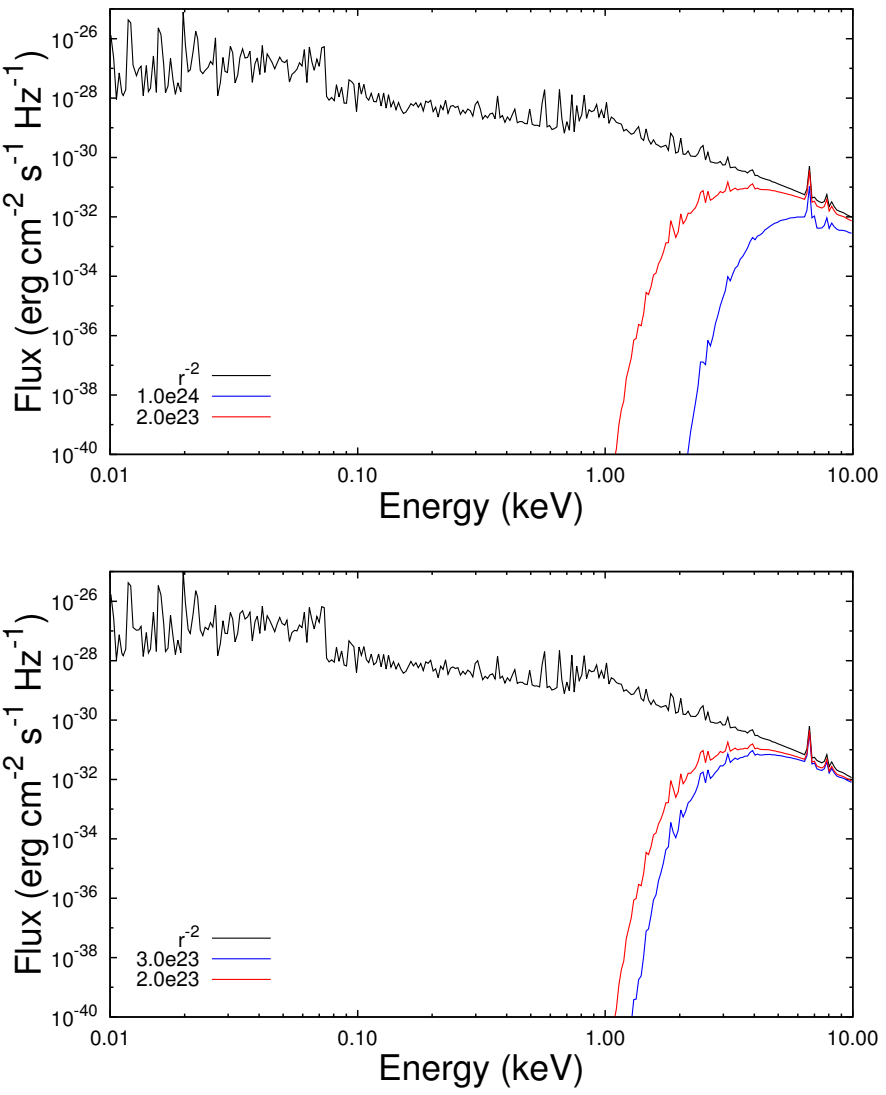

FIGURE 5.2: The geometrically diluted intrinsic spectrum for a stellar separation of 1.00 AU (black lines) (top and bottom panels). Top panel: Two attenuated spectra for different column densities, the blue line for a column density of 10^{24} cm^{-2} and red line for 2×10^{23} cm^{-2} for (G9.62+0.20E). Bottom panel: The red line is also for a column density of 2×10^{23} cm^{-2}, and the blue line for 3×10^{23} cm^{-2}, for (G22.357+0.066).

source. The distance to M17 is, however, only 1.6 kpc (Broos et al., 2007, Nielbock et al., 2001), therefore, although most of the material is probably located at the sources, the column densities towards the sources in question (ranging between $\simeq 1.8 - 2.4 \times 10^{22}$ cm^{-2}, for the respective distances to the sources, assuming the same extinction in all directions) may become a considerable fraction of the total column density because they are so distant.

Figure 5.2 shows the unabsorbed SED (black lines) and absorbed SEDs (red and blue lines) for G9.62+0.20E (top panel) and G22.357+0.066 (bottom panel), at the respective distances of 5.2 kpc and 4.7 kpc that would reach the Earth. The top panel of Figure 5.3 shows the same result for G37.55+0.20 at the distance of 6.7 kpc, whereas the bottom panel shows the result

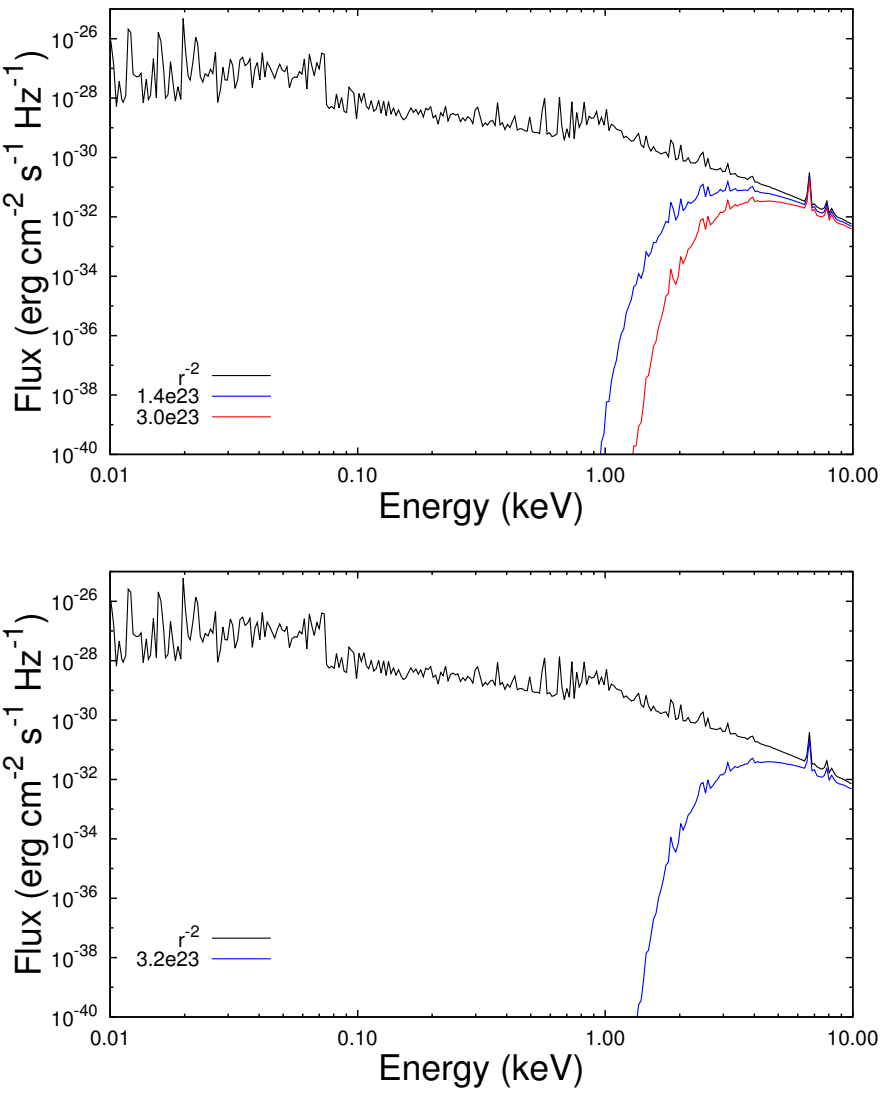

FIGURE 5.3: Same as in Figure 5.2, however, the column densities differ as well as the respective distances to the sources. Top panel: Two attenuated spectra for different column densities, the blue line for a column density of 1.4×10^{23} cm^{-2} and red line for 3×10^{23} cm^{-2}, for (G37.55+0.20). Bottom panel: The blue line is for a column density of 3.2×10^{23} cm^{-2}, for (G45.473+0.134).

for G45.473+0.134 at a distance of 6.0 kpc. These results are a SED for a stellar separation of 1.00 AU, for CWB model CWB1. The different column densities used for the calculations are given in Table 5.1, with their corresponding references. As shown, the results are expressed in erg cm^{-2} s^{-1} Hz^{-1} (Flux) and Energy (keV). From a comparison with SEDs from sources such as η Carina, WR140, and others (e.g. Sana et al., 2004), the only difference is the energy at which the spectrum turns over.

5.3 Calculated synthetic X-ray fluxes

The sources considered in this study have not been observed at X-ray energies. However, by use of the calculations of this study a synthetic phase-dependent X-ray flux can be calculated to predict if it might be possible to observe X-rays from these HMSFRs. For the presence of an eccentric colliding wind binary system, we expect the X-ray flux to be the highest around periastron. Thus, we consider an orbital phase of 0.4 around periastron, with periastron at phase 0.5. This is done from the SEDs of the different stellar separation distances, which are converted into the time dependence of the orbit and interpolated to obtain a time dependent solution. To determine if the remaining flux arriving at the observer would be high enough to be observed, the specifications of the *Advanced CCD imaging Spectrometer* (ACIS) on board the *Chandra*

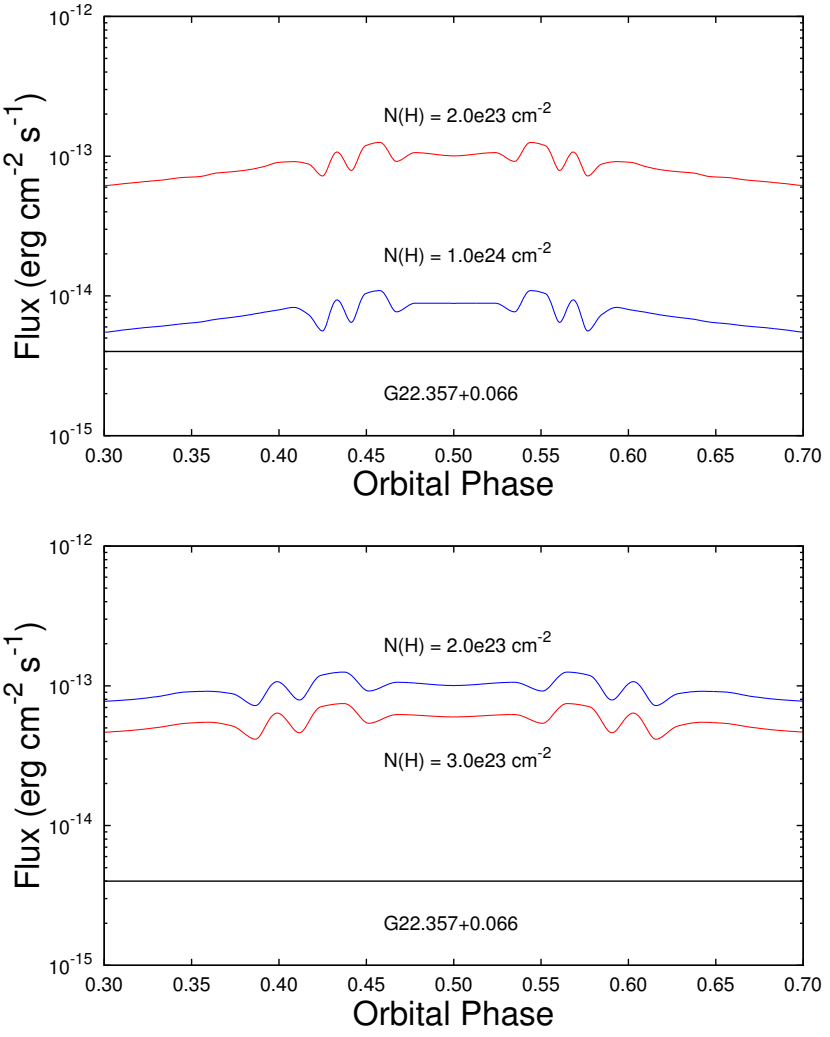

FIGURE 5.4: Here the time dependent integrated fluxes for G9.62+0.20E (top panel) and G22.357+0.066 (bottom panel) are given, only for an orbital phase of 0.4 around periastron. The different lines represent the different column densities used in the calculation of the attenuation. The threshold ($\simeq 4 \times 10^{-15}$ erg cm^{-2} s^{-1} for 10^4 seconds) for *Chandra* is also shown by the black horizontal line.

X-ray Observatory were used. The ACIS instrument is primarily used to observe X-rays with energies between 0.4 keV - 10 keV, with a threshold of $\simeq 4 \times 10^{-15}$ erg cm^{-2} s^{-1} in 10^4 seconds. The quasi-time dependent flux will be calculated in the next section, and compared with the threshold to determine if *Chandra* will be able to pick up a observable flux of X-rays from some of these HMSFRs.

From the colliding binary approach used, every calculated SED represents a specific time during the orbit of the binary system. In the adiabatic regime the SEDs are similar at the energies in question, as was shown in Chapter 3, with their flux increasing as the stellar separation decreases. However, for the stellar wind parameters used in this work, there are signs of radiative cooling for stellar separations smaller than 1.30 AU for a mass-loss combination of $1{\times}10^{-6} M_{\odot} yr^{-1}$, and $8{\times}10^{-7} M_{\odot} yr^{-1}$ (CWB1); and 1.10 AU for $8{\times}10^{-7} M_{\odot} yr^{-1}$ and $6{\times}10^{-7} M_{\odot} yr^{-1}$ (CWB3). This may cause variations in the integrated flux around periastron. As mentioned, several known colliding wind binary sources show variation around periastron (Sana et al., 2004, Fauchez et al., 2011, Corcoran, 2003). However, their behaviour is explained by occultation of the shocked gas by the opaque WR wind.

Although there is a difference in the flux for the different mass-loss rate combinations, here only the mass-loss rate combination of model CWB1 will be used. Also, because of variations in the radiative regime, a periastron distance of 0.90 AU is chosen to calculate the synthetic time dependent X-ray flux, and changes for various parameters relative to this result will be discussed. The results for all the sources are shown for periastron passage being at phase 0.50, with an orbital phase coverage of 0.4, as mentioned. For the periods of the four sources, this equates to a coverage of between $\simeq$ 72-96 days, for the four periods. Figures 5.4 and 5.5 show the orbital phase-dependent synthetic integrated fluxes (0.4 keV - 10 keV) of the four sources for the respective column densities given in Table 5.1. The threshold flux for 10^4 seconds of the ACIS instrument is shown with the horizontal black line. This shows that the synthetic integrated flux for all the sources and column densities is greater than the threshold, even for the extremely high column density of 1 $\times 10^{24}$ cm^{-2} associated with G9.62+0.20E. As mentioned, these results were obtained by only using a single parameter set for the wind parameters. As also discussed in Chapter 3, changing the stellar parameters will influence the SED from the shocked gas. Firstly, if the periastron distance of the binary orbit were to be decreased, the flux should increase and vice versa (although the radiative cooling just mentioned may also decrease the flux). If the stellar wind speeds of the individual stars of the binary system are slower, the shocked gas temperature will be lower, and the high energy flux will decrease, decreasing the flux and increasing the integration time necessary. For higher stellar wind speeds, the opposite happens, and the high energy flux will increase and the integration time necessary will decrease. Third, if the mass-loss rate is lower than that assumed here, the flux will decrease, and vice versa for high mass-loss rates. However, increasing the mass-loss rate may also cause an increase in

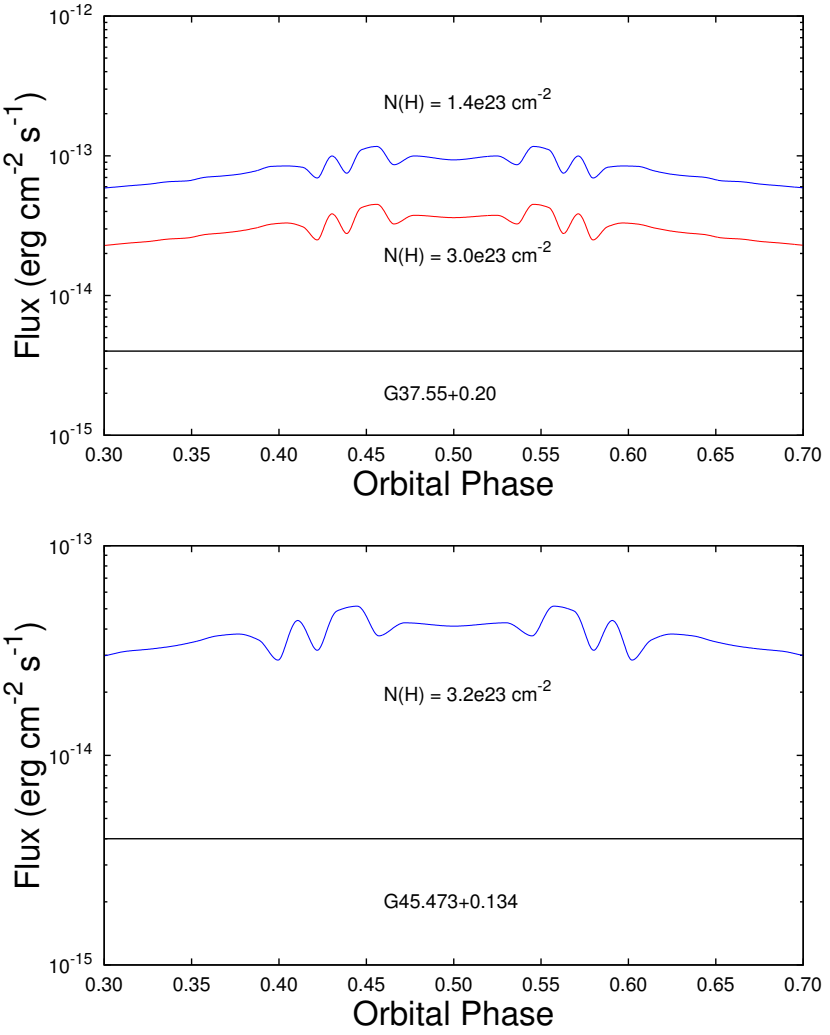

FIGURE 5.5: Figure 5.4 continued. Here, however, the time dependent integrated fluxes for G37.55+0.20 (top panel) and G45.473+0.134 (bottom panel) is given. The threshold ($\simeq 4 \times 10^{-15}$ erg cm^{-2} s^{-1} for 10^4 seconds) for *Chandra* is shown by the black horizontal line.

the effect of radiative cooling which will decrease the high energy flux. We do not have sufficient information as to the stellar properties of the periodic sources considered here. Thus taking into account the possible influence of stellar parameters on the resulting attenuated SED is somewhat difficult.

Considering these results we conclude that for the stellar parameters used in these calculations, we expect to detect X-rays towards these HMSFRs in 10^4 seconds if a binary system with similar stellar parameters is present. Even if the stellar parameters are different and decrease the integrated flux by an order of magnitude (for a column density of 1×10^{24} cm^{-2}), a detectable flux is still expected to be observed with an integration time not much longer than a few times 10^4 seconds.

Chapter 6

Summary and Discussion

6.1 Summary

The formation and evolution of massive stars are important topics of study, since massive stars play a key role in the evolution of galaxies. The study of their formation is complicated by their rarity, great average distances from the earth, their formation inside dense clusters, and that they are deeply embedded in their natal molecular clouds. To further add to all these difficulties, the rapid evolution and short-lived evolutionary phases of massive stars imply a smaller sample of such stars in each evolutionary stage (Shepherd & Churchwell, 1996, Zinnecker & Yorke, 2007, Ward-Thompson & Whitworth, 2011). Given these difficulties, it is not surprising that there is still no complete theoretical picture of the formation of massive stars.

As mentioned, the great distances at which these massive stars reside, make it difficult to study them and their environment. These great distances constrain the linear size that can be resolved at these sources for a given angular resolution. However, since the discovery of masers at sites of HMSF (e.g. Weaver et al., 1965, Menten, 1991), it has enabled us to study the environments of massive stars on much smaller scales, VLBI observations have found some of the methanol maser sizes (G9.62+0.20E) to be $\leq$ 10 AU (Goedhart et al., 2005). To date $\simeq$ 1000 sources showing methanol (CH_3OH) maser emission have been discovered (Caswell et al., 2010, 2011, Green et al., 2010, 2012). Both the widespread 6.7 GHz class II methanol masers discovered by Menten (1991), and the 12.2 GHz methanol masers (Batrla et al., 1987) have been found to be exclusively associated with HMSFRs (Ellingsen, 2006, Breen et al., 2010, 2013). Studies of 6.7 GHz methanol masers in HMSFRs suggest a correlation between the occurrence of methanol masers and the presence of HII regions (Caswell, 2009, Caswell & Breen, 2010, Sanna et al., 2010). It was recently discovered, that several methanol maser sources show periodic variability (Goedhart et al., 2003, 2004). In particular, the masers associated with the HMSFR G9.62+0.20E

show very interesting behaviour in that the increase in the flux density is very rapid with the onset of a flare, after which it decays for $\simeq$ 80-90 days (see van der Walt et al., 2016) until the flux reaches a quiescent flux density, where it remains for $\simeq$ 115 days until the next flare starts. Since the discovery of the periodic flaring behaviour of G9.62+0.20E, fifteen other sources have been observed to show regular/periodic flaring behaviour, and three others show the same flaring profile as G9.62+0.20E.

This study attempted to explain the flaring behaviour of the methanol masers associated with the HMSFR G9.62+0.20E, and the three sources G22.357+0.066, G37.55+0.20, and G45.473+0.134. The hypothesis was that the flare is caused by a *Colliding Wind Binary* system. The UV and X-ray photons produced from the very hot (10^6-10^8 K) shocked gas (colliding winds) are modulated by the stars' orbital motion in an eccentric binary system. This results in a "pulse" of ionizing photons around periastron. The "pulse" would then cause additional ionization in the partially ionized gas at the ionization front, i.e. change the position of the ionization front. It is then postulated that the periodic masers are located at such a position that it "sees" the change in the position (increase in the electron density) of the ionization front. The increase in the electron density would then subsequently cause an increase in the free-free emission from the ionization front of the background HII region. The subsequent decay of the flare profile of the periodic masers would then be caused by the recombination of the partially ionized gas, as the "pulse" diminishes towards apastron. A numerical model was constructed to account for all these different aspects. From the simple model of van der Walt (2011) a few questions were raised which we wanted to address in this work. First, would the energetic output from the shocked gas be enough to cause such changes at the ionization front? Second, what would the properties of the shocked gas be to result in such changes, and lastly, would the changes in the position be able to explain the flare profiles? The results of these investigations follow.

6.1.1 Results from the CWB model

For the parameters used in this work, the shocked gas of the *Colliding wind Binary* cools adiabatically ($L_{shock} \propto D^{-1}$) for the largest part of the binary orbit. Close to periastron (for an eccentric orbit) cooling of the shocked gas is mainly radiative. For the luminosity $L_\star \simeq 10^{38.5}$ erg s^{-1} of a B0 star from Sternberg et al. (2003), the luminosity of the shocked gas for adiabatic cooling conditions were found as $L_{shock} \leq 2 \times 10^{-4}\ L_\star$. This means that the luminosity has this maximum value for the smallest stellar separation for which the gas still cools adiabatically. On the other hand, for radiative cooling it was found that $2 \times 10^{-4} L_\star \leq L_{shock} \leq 10^{-3}\ L_\star$. For adiabatically cooling gas, the emitted SEDs are almost identical, the only difference being that the flux increase/decrease as the stellar separation changes or the mass-loss rate changes. Note

that in this work the stellar wind velocities were kept constant for all the mass-loss rate combinations. When the gas cools radiatively, a large fraction of the gas has a lower temperature, which results in an enhancement in the low energy flux.

From these SEDs, the *Cloudy* simulations showed that the influence on the ionization front is the largest for SEDs produced from gas dominated by radiative cooling. The flux of lower energy photons for adiabatic cooling gas seems to be too low to result in significant changes in the position of the ionization front. On the other hand, the increased flux at lower energies for SEDs produced from radiative cooling gas results in significant changes in the position of the ionization front of order a few times 10^{12} cm. From (Gagné et al., 2012), the luminosity of the shocked gas calculated here is in good agreement with surveys done of CWBs. This strongly suggests that we should expect the energy generated from the shocked gas to cause sufficient changes in the position of the ionization front in order to also affect the free-free emission. This substantial influence on the ionization front occurs for stars at least as early as O8 and a density as low as 1.5×10^6 cm^{-3}.

For the radially-dependent electron density structure obtained from the *Cloudy* simulations, it was shown that the HII region is optically thin from the ionization front to the maser along the line of sight. This justifies the use of the time-dependent solution of n_e to represent the time-dependent change in the free-free emission. It was also shown that for lines of sight passing through the ionization front, the ionization front is optically thick for the radio free-free emission propagating from the far-side of the ionization front towards the maser. This means that the maser should only "see" the free-free emission from the ionization front itself. From this result, the time-dependent ionization rate was constructed and used to solve for n_e time-dependently, and the behaviour of $n_e(t)$ was described for various system parameters. From this behaviour, it was possible to determine that the minimum electron density to which the flares of these sources should recombine to is higher than 3×10^5 cm^{-3}. This is because the recombination time for values smaller than this would be longer than the period of all of these sources, and the decay part of the flare would not have reached its quiescent state before the next flare has started. For all four sources it was shown, that the flares recombine to a quiescent state before the next flare starts, thus the quiescent electron density should be higher than this value.

6.1.2 Results from the flare analysis and CWB model comparison

From the assumption that the decay part of the flare is due to the recombination of a partially ionized gas, the flares were fitted with Equation 2.66. For the sparse data sampling of the sources G37.55+0.20 and G45.473+0.134, ephemeris folding was applied to construct a single flare profile in order to fit Equation 2.66. For all the sources, the recombination of a partially ionized gas describes the decay of the flare profiles remarkably well. The average peak electron densities for

the four sources were found as: (1.13 ± 0.20) $\times 10^6$ cm^{-3} (G9.62+0.20E), (1.08 ± 0.16) $\times 10^6$ cm^{-3} (G22.357+0.066), (1.11 ± 0.22) $\times 10^6$ cm^{-3} (G37.55+0.20), and (1.22 ± 0.11) $\times 10^6$ cm^{-3} (G45.473+0.134), respectively. From these results, this is the reason for the abovementioned 1.5 $\times$ 10^6 cm^{-3} limit. Whereas the average quiescent electron densities were found as: (5.6 ± 0.8) $\times 10^5$ cm^{-3} (G9.62+0.20E), (6.7 ± 1.1) $\times 10^5$ cm^{-3} (G22.357+0.066), (4.0 ± 1.5) $\times 10^5$ cm^{-3} (G37.55+0.20), and (4.6 ± 0.8) $\times 10^5$ cm^{-3} (G45.473+0.134), respectively. Although, the error for G37.55+0.20 includes 3 $\times$ 10^5 cm^{-3}, the results still indicate that all the quiescent state electron densities are indeed above this value. Additionally, note that both the peak and quiescent electron densities overlap when their errors are taken into account. As mentioned in chapter 4, this may be the reason why the flare profiles of these sources are so similar.

For G9.62+0.20E, it can be seen that the quiescent state flux density is steadily increasing with time. This was also found by a linear regression fit to the quiescent state flux density. The opposite, that the quiescent state flux density is decreasing with time, was found for G22.357+0.066. The increase in the quiescent state flux density of G9.62+0.20E, is proposed to be due to the expansion of the ionization front in the reference frame where the maser is stationary and for the ionization front to expand across the line of sight of the maser spot. From the size of the maser spot (2 AU) that we have used in this work, and the parameters used to compare the CWB model with the data, we derived an ionization velocity of $\simeq$ 50 m s^{-1}. A quantitative discussion (assuming this velocity) within the expanding ionization front framework explains the observed time-dependent flux densities well. It also explains the long-lived stable variability observed, because if the ionization front of the HII region was to expand at the sound speed ($\simeq$ 10 km s^{-1}) in the ionized gas, the ionization front would have expanded across the line of sight of the maser spot (with a size of 2 AU) in $\approx$ 1 yr. This is significantly shorter than the 20 yrs over which the variability have been monitored. From this result, we predict that the variability of the masers in G9.62+0.20E will continue for an extended period of time before the ionization front moves across the line of sight of the maser spot entirely. For the velocity of the ionization front derived, the lifetime of the variability is predicted to persist for $\simeq$ 200 years. For G22.357+0.066, it is unclear what causes the decrease in the flux density, however, the decreasing electron density explains the decreasing flux density for optically thin conditions. With G22.357+0.066, the opposite might be happening, i.e. the relative motion between the maser spot and the ionization front may be causing the decrease in the electron density. The other two sources do not have enough information in order to apply such an expanding ionization front model to the observed flux densities. This scenario, that the ionization front is expanding very slowly (much slower than the theoretical value of the sound speed of $\simeq$ 10 km s^{-1} in the ionized gas), may explain the UCHII region lifetime problem that have been found (e.g. Wood & Churchwell, 1989, Churchwell, 2002, de Pree et al., 1995). This is because there are more UCHII regions observed than the star formation rate and IMF predict. Numerical simulations were also performed by Akeson & Carlstrom (1996), which found that the velocity of the ionization front

slows down to a velocity of $\simeq 1$ km $^{-1}$ after a few times 10^4 years, after the initial Strömgren radius have been reached.

The CWB model were compared to the observed maser light curves, and it showed that the CWB model compares remarkably well. The comparison was made by scaling $n_e^2(t)$ to the quiescent state flux densities. The scaling factor was obtained from the linear regression applied to the quiescent state electron densities in chapter 4 for G9.62+0.20E and G22.357+0.066, and for the other two sources it was simply scaled with the obtained quiescent state electron density. This suggests the maser flares can be explained by the change in the electron density at the ionization front of a background HII region, i.e. the change in the radio free-free emission from the ionization front of the HII region for optically thin conditions.

6.1.3 The results from the X-ray predictions

As mentioned in Chapter 5, it would be very difficult to directly observe changes in the radio free-free emission from the transition from fully ionized to partially ionized gas of the HII region, i.e. the ionization front, and another method have to be used to test the CWB hypothesis. In the case of the presence of a CWB, the shocked gas produces X-rays and a synthetic SED is calculated up to 10 keV. The X-rays at $\simeq 10$ keV can propagate large distances before being absorbed, because of their small photo-ionization cross-sections. In Chapter 5, it was shown that for the presence of a CWB system for the column densities $\simeq 10^{23-24}$ cm^{-2} used, X-rays should be detectable from all four sources with *Chandra*, if *Chandra* was pointed at the sources for an integration time of 10^4 seconds. For G9.62+0.20E, the expected fluxes at periastron for a column density of 2×10^{23} and 10^{24} cm^{-2} are $\simeq 10^{-13}$ erg cm^{-2} s^{-1} and $\simeq 10^{-14}$ erg cm^{-2} s^{-1}, respectively. In the case of G22.357+0.066, the expected fluxes at periastron are $\simeq 1.2 \times 10^{-13}$ erg cm^{-2} s^{-1} (2×10^{23} cm^{-2}) and $\simeq 8 \times 10^{-14}$ erg cm^{-2} s^{-1} (3×10^{23} cm^{-2}). For G37.55+0.20, the expected fluxes are $\simeq 10^{-13}$ erg cm^{-2} s^{-1} (1.4×10^{23} cm^{-2}) and $\simeq 8 \times 10^{-14}$ erg cm^{-2} s^{-1} (3×10^{23} cm^{-2}). Lastly, the expected flux for G45.473+0.134 is also $\simeq 8 \times 10^{-14}$ erg cm^{-2} s^{-1} (3.2×10^{23} cm^{-2}).

6.2 Evaluation and criticism of the current work

We have investigated the possibility that the periodicity of the methanol masers are due to the presence of a *Colliding Wind Binary* system. This was done by putting together, the 2D hydrodynamical simulation of the shocked gas, the plasma emission model, the photo-ionization code *Cloudy*, and the time-dependent calculation of the electron density in the partially ionized gas of the ionization front using the projection of the maser spot. Although it is possible to simulate the shocked gas with 3D hydrodynamical simulations, the 2D static equilibrium

simulations from the hydrodynamic simulations are good enough as long as the stellar wind velocities are sufficiently higher than the orbital speed. This is because the effect of the Coriolis force is almost negligible in this case (Stevens et al., 1992). Thus, the equilibrium states of the shocked gas provides a relatively accurate representation of the shocked gas to calculate the emission. Additionally, the *Cloudy* simulations result in static equilibrium solutions of the radially-dependent electron density for the HII region, and the time-dependent electron density is solved for by using these equilibrium states. Although the equilibrium states from *Cloudy* provides no time-dependent information (as discussed in Chapter 3), and the time-dependent solution of the electron density do not contain any radial-dependent information; it has been shown that the periodic methanol masers can be explained by the time-dependent change of electron density caused by the presence of a CWB. Thus, it indicates that the approach followed in this work, connecting four different calculations to arrive at a result, is a reasonably accurate complex approach of the qausi-time-dependent representation of the full time-dependence.

As a result of this investigation, several assumptions were made which may have important implications within the framework of the CWB model. An important result that precedes these assumptions, is that it was found that in order to produce a significant influence on the ionization front the shocked gas have to undergo radiative cooling close to periastron. Thus, the original CWB model used by van der Walt (2011) which only considered the shocked gas to cool adiabatically, would most probably not result in the necessary influence on the ionization front to explain the change in the free-free emission, but for radiative cooling close to periastron it would be able to. Furthermore, we also found that the requirement of a very high eccentricity orbit for the model of van der Walt (2011) is significantly relaxed.

It was assumed that the molecular clouds in which the HII regions reside and evolve has a constant neutral hydrogen density. This is, however, most probably an oversimplification. How would a different density structure, such as a radially-dependent density structure, impact the influence on the ionization front? Test simulations were done with *Cloudy* for such a radially-dependent density structure, and found that (apart from the size of the HII region that changes) the influence (for the same SED) on the ionization front actually increases. This has an interesting implication, in that within the same framework the mass-loss rate or eccentricity can be lowered and still obtain the same result. Thus, even less energy from the shocked winds will be necessary to explain this phenomenon. Although, we only assume a constant density structure to construct the CWB model, a different density structure (and possibly even an inhomogeneous density structure) could also explain the flare profile. Additionally, as discussed in chapter 3, the adjusted chemical abundance of Mg, Si, and Fe play an important role in the interpretation of the CWB model, in order for the HII region to be optically thin at 12.2 GHz from the ionization front towards the maser. Observational evidence of the presence of dust coincident with the UCHII region of G9.62+0.20E (**?**), and similar observations from Osterbrock et al. (1992) and Esteban et al.

(1998) seem to substantiate this claim. Thus, it is reasonable to assume that these elements are depleted from the gas phase, and for the HII region to be optically thin. However, in the event that this is not the case, where the dust have been destroyed by e.g. radiation pressure, the HII region would be optically thick for free-free emission at 12.2 GHz from the ionization front outward. This would mean that we would not be able to explain the periodicity in the methanol masers as the increase in the free-free emission due to changes in the electron density at the ionization front of the HII region. Which has an important implication for the CWB framework, as this means that the periodicity will probably only be observable in a specific timeframe during the evolution of the HII region, where dust is still present in the vicinity of the ionization front. Additionally, from the proposed projection of the masers on the partially ionized gas of the ionization front, the masers may simply be projected such that at this point they "currently see" the ionization front, as we are still uncertain where precisely these masing cloudlets form. However, although the HII region has to be optically thin, and that the masers have to be projected favourably, it is not necessarily an unlikely possibility that these constraints are "currently" met.

In addition, with conventional continuum observations, the linear size that can be probed at these distant sources depends on the angular resolution that can be achieved by the telescope(s). On the other hand, because masers have such high brightness temperatures, they provide an excellent tool to probe small scale (AU) variations, which by conventional observations would be almost impossibe. In chapter 4, it has been shown that the quiescent state flux density of G9.62+0.20E follows the quiescent state electron density obtained from the recombination curve fits very well. This strongly suggests that the maser light curve follows the time-dependent change in the electron density. The clouds in which these HII regions evolve also need not be homogeneous, such that different masers projected at different positions on the ionization front would not necessarily give the exact same flare profile. In this regard, the flare profile of two different velocity features need not be the same in order to describe it as a time-dependent change in the electron density, i.e. free-free emission. Szymczak et al. (2015) critisized the CWB model, because the variability index of individual maser velocity features of G22.357+0.066 are not the same. However, it is possible to explain different flare profiles in the same source with inhomogeneous density structures at different positions on the ionization front of the HII region. This can be seen from chapter 3, where different densities or projections of the maser spot of the ionization front were shown. Although there are these outstanding questions, which will follow below, the fact that the time-dependent change in the electron density describes the maser light curves so well, points to the CWB model as a strong candidate to explain these periodic methanol maser light curves as the time-dependent change in the electron density. Lastly, the detection of X-rays for long enough exposure times from these star forming regions may shed some light on the presence of CWBs, which would give additional merrit to this hypothesis.

6.3 Unanswered and outstanding questions

- What is the statistical probability of forming massive binary systems with the periods of 179, 196, 237, and 244 days investigated? From the surveys of e.g. Mason et al. (1998) and the numerical simulations of (Bonnell, 2001, Bonnell et al., 2004) the mass ratio of massive stars in binary systems tends to be ≥ 0.5. The surveys of e.g. Mason et al. (1998) and García & Mermilliod (2001) also found the multiplicity of massive stars to be as high as 75%. This has important implications on the IMF as it suggests the secondary star in a binary system, at the high-mass end of the IMF, is not "sampled" from the "standard" IMF, although the numerical simulations of Bonnell (2001) and Bonnell et al. (2004) seem to reproduce the IMF. Additionally, the numerical simulations of Bate et al. (2002b) describe the formation of close/compact binaries by the transfer of angular momentum from the circumstellar disk to the orbit of the binary system. On the other hand, wide binaries can be explained by the fragmentation of collapsing cores (Bodenheimer, 1995).

- Are the elements Mg, Si, and Fe still in the dust phase for the sources that we have investigated? From the shell-like morphologies seen in the MIR emission of many compact HII regions (see for example Phillips & Ramos-Larios, 2008) suggest that some of the dust has been cleared out of the ionized volume either through destruction or by radiation pressure. However, there may still be significant amounts of dust inside the HII region, as found by De Buizer et al. (2003) from MIR emission associated with G9.62+0.20E (one of the periodic sources investigated here). Thus, in the vicinity of the ionization front of the HII region, the destruction of dust may not be important and the abundance of Mg, Si, and Fe might be low.

- If the velocity of ionization fronts of UCHII regions are much lower than $\simeq 10$ km s^{-1} after the initial Strömgren radius have been reached, is the stable long-lived variability of G9.62+0.20E and possibly the other sources an indication of a slightly later stage in the evolution of the UCHII region?

- Except for the time-dependent change in the electron density at the ionization front of an HII region, what other possible phenomenon would be able to explain the same maser flare profile for two different maser species? From the flare analysis, the decay of the flares is very well described by a recombining partially ionized gas of the ionization front of an HII region. Additionally, the CH_3OH and H_2CO masers are pumped by different mechanisms (van der Walt, 2014), which strongly suggests a common pumping mechanism for the variability.

6.4 Conclusion

We have presented the numerical model used to compare the CWB hypothesis with the observed maser light curves. With this model we were able to add additional physics to the simple toy model of van der Walt (2011), which include the physical properties of the shocked gas from where we were able to calculate the SEDs. From these SEDs it was found that the ionization front would be influenced, which strongly suggests that there is enough energy produced from the shocked gas. In view of the remarkable comparison of the CWB model with the maser light curves, it strongly suggest that a CWB system can explain the flaring behaviour of the periodic methanol masers. Although there are several unanswered and outstanding questions that arose from this work. The fact that the recombination of a partially ionized gas describes the decay part of these flares so well, strongly points to the variability arising from time-dependent changes in the electron density and thus the free-free emission from the background HII region.

Bibliography

Akeson, R. L. & Carlstrom, J. E. 1996, ApJ, 470, 528

Anderson, L. D., Bania, T. M., Jackson, J. M., et al. 2009, ApJS, 181, 255

André, P. 2001, in ESA Special Publication, Vol. 460, The Promise of the Herschel Space Observatory, ed. G. L. Pilbratt, J. Cernicharo, A. M. Heras, T. Prusti, & R. Harris, 169

Andrè, P. & Motte, F. 2001, in Astronomical Society of the Pacific Conference Series, Vol. 235, Science with the Atacama Large Millimeter Array, ed. A. Wootten, 11

André, P., Motte, F., & Belloche, A. 2001, in Astronomical Society of the Pacific Conference Series, Vol. 243, From Darkness to Light: Origin and Evolution of Young Stellar Clusters, ed. T. Montmerle & P. André, 209

Andre, P., Ward-Thompson, D., & Barsony, M. 1993, ApJ, 406, 122

Andre, P., Ward-Thompson, D., & Barsony, M. 2000, Protostars and Planets IV, 59

Araya, E., Hofner, P., Kurtz, S., et al. 2005, ApJ, 618, 339

Araya, E., Hofner, P., Linz, H., et al. 2004, ApJS, 154, 579

Araya, E., Hofner, P., Sewiło, M., et al. 2007, ApJ, 669, 1050

Araya, E. D., Hofner, P., Goss, W. M., et al. 2010, ApJ, 717, L133

Bally, J. & Zinnecker, H. 2005, AJ, 129, 2281

Bartkiewicz, A., Szymczak, M., & van Langevelde, H. J. 2014, 564, A110

Bartkiewicz, A., Szymczak, M., van Langevelde, H. J., Richards, A. M. S., & Pihlström, Y. M. 2009, 502, 155

Bate, M. R., Bonnell, I. A., & Bromm, V. 2002a, MNRAS, 332, L65

Bate, M. R., Bonnell, I. A., & Bromm, V. 2002b, MNRAS, 336, 705

Bate, M. R., Bonnell, I. A., & Bromm, V. 2003, MNRAS, 339, 577

Batrla, W., Matthews, H. E., Menten, K. M., & Walmsley, C. M. 1987, Nat, 326, 49

Berghoefer, T. W., Schmitt, J. H. M. M., Danner, R., & Cassinelli, J. P. 1997, 322, 167

Bergin, E. A. & Tafalla, M. 2007, ARA&A, 45, 339

Bernabeu, G., Magazzu, A., & Stalio, R. 1989, 226, 215

Beuther, H., Churchwell, E. B., McKee, C. F., & Tan, J. C. 2007, Protostars and Planets V, 165

Beuther, H., Linz, H., & Henning, T. 2012, 543, A88

Beuther, H., Schilke, P., & Gueth, F. 2004, ApJ, 608, 330

Beuther, H., Schilke, P., Menten, K. M., et al. 2002a, ApJ, 566, 945

Beuther, H., Schilke, P., Sridharan, T. K., et al. 2002b, 383, 892

Beuther, H., Sridharan, T. K., & Saito, M. 2005, ApJ, 634, L185

Blitz, L. 1991, in NATO Advanced Science Institutes (ASI) Series C, Vol. 342, NATO Advanced Science Institutes (ASI) Series C, ed. C. J. Lada & N. D. Kylafis, 3

Blitz, L. & Williams, J. P. 1999, in NATO Advanced Science Institutes (ASI) Series C, Vol. 540, NATO Advanced Science Institutes (ASI) Series C, ed. C. J. Lada & N. D. Kylafis, 3

Blondin, J. M. & Stevens, I. R. 1990, in baas, Vol. 22, Bulletin of the American Astronomical Society, 1294

Bodenheimer, P. 1995, ARA&A, 33, 199

Bodenheimer, P., Ruzmajkina, T., & Mathieu, R. D. 1993, in Protostars and Planets III, ed. E. H. Levy & J. I. Lunine, 367–404

Bonnell, I. A. 1999, in NATO Advanced Science Institutes (ASI) Series C, Vol. 540, NATO Advanced Science Institutes (ASI) Series C, ed. C. J. Lada & N. D. Kylafis, 479

Bonnell, I. A. 2001, in IAU Symposium, Vol. 200, The Formation of Binary Stars, ed. H. Zinnecker & R. Mathieu, 23

Bonnell, I. A., Bate, M. R., Clarke, C. J., & Pringle, J. E. 1997, MNRAS, 285, 201

Bonnell, I. A., Bate, M. R., & Zinnecker, H. 1998, MNRAS, 298, 93

Bonnell, I. A., Clarke, C. J., Bate, M. R., & Pringle, J. E. 2001, MNRAS, 324, 573

Bonnell, I. A., Vine, S. G., & Bate, M. R. 2004, MNRAS, 349, 735

Bontemps, S., Motte, F., Csengeri, T., & Schneider, N. 2010, 524, A18

Breen, S. L., Caswell, J. L., Ellingsen, S. P., & Phillips, C. J. 2010, MNRAS, 406, 1487

Breen, S. L., Ellingsen, S. P., Contreras, Y., et al. 2013, MNRAS, 435, 524

Broos, P. S., Feigelson, E. D., Townsley, L. K., et al. 2007, ApJS, 169, 353

Carroll, B. & Ostlie, D. 2007, An Introduction to Modern Astrophysics

Caswell, J. L. 2009, Proc. Astron. Soc. Aust., 26, 454

Caswell, J. L. & Breen, S. L. 2010, MNRAS, 407, 2599

Caswell, J. L., Fuller, G. A., Green, J. A., et al. 2010, MNRAS, 404, 1029

Caswell, J. L., Fuller, G. A., Green, J. A., et al. 2011, MNRAS, 417, 1964

Cesaroni, R. 2005, in Massive Star Birth: A Crossroads of Astrophysics

Cesaroni, R., Felli, M., Testi, L., Walmsley, C. M., & Olmi, L. 1997, 325, 725

Chlebowski, T. & Garmany, C. D. 1991, ApJ, 368, 241

Churchwell, E. 2002, ARA&A, 40, 27

Codella, C., Lorenzani, A., Gallego, A. T., Cesaroni, R., & Moscadelli, L. 2004, 417, 615

Codella, C. & Moscadelli, L. 2000, 362, 723

Cooke, B. A., Fabian, A. C., & Pringle, J. E. 1978, Nat, 273, 645

Corcoran, M. F. 2003, in IAU Symposium, Vol. 212, A Massive Star Odyssey: From Main Sequence to Supernova, ed. K. van der Hucht, A. Herrero, & C. Esteban, 130

Cragg, D. M., Sobolev, A. M., & Godfrey, P. D. 2005, MNRAS, 360, 533

Crowther, P. A., Schnurr, O., Hirschi, R., et al. 2010, MNRAS, 408, 731

Cyganowski, C. J., Brogan, C. L., Hunter, T. R., & Churchwell, E. 2009, ApJ, 702, 1615

De Buizer, J. M. 2003, MNRAS, 341, 277

De Buizer, J. M., Radomski, J. T., Telesco, C. M., & Piña, R. K. 2003, ApJ, 598, 1127

de Pree, C. G., Rodriguez, L. F., & Goss, W. M. 1995, 31, 39

de Villiers, H. M., Chrysostomou, A., Thompson, M. A., et al. 2014, MNRAS, 444, 566

de Wit, W. J., Testi, L., Palla, F., Vanzi, L., & Zinnecker, H. 2004, 425, 937

Dougherty, S. M., Pittard, J. M., Kasian, L., et al. 2003, 409, 217

Draine, B. T. 2011, Physics of the Interstellar and Intergalactic Medium

Duquennoy, A. & Mayor, M. 1991, 248, 485

Dyson, J. & Williams, D. 1997, The Physics of the Interstellar medium

Elitzur, M. 1992, ARA&A, 30, 75

Ellingsen, S. P. 2006, ApJ, 638, 241

Elmegreen, B. G. 1985, in Protostars and Planets II, ed. D. C. Black & M. S. Matthews, 33–58

Elmegreen, B. G. 1993, in Protostars and Planets III, ed. E. H. Levy & J. I. Lunine, 97–124

Esteban, C., Peimbert, M., Torres-Peimbert, S., & Escalante, V. 1998, , 295, 401

Falgarone, E., Phillips, T. G., & Walker, C. K. 1991, ApJ, 378, 186

Fauchez, T., De Becker, M., & Nazé, Y. 2011, Bulletin de la Societe Royale des Sciences de Liege, 80, 673

Ferland, G. J., Korista, K. T., Verner, D. A., et al. 1998, PASP, 110, 761

Fontani, F., Cesaroni, R., Caselli, P., & Olmi, L. 2002, 389, 603

Franco, J., Kurtz, S., Hofner, P., et al. 2000, ApJ, 542, L143

Franco, J., Tenorio-Tagle, G., & Bodenheimer, P. 1990, ApJ, 349, 126

Gagné, M., Fehon, G., Savoy, M. R., et al. 2012, in Astronomical Society of the Pacific Conference Series, Vol. 465, Proceedings of a Scientific Meeting in Honor of Anthony F. J. Moffat, ed. L. Drissen, C. Robert, N. St-Louis, & A. F. J. Moffat, 301

Garay, G. & Lizano, S. 1999, PASP, 111, 1049

Garay, G., Rodriguez, L. F., Moran, J. M., & Churchwell, E. 1993, ApJ, 418, 368

García, B. & Mermilliod, J. C. 2001, 368, 122

García, J., Elhoussieny, E. E., Bautista, M. A., & Kallman, T. R. 2013, ApJ, 775, 8

Garcia-Segura, G. & Franco, J. 1996, ApJ, 469, 171

Genzel, R., Ho, P. T. P., Bieging, J., & Downes, D. 1982, ApJ, 259, L103

Goedhart, S., Gaylard, M. J., & van der Walt, D. J. 2003, MNRAS, 339, L33

Goedhart, S., Gaylard, M. J., & van der Walt, D. J. 2004, MNRAS, 355, 553

Goedhart, S., Maswanganye, J. P., Gaylard, M. J., & van der Walt, D. J. 2014, MNRAS, 437, 1808

Goedhart, S., Minier, V., Gaylard, M. J., & van der Walt, D. J. 2005, MNRAS, 356, 839

Green, J. A., Caswell, J. L., Fuller, G. A., et al. 2010, MNRAS, 409, 913

Green, J. A., Caswell, J. L., Fuller, G. A., et al. 2012, MNRAS, 420, 3108

Güver, T. & Özel, F. 2009, MNRAS, 400, 2050

Hartquist, T. W., Menten, K. M., Lepp, S., & Dalgarno, A. 1995, MNRAS, 272, 184

Henkel, C., Wilson, T. L., & Mauersberger, R. 1987, 182, 137

Henning, T., Schreyer, K., Launhardt, R., & Burkert, A. 2000, 353, 211

Hillenbrand, L. A. & Hartmann, L. W. 1998, ApJ, 492, 540

Ho, P. T. P. & Haschick, A. D. 1981, ApJ, 248, 622

Hoare, M. G., Kurtz, S. E., Lizano, S., Keto, E., & Hofner, P. 2007, Protostars and Planets V, 181

Hofner, P., Kurtz, S., Churchwell, E., Walmsley, C. M., & Cesaroni, R. 1994, ApJ, 429, L85

Hofner, P., Kurtz, S., Churchwell, E., Walmsley, C. M., & Cesaroni, R. 1996, ApJ, 460, 359

Hosokawa, T. & Omukai, K. 2008, in Astronomical Society of the Pacific Conference Series, Vol. 387, Massive Star Formation: Observations Confront Theory, ed. H. Beuther, H. Linz, & T. Henning, 255

Howarth, I. D. & Smith, K. C. 2001, MNRAS, 327, 353

Hu, B., Menten, K. M., Wu, Y., et al. 2016, ApJ, 833, 18

Inayoshi, K., Sugiyama, K., Hosokawa, T., Motogi, K., & Tanaka, K. E. I. 2013, ApJ, 769, L20

Jijina, J. & Adams, F. C. 1996, ApJ, 462, 874

Kaastra, J. S. & Mewe, R. 2000, in Atomic Data Needs for X-ray Astronomy, ed. M. A. Bautista, T. R. Kallman, & A. K. Pradhan, 161

Kennicutt, R. C. 2005, in IAU Symposium, Vol. 227, Massive Star Birth: A Crossroads of Astrophysics, ed. R. Cesaroni, M. Felli, E. Churchwell, & M. Walmsley, 3–11

Kim, K.-T. & Koo, B.-C. 2001, ApJ, 549, 979

Kraemer, K. E., Jackson, J. M., Kassis, M., et al. 2003, ApJ, 588, 918

Kroupa, P. & Burkert, A. 2001, ApJ, 555, 945

Krumholz, M. R. 2011, in American Institute of Physics Conference Series, Vol. 1386, American Institute of Physics Conference Series, ed. E. Telles, R. Dupke, & D. Lazzaro, 9–57

Krumholz, M. R. 2014, in American Astronomical Society Meeting Abstracts, Vol. 223, American Astronomical Society Meeting Abstracts #223, 318.01

Krumholz, M. R., Klein, R. I., & McKee, C. F. 2007, ApJ, 656, 959

Krumholz, M. R., McKee, C. F., & Klein, R. I. 2005, Nat, 438, 332

Kuiper, R., Klahr, H., Beuther, H., & Henning, T. 2010, ApJ, 722, 1556

Kuiper, R., Klahr, H., Beuther, H., & Henning, T. 2011, ApJ, 732, 20

Kurtz, S., Cesaroni, R., Churchwell, E., Hofner, P., & Walmsley, C. M. 2000, Protostars and Planets IV, 299

Kurtz, S., Churchwell, E., & Wood, D. O. S. 1994, ApJS, 91, 659

Kylafis, N. D. & Pavlakis, K. G. 1999, in NATO Advanced Science Institutes (ASI) Series C, Vol. 540, NATO Advanced Science Institutes (ASI) Series C, ed. C. J. Lada & N. D. Kylafis, 553

Lada, C. J. & Lada, E. A. 2003, ARA&A, 41, 57

Larson, R. B. 2003, Reports on Progress in Physics, 66, 1651

Liu, T., Wu, Y., Liu, S.-Y., et al. 2011, ApJ, 730, 102

Lopez, L. A., Krumholz, M., Bolatto, A., Prochaska, J. X., & Ramirez-Ruiz, E. 2010, in Bulletin of the American Astronomical Society, Vol. 42, American Astronomical Society Meeting Abstracts #215, 261

Luo, D., McCray, R., & Mac Low, M.-M. 1990, ApJ, 362, 267

Mason, B. D., Gies, D. R., Hartkopf, W. I., et al. 1998, AJ, 115, 821

McKee, C. F. & Ostriker, E. C. 2007, ARA&A, 45, 565

McKee, C. F. & Tan, J. C. 2003, ApJ, 585, 850

Menten, K. M. 1991, ApJ, 380, L75

Minier, V., Booth, R. S., & Conway, J. E. 2002, 383, 614

Moscadelli, L., Cesaroni, R., & Rioja, M. J. 2005, 438, 889

Motte, F. & André, P. 2001, in Astronomical Society of the Pacific Conference Series, Vol. 243, From Darkness to Light: Origin and Evolution of Young Stellar Clusters, ed. T. Montmerle & P. André, 301

Motte, F., Andre, P., & Neri, R. 1998, 336, 150

Nebot Gómez-Morán, A., Motch, C., Barcons, X., et al. 2013, 553, A12

Nielbock, M., Chini, R., Jütte, M., & Manthey, E. 2001, 377, 273

Nomura, H. & Millar, T. J. 2004, 414, 409

Norris, R. P., Byleveld, S. E., Diamond, P. J., et al. 1998, ApJ, 508, 275

Norris, R. P., Whiteoak, J. B., Caswell, J. L., Wieringa, M. H., & Gough, R. G. 1993, ApJ, 412, 222

Osorio, M., Lizano, S., & D'Alessio, P. 1999, ApJ, 525, 808

Osterbrock, D. E. 1989, Astrophysics of gaseous nebulae and active galactic nuclei

Osterbrock, D. E., Tran, H. D., & Veilleux, S. 1992, , 389, 305

Panagia, N. 1973, AJ, 78, 929

Parfenov, S. Y. & Sobolev, A. M. 2014, MNRAS, 444, 620

Parkin, E. R., Broos, P. S., Townsley, L. K., et al. 2011, ApJS, 194, 8

Pestalozzi, M. R., Elitzur, M., Conway, J. E., & Booth, R. S. 2004, ApJ, 603, L113

Phillips, C. J., Norris, R. P., Ellingsen, S. P., & McCulloch, P. M. 1998, MNRAS, 300, 1131

Phillips, J. P. & Ramos-Larios, G. 2008, MNRAS, 391, 1527

Pittard, J. 1998, MNRAS, 300, 479

Pittard, J. M. 2010a, in Astronomical Society of the Pacific Conference Series, Vol. 422, High Energy Phenomena in Massive Stars, ed. J. Martí, P. L. Luque-Escamilla, & J. A. Combi, 145

Pittard, J. M. 2010b, 81, 341

Pittard, J. M. & Dougherty, S. M. 2006, MNRAS, 372, 801

Pittard, J. M. & Parkin, E. R. 2010, MNRAS, 403, 1657

Pittard, J. M. & Stevens, I. R. 2002, 388, L20

Portegies Zwart, S. F., Pooley, D., & Lewin, W. H. G. 2002, ApJ, 574, 762

Pudritz, R. E., Ouyed, R., Fendt, C., & Brandenburg, A. 2007, Protostars and Planets V, 277

Puls, J. 2009, Communications in Asteroseismology, 158, 113

Raboud, D. & Mermilliod, J.-C. 1998, 333, 897

Raymond, J. C. & Smith, B. W. 1977, ApJS, 35, 419

Rohlfs, K. & Wilson, T. L. 2000, Tools of radio astronomy

Salpeter, E. E. 1955, ApJ, 121, 161

Sana, H., Stevens, I. R., Gosset, E., Rauw, G., & Vreux, J.-M. 2004, MNRAS, 350, 809

Sanna, A., Menten, K. M., Carrasco-González, C., et al. 2015, ApJ, 804, L2

Sanna, A., Moscadelli, L., Cesaroni, R., et al. 2010, 517, A78

Sanna, A., Reid, M. J., Moscadelli, L., et al. 2009, ApJ, 706, 464

Scalo, J. M. 1986, 11, 1

Schlafly, E. F. & Finkbeiner, D. P. 2011, ApJ, 737, 103

Schroeder, D. V. 1999, An Introduction to Thermal Physics

Shepherd, D. S. & Churchwell, E. 1996, ApJ, 457, 267

Shu, F. H. 1992, The physics of astrophysics. Volume II: Gas dynamics.

Shu, F. H., Adams, F. C., & Lizano, S. 1987, ARA&A, 25, 23

Shu, F. H. & Li, Z.-Y. 1997, ApJ, 475, 251

Sidoli, L., Mereghetti, S., Favata, F., Oosterbroek, T., & Parmar, A. N. 2006, 456, 287

Sidoli, L., Mereghetti, S., Treves, A., et al. 2001, 372, 651

Solomon, P. M. & Sanders, D. B. 1985, in Protostars and Planets II, ed. D. C. Black & M. S. Matthews, 59–80

Sridharan, T. K., Beuther, H., Schilke, P., Menten, K. M., & Wyrowski, F. 2002, ApJ, 566, 931

Stahler, S. W. & Palla, F. 2005, The Formation of Stars, 865

Stahler, S. W., Palla, F., & Ho, P. T. P. 2000, Protostars and Planets IV, 327

Sternberg, A., Hoffmann, T. L., & Pauldrach, A. W. A. 2003, ApJ, 599, 1333

Stevens, I. R., Blondin, J. M., & Pollock, A. M. T. 1992, ApJ, 386, 265

Strömgren, B. 1939, ApJ, 89, 526

Szymczak, M., Wolak, P., & Bartkiewicz, A. 2015, MNRAS, 448, 2284

Szymczak, M., Wolak, P., Bartkiewicz, A., & van Langevelde, H. J. 2011, 531, L3

Tayler, R. J. 1994, The Stars, Their Structure and Evolution

Testi, L., Felli, M., & Taylor, G. B. 1999, A&AS, 138, 71

Testi, L., Hofner, P., Kurtz, S., & Rupen, M. 2000, 359, L5

Torrelles, J. M., Gómez, J. F., Garay, G., et al. 1998a, ApJ, 509, 262

Torrelles, J. M., Gómez, J. F., Rodríguez, L. F., et al. 1998b, ApJ, 505, 756

Torrelles, J. M., Gomez, J. F., Rodriguez, L. F., et al. 1996, ApJ, 457, L107

Torrelles, J. M., Gómez, J. F., Rodríguez, L. F., et al. 1997, ApJ, 489, 744

Torrelles, J. M., Patel, N. A., Anglada, G., et al. 2003, ApJ, 598, L115

Townsend, R. 2009, ApJS, 181, 391

Townsley, L. K., Feigelson, E. D., Montmerle, T., et al. 2003, ApJ, 593, 874

Ungerechts, H., Walmsley, C. M., & Winnewisser, G. 1980, 88, 259

Usov, V. 1992, ApJ, 389, 635

van der Tak, F. F. S. 2004, in IAU Symposium, Vol. 221, Star Formation at High Angular Resolution, ed. M. G. Burton, R. Jayawardhana, & T. L. Bourke, 59

van der Tak, F. F. S., van Dishoeck, E. F., & Caselli, P. 2000, 361, 327

van der Walt, D. J. 2011, aj, 141, 152

van der Walt, D. J. 2014, 562, A68

van der Walt, D. J., Goedhart, S., & Gaylard, M. J. 2009, MNRAS, 398, 961

van der Walt, D. J., Maswanganye, J. P., Etoka, S., Goedhart, S., & van den Heever, S. P. 2016, 588, A47

van der Walt, J. 2005, MNRAS, 360, 153

Vink, J. S. & de Koter, A. 2005, 442, 587

Vink, J. S., de Koter, A., & Lamers, H. J. G. L. M. 2000, 362, 295

Vishniac, E. T. 1983, ApJ, 274, 152

Volpi, D. 2011, Bulletin de la Societe Royale des Sciences de Liege, 80, 733

Ward-Thompson, D. & Whitworth, A. P. 2011, An Introduction to Star Formation

Weaver, H., Williams, D. R. W., Dieter, N. H., & Lum, W. T. 1965, Nat, 208, 29

Williams, J. P., Blitz, L., & McKee, C. F. 2000, Protostars and Planets IV, 97

Williams, P. M., van der Hucht, K. A., Pollock, A. M. T., et al. 1990, MNRAS, 243, 662

Williams, S. J., Fuller, G. A., & Sridharan, T. K. 2004, 417, 115

Wolfire, M. G. & Cassinelli, J. P. 1987, ApJ, 319, 850

Wood, D. O. S. & Churchwell, E. 1989, ApJS, 69, 831

Yorke, H. W. 1986, ARA&A, 24, 49

Yorke, H. W. & Kruegel, E. 1977, 54, 183

Yorke, H. W. & Sonnhalter, C. 2002, ApJ, 569, 846

Zapata, L. A., Ho, P. T. P., Schilke, P., et al. 2009, ApJ, 698, 1422

Zhang, Q., Sridharan, T. K., Hunter, T. R., et al. 2007, 470, 269

Zinnecker, H. & Mathieu, R., eds. 2001, IAU Symposium, Vol. 200, The Formation of Binary Stars

Zinnecker, H. & Yorke, H. W. 2007, ARA&A, 45, 481